
From Biomimetic Multicompartments towards Artificial Cells

Design of Smart Polymeric Materials with Responsive Properties
to Mimic Cellular Functionalities

Inauguraldissertation

Zur Erlangung der Würde
eines Doktors der Philosophie vorgelegt der
Philosophisch-Naturwissenschaftlichen
Fakultät der Universität Basel

von

Sagana Thamboo
aus Basel-Stadt, Schweiz

2020

Genehmigt von der Philosophisch-Naturwissenschaftlichen Fakultät

auf Antrag von

Prof. Dr. Wolfgang Meier

(Universität Basel)

Fakultätsverantwortlicher/Dissertationsleiter

Prof. Dr. Nico Bruns

(Universität Strathclyde)

Korreferent

Basel, den 19.11.2019

Prof. Dr. Martin Spiess

(Dekan)

Dedication

அம்மா & அப்பா
கீர்த்தனா & சந்தனா
Claudio

Summary

Polymeric stimuli-responsive multicompartment vesicles can be designed to self-regulate their activity in a bioinspired manner, which mimics cellular signaling pathways. In this thesis, the modularity of our system is highlighted, giving a truly flexible multipurpose tool that can be readily adapted for multiple functions. A multicompartment architecture based on synthetic vesicles with sizes in the micrometer range (giant unilamellar vesicles, GUVs) is loaded with nanosized synthetic subcompartments and their functionality through a stimulus present in their environment is introduced. To achieve the environmental responsiveness, the loaded subcompartments are reduction-sensitive thus possessing a triggered activity resulting in a morphological change. The multicompartments are formed by one-pot self-assembly of a mixture of amphiphilic block copolymers poly(2-methyl-2-oxazoline)₅-*block*-poly(dimethylsiloxane)₅₈-*block*-poly(2-methyl-2-oxazoline)₅ (PMOXA₅-*b*-PDMS₅₈-*b*-PMOXA₅) and PDMS₆₅-*b*-heparin in the presence of specific molecules (enzymes, reporter compounds) and previously formed stimuli-responsive subcompartments, which contains the enzyme substrates or ion channels. By simultaneous co-encapsulation of desired molecules, and respective partners entrapped inside subcompartments, molecular tandems with a spatial segregation inside GUVs is realized. PDMS₆₅-*b*-heparin served to equip the surface of the multicompartment with a biological receptor-like moiety that will further support possible bio-interactions.

A sequential setup provides the multicompartments' activity: production of desired molecules by *in situ* triggered enzymatic reactions or selective flow of ions in/out via ion channel recruitment in the GUVs' membrane for biosensing purposes. An external signaling molecule added to the environment of the multicompartments diffuses across the GUVs' membrane, inducing the disassembly of the reduction-sensitive nanoparticles

and the release of the entrapped cargo. Depending on their chemical nature (enzyme substrates or biopores), these molecules initiate either an enzymatic reaction or a selective ion flow through the polymer membrane. In a more complex system, the biopore recruitment was induced to trigger the formation of an actin cytoskeleton (monomeric actin polymerized into filamentous actin) within the polymeric GUV, when selected ions could enter the vesicle's lumen. On the contrary, when the subcompartments are non-responsive or the external stimulus is not present, the multicompartments preserve their architecture and remain in a "silent mode" for several months. The combination of a primary signal (presence of stimulus in the environment of multicompartments) with a secondary one (induced ion flow to/from the environment) represents an important advance in multicompartment assembly, responsiveness, and triggered signal transduction. Our multicompartments have remarkable stability and activity because they preserve their integrity and respond "on demand" to signaling molecules to release the desired molecules. Triggered activity and change in the architecture of synthetic multicompartment vesicles, in auto-controlled sequences, are expected to open new directions for potential applications of these multifunctional systems in the domains such as medicine, catalysis and biosensing. The development of this bioinspired multicompartment with unprecedented mode of action and careful *in situ* characterization was achieved by combining expertise from materials science, chemistry and nanotechnology.

List of Abbreviations

3D-SIM	3D structured illumination microscopy	NaN ₃	sodium azide
Actin GUVs	G-Actin loaded giant vesicles	NP-Control	nanoparticles based on PMOXA ₃₀ - <i>b</i> -PCL ₆₂ (cargo: Bodipy 630/650)
Actin MCs	G-actin loaded multicompartments	NP-Graft	nanoparticles based on PMOXA ₈₈ -g(SS)-PCL ₂₃₈ (cargo: Bodipy 630/650, DGGR, gA, IoNo)
ADP	adenosine diphosphate	OG488	Oregon Green 488
ANG2	Asante Natrium Green2	OmpF	outer membrane protein F
ATP	adenosine triphosphate	PAH	polyallylamine
BCP	2-Hydroxy-4-(methacryloyloxy)-benzophenone	PBD	polybutadiene
CLSM	confocal laser scanning microscopy	PBS	phosphate buffered saline
CMC	critical micelle concentration	Pc	packing parameter
CPM	counts per molecule	PCL	polycaprolactone
CR	count rate	PDA	poly(dopamine)
cryo-TEM	cryonic transmission electron microscopy	PDMAEMA	poly(N,N-dimethylaminoethyl methacrylate)
DCM	dichloromethane	PDMS	poly(dimethylsiloxane)
DGGR	1,2-Di-O-lauryl-rac-glycero-3-(glutaric acid 6-methylresorufin ester)	PEG/PEO	poly(ethylene glycol)/poly(ethylene oxide)
DLS	dynamic light scattering	PIAT	polyisocynoalanine(2-thio- phene-3-yl-ethyl)amide
DMF	dimethylformamide	PISA	polymerization-induced self-assembly
DMSO	dimethyl sulfoxide	PLL	poly(L-lysine)
DNA	deoxyribonucleic acid	PMA	poly(methacrylic acid)
DTT	dithiothreitol	PMAC	poly(methacrylic acid) co-(cholesteryl methacrylate)
EmptyNPs	NP-Graft without cargo	PMOXA	poly(2-methylloxazoline)
EtOH	ethanol	PNIPAAm	poly(N-isopropylacrylamide)
Ex/Em	excitation/emission	PNMD	poly(methacrylic acid)
f	fraction of blocks	PNVP	poly(N-vinyl pyrrolidone)
F-actin	filamentous actin	PS	polystyrene
FCS	fluorescence correlation spectroscopy	PVA	polyvinyl alcohol
gA	gramicidin A	RT	room temperature
G-actin	globular actin	RZ	resazurin
GSH	glutathione	SEC	size exclusion chromatography
GUVs	giant unilamellar vesicles	SRB	sulforhodamine B
HEPES	4-(2-hydroxyethyl)-1-piperazineethanesulfonic acid	SRBVes	vesicles based on PMOXA ₅ - <i>b</i> -PDMS ₅₈ - <i>b</i> -PMOXA ₅ (cargo: SRB)
IoNo	ionomycin	SUVs	small unilamellar vesicles
LCST	lower critical solution temperature	TEM	transmission electron microscopy
LipVes	vesicles based on PMOXA ₅ - <i>b</i> -PDMS ₅₈ - <i>b</i> -PMOXA ₅ (cargo: Lipase)	UV	ultraviolet
LUVs	large unilamellar vesicles	Ves25	vesicles based on PMOXA ₅ - <i>b</i> -PDMS ₅₈ - <i>b</i> -PMOXA ₅ + 25% PDMS ₆₅ - <i>b</i> -heparin ₂₅ (cargo: Bodipy 630/650)
M100	micelles based on PDMS ₆₅ - <i>b</i> -heparin ₂₅ (cargo: OG488)	Ves5	vesicles based on PMOXA ₅ - <i>b</i> -PDMS ₅₈ - <i>b</i> -PMOXA ₅ + 5% PDMS ₆₅ - <i>b</i> -heparin ₂₅ (cargo: Bodipy 630/650, OG488)
MeOH	methanol		
Mn	number average molar mass		
Mw	weight average molar mass		
MWCO	molecular weight cut-off		
N	average number of particles		
NA	numeric aperture		
Na ⁺ Ves	vesicles based on PMOXA ₅ - <i>b</i> -PDMS ₅₈ - <i>b</i> -PMOXA ₅ (cargo: PBS)		

Table of Contents

Dedication	i
Summary	iii
List of Abbreviations	v
1. Introduction	1
1.1. Structure of a Cell	2
1.1.1. Cellular Membrane	2
1.1.2. Cellular Compartmentalization.....	3
1.1.3. Cytoskeleton	4
1.2. Strategies to Fabricate Synthetic Cell Mimics.....	7
1.2.1. Copolymers	9
1.2.2. Principle of Self-Assembly Process of Amphiphilic Block Copolymers.....	10
1.2.3. Comparison of Liposomes and Polymersomes	15
1.2.4. Fabrication Techniques of Vesicles.....	18
1.2.5. Stimuli-Responsiveness	20
1.2.6. Characterization Techniques of Cell Mimics	22
1.2.7. Combination of Biomolecules and Synthetic Materials	25
1.2.8. Compartmentalization within Cell Mimics	27
1.2.9. Vesicular Cytoskeleton Mimics	29
2. Aim of the Thesis	31
3. Self-Assembly and Characterization of Stimuli-Responsive Multicompartments.....	35
3.1. Introduction.....	36
3.2. Results and Discussion.....	37
3.2.1. Multicompartment Self-Assembly: Loading Synthetic Giant Vesicles with Subcompartments	37
3.2.2. Multicompartments with two different Subcompartments.....	45
3.2.3. Stimuli Responsiveness - Triggerable Multicompartments with Reduction-Sensitive Inner Subcompartments.....	47
3.3. Conclusion	53
4. Enzymatic Activity via Triggerable Multicompartments	55

4.1.	Introduction.....	56
4.2.	Results and Discussion.....	57
4.2.1.	Triggered Enzymatic Reactions in Multicompartment	57
4.2.2.	Compartmentalized Enzymatic Reactions using Two Internal Subcompartments.....	61
4.3.	Conclusion	64
5.	Ion Channel Recruitment in Triggerable Multicompartment	65
5.1.	Introduction.....	66
5.2.	Results and Discussion.....	67
5.2.1.	Triggered Ion Efflux via Compartmentalized Giant Polymersome.....	67
5.2.2.	Triggered Gramicidin Reconstitution for Ion Influx.....	69
5.2.3.	Ion Channel Recruitment using Two Internal Subcompartments	73
5.3.	Conclusion	75
6.	Cytoskeleton Mimic in Multicompartment	77
6.1.	Introduction.....	78
6.2.	Results and Discussion.....	79
6.2.1.	Actin Filament Polymerization in Synthetic GUVs	79
6.2.2.	Actin Polymerizing Multicompartment.....	84
6.2.3.	Actin Related Morphology Changes	88
6.3.	Conclusion	92
7.	General Conclusion and Outlook	95
8.	Experimental Section	99
8.1.	Materials.....	99
8.2.	Polymer Synthesis	99
8.2.1.	Synthesis of PMOXA ₅ - <i>b</i> -PDMS ₅₈ - <i>b</i> -PMOXA ₅	99
8.2.2.	Synthesis of PDMS ₆₅ -Heparin	100
8.2.3.	Synthesis of PMOXA ₈₈ -g(SS)-PCL ₂₃₈	100
8.2.4.	Synthesis of PMOXA ₃₀ - <i>b</i> -PCL ₆₂	101
8.2.5.	PMOXA ₆ - <i>b</i> -PDMS ₆₅ - <i>b</i> -PMOXA ₆	101
8.3.	Preparation of Nanostructures.....	102
8.3.1.	Bulk Rehydration Method	102
8.3.2.	Solvent Switch Technique.....	103
8.4.	Preparation of Giant Polymersomes	104

8.5.	Preparation of Multicompartment.....	104
8.6.	Preparation of Actin GUVs	106
8.7.	Preparation of Actin MCs	106
8.8.	Preparation of F-actin	107
8.9.	Fluorescence Imaging of Giant Polymersomes and Multicompartment	107
8.10.	Fluorescence Correlation Spectroscopy	109
8.11.	Transmission Electron Microscopy	113
8.12.	Cryonic Transmission Electron Microscopy	113
8.13.	Dynamic Light Scattering.....	113
8.14.	Enzymatic Test	114
8.15.	Pyrene-F-actin Polymerization Assays	114
8.16.	Preparation of Actin GUVs for 3D-SIM	114
8.17.	3D-SIM Super-Resolution Microscopy	115
9.	References	117
10.	Acknowledgements.....	133

1. Introduction

This chapter introduces several relevant topics and current scientific literature concerning this work to provide the reader with basic information. First an overview of the architecture and functions of biological cells, and how they can be used as inspiration for the construction of artificial cells based on synthetic materials is presented. For the construction of artificial cells, the relevance of biological elements, such as receptor like molecules, enzymes, pore channels or cytoskeletal elements will be discussed. The dissertation focuses on the fabrication of biomimicking responsive multicompartments, including synthetic building blocks and desired functionality. Amphiphilic block copolymers were utilized for the assembly of synthetic compartmentalized vesicles and therefore the self-assembly and characterization techniques will be shown, followed by the state-of-the-art techniques for the fabrication of responsive multicompartments that motivate the experimental approach of this thesis.

PARTS OF THIS CHAPTER HAVE BEEN PUBLISHED AND REPRINTED HEREIN WITH PERMISSION FROM REFERENCE ^[1]. COPYRIGHT (2019) JOHN WILEY AND SONS:

SAGANA THAMBOO, ADRIAN NAJER, ANDREA BELLUATI, CLAUDIO VON PLANTA, DALIN WU, IOANA CRACIUN, WOLFGANG MEIER^x AND CORNELIA G. PALIVAN^x. MIMICKING CELLULAR SIGNALING PATHWAYS WITHIN SYNTHETIC MULTICOMPARTMENT VESICLES WITH TRIGGERED ENZYME ACTIVITY AND INDUCED ION CHANNEL RECRUITMENT, *ADVANCED FUNCTIONAL MATERIALS*, 2019, 1904267.

PARTS OF THIS CHAPTER ARE A MANUSCRIPT IN PREPARATION:

SAGANA THAMBOO*, ANDREA BELLUATI*, ADRIAN NAJER, VIVIANA MAFFEIS, CLAUDIO VON PLANTA, IOANA CRACIUN, CORNELIA G. PALIVANX, WOLFGANG MEIERX, MULTICOMPARTMENT POLYMER VESICLES WITH ARTIFICIAL ORGANELLES FOR SIGNAL-TRIGGERED CASCADE REACTIONS INCLUDING CYTOSKELETON FORMATION, *ADVANCED FUNCTIONAL MATERIALS*, 2020, 2002949.

**These authors contributed equally*

1.1. Structure of a Cell

The cell is the basic unit of life that can perform all vital functions. This highly organized entity can be distinguished in two fundamental cell types: the prokaryotes (organisms without a nucleus, e.g. bacteria) and the more internally complex eukaryotes (organisms with a nucleus, versatile cytoskeleton and membrane bound organelles, e.g. animal and plant cells). While eukaryotic cells can differ by their shape or in terms of their function (replication, compartmentalization, movement, communication, sensing of the environment and its subsequent response), they share a common structure and are all composed of the same basic components such as the cell membrane, functional compartments called organelles and the cytoskeleton. [2, 3]

1.1.1. Cellular Membrane

The membrane of a cell serves as the barrier between the interior and the exterior, allowing only certain molecules to cross and relay messages via a chain of molecular events. The selectively permeable membranes are made of a lipid bilayer (most abundant glycerophospholipids) and embedded proteins, such as specific transport membrane proteins and receptor proteins (Figure 1).

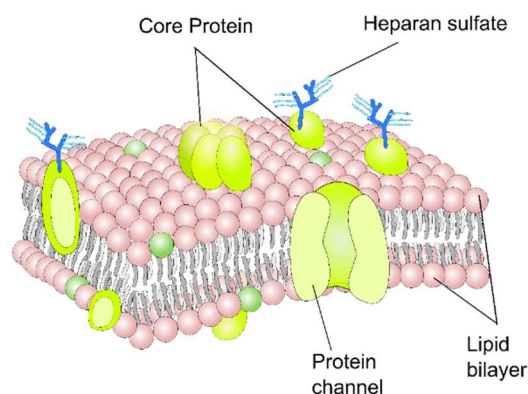


Figure 1. Schematic architecture of cellular membrane showing some of the main components: phospholipids, membrane proteins and glycosylation.

The membrane barrier and membrane proteins are essential to transport specific molecules and to maintain a concentration gradient. This allows the accumulation of important nutrients within the cell and the clearance of waste products and toxic

byproducts. ^[4, 5] The biological membrane is an active component containing receptor proteins that bind selectively molecules and transduce signals through intracellular messenger molecules to sense its local environment and communicate between cells. ^[6] Cellular compartments can either be horizontal, with no clear directionality in their communication and regulation (cell colonies or tissues), or hierarchical, where one compartment controls other lower-tier, often encapsulated, subcompartments, achieving a higher organizational level (organelles inside cell). ^[3, 7] Communication between cells (paracrine signaling) is based on receiving a first messenger, an external molecule that acts as a ligand on cell-surface receptors. The chemical signal triggers a conformation change in structures of the receptor. The activated receptor initiates the release of the second messenger (intracellular signaling molecule) to transduce a signal to the target area. ^[8]

1.1.2. Cellular Compartmentalization

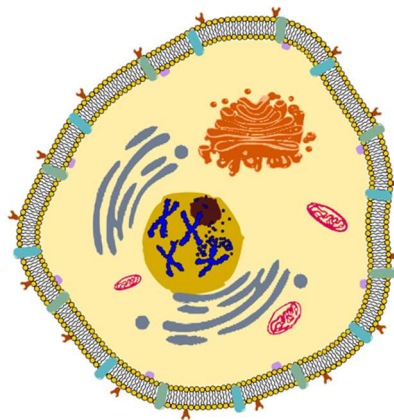


Figure 2. Schematic representation of a eukaryotic cell with compartments such as nucleus, mitochondria and Golgi apparatus.

Eukaryotic cells are subdivided into well-defined compartments with specific functions called organelles to create ion and small molecule gradients. Subcellular processes occur within organelles in the cytosol, such as nucleus, endoplasmic reticulum or Golgi apparatus, bound within the membrane and at the plasma membrane, present in various types of cells, such as neuron, muscle cell or epithelial cells. (Figure 2). Compartmentalization increases the efficiency of subcellular mechanisms by

concentrating the essential components in a limited space within the cell. This local separation (intracellular boundaries) leads to reduced disruption of function in other compartments and each carries out functions vital to survival. ^[9] For example, mitochondria can efficiently generate ATP by maintaining an electron gradients, while lysosomes can degrade internalized material at a lower pH than in the cytosol. ^[10] The optimal condition can be created within each compartment, where each organelle can achieve the highest efficiency. This subcellular organization allows hundreds of cascade activities precisely regulated in various intracellular organelles and toxic byproducts can be isolated in separate compartments. Reactions inside cells to generate or consume energy are known as the cellular metabolism based on anabolism (synthesis of molecules) and catabolism (degradation of molecules). Each step of the reaction is catalyzed by enzymes by lowering the activation energies. The chemical energy released through various chemical reactions (ATP hydrolysis) is used for unfavorable reactions which is fundamental for cellular activities such as cell maintenance, cellular movements and organization. ^[11, 12]

1.1.3. Cytoskeleton

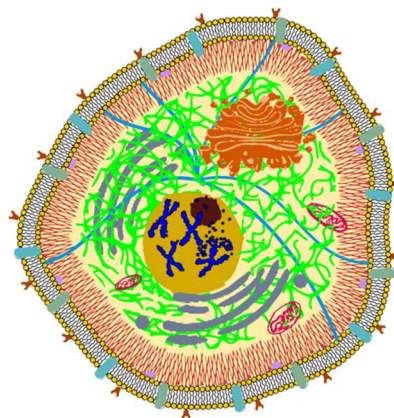


Figure 3. Schematic of the cytoskeletal organization within a cell. Intermediate filaments (green) connect to the nucleus and make the cell membrane mechanically more resistant against cell compression. Actin filaments (red) is anchored to numerous proteins on the cell membrane and regulates surface stiffness. Microtubules (blue) generate forces to push and pull organelles.

The cell is crowded by macromolecules which is vital to regulate subcellular metabolic processes. The confined space of a cell limits the diffusion of the molecules due to

biopolymers and the concentration of components (enzymes, substrates, ions) are optimized for specific reactions. ^[13] A network of proteins in the cytoplasm forms the cytoskeleton of a cell surrounded by the cell membrane. The cytoskeleton is responsible for the shape, cell division, cell movement, stability/support and serves as an anchor for organelles to allow their movement. The cytoskeletal fibers can be modified by active agents such as growth factors, hormones, second messengers and binding proteins. ^[14] The cytoskeleton contributes in the response to environmental changes by changing its shape and is comprised of three major interconnecting structural elements: (i) microtubules, (ii) intermediate filaments and (iii) actin filaments (Figure 3). ^[14] All subsystems have their own characteristic properties and shape. ^[15] In this thesis, the cytoskeletal component “actin” was utilized, an ideal candidate to study dynamics that was discovered by Straub in 1942. The flexible, but robust actin filaments form a cortical layer beneath the membrane to regulate the cell surface stiffness by providing stiffness and tension, responsible for cell locomotion. Pushing and pulling forces are facilitated to cause protrusions and invaginations in the membrane forming filopodia or microvilli (Figure 4).

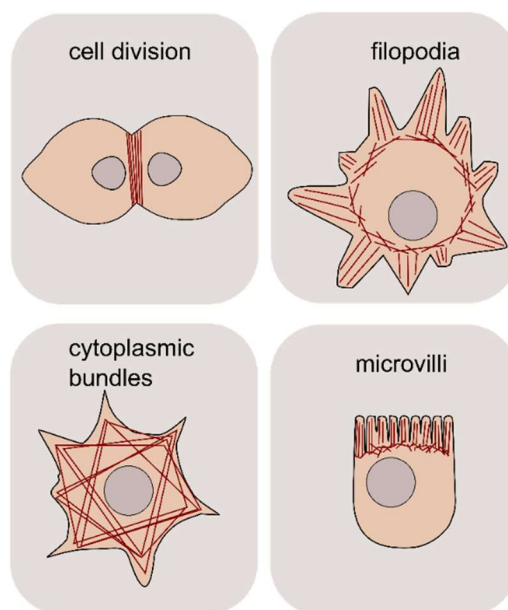


Figure 4. Illustration of actin based structures. The actin cytoskeleton is present throughout cells, forming a variety of well-defined, ordered structures (such as filopodia or microvilli) and contributing in various biological processes (cell division, migration).

Actin is the most abundant intracellular protein in eukaryotes and consists of two strands of globular subunits (approximately 42 kDa) which are twisted into a helix. ^[15, 16] Monomeric actin (globular actin, G-actin) is known to polymerize into filamentous actin (F-actin) by non-covalent bonds. ^[17] Actin polymerization occurs over three steps: (i) nucleation of dimers and trimers (ii) elongation into filaments (iii) steady state. Initial nucleation of actin is highly unfavorable and very slow and after overcoming this phase, the filament elongates quickly. Both ends of the actin filaments polymerize at different rates, where the rapidly growing is called barbed end and the slowly growing is the pointed end. Therefore, actin polymerization and depolymerization act at equilibrium, where filaments constantly grow and shrink through addition and removal of actin subunits. ^[18] F-actin forms when the total concentration of actin exceeds the critical concentration of actin, which is dependent on the nucleotide (ATP, ADP-Pi, or ADP) -associated divalent cations (Ca^{2+} or Mg^{2+}) and concentration and type of ions in solution. ^[19] Increasing ratio of ATP-actin to ADP-actin decreases the critical concentration of actin. Also salts are known to lower the critical concentration, since the filaments tend to become thermodynamically more stable. The charge-dense actin filaments possess specific binding sites for discrete cations with varying affinities such as Ca^{2+} , Mg^{2+} , K^+ and H^+ . ^[20, 21] The salt-dependency of the critical concentration is a result due to neutralization of the surface charges on the monomers. ^[19, 22] So far, the position of these sites and their contribution in actin polymerization and stiffness are not well studied. ^[22] There are numerous actin binding proteins, such as α -actinin, Arp2/3, profilin, formin, fascin and filamin, that influence the rate and extent of actin polymerization. ^[23] Filamin can act as a mechanosensor by sensing the cell environment and connecting actin with signaling molecules, receptors and channels. ^[24, 25] For example, the cooperation of actin and ion channels plays an important role to regulate channel location, channel activity and intracellular trafficking as in neurons or epithelial cells. ^[26, 27] Basically, the interactions of actin with its binding partners have

a vast influence assembling actin filaments into high-ordered bundles/networks essential for cell morphology and behavior.

In the following chapters, strategies to fabricate synthetic cell mimics are highlighted. The building block of our cell mimics, the amphiphilic block copolymer, are introduced and the self-assembly process are explained first. Further, the fabrication and characterization methods of vesicle based cell mimics are discussed. Then the importance of the stimuli responsive properties, the compartmentalization and the combination of biomolecules for the design of an artificial cell is described with examples of current state of the art cell mimics.

1.2. Strategies to Fabricate Synthetic Cell Mimics

The first cells are assumed to have been emerged as a result of about four billion years of evolution. We have an extensive knowledge about cellular building blocks, but do not understand how they collectively work together to mimic the high complexity of a biological cell. The simplest description, cells are self-enclosed compartments of biological material. ^[3, 28] A strategy to address the mystery of life is to try building cells from scratch, a challenge that has recently seen a boost due to novel paths of creating artificially constructed, nonbiological structures, or widely known as artificial cells. There is still some debate over the exact definition of the terminology “artificial cell”. In literature, they are also referred to as synthetic cells, minimal cells or protocells and commonly defined as a man-made minimal system in cellular dimensions to mimic or substitute some but not necessarily all fundamental cell features. ^[2, 3, 29] Synthetic and natural components are merged to study the transition from artificial cells to living cells, which is the key step for the transformation of non-living to living matter and so far the secret has not been solved yet. ^[3, 30] A vast amount of approaches to generate

artificial cells have been published in this currently emerging research field utilizing a large catalog of raw materials including bio-machineries of modern cells from different organisms as well as biomimetic synthetic components. ^[31]

An ideal candidate should exhibit the following properties: ^[2, 31]

- (i) Compatibility towards biological cell machineries (DNA, enzymes, membrane proteins and pores) and performing functions in parallel.
- (ii) Selective permeability (allowing the passage of nutrient and waste molecules) while retaining the compartment architecture.
- (iii) Self-sustainability to regulate enzymatic activities and undergo growth-division cycles.

Although the research of artificial cells is in its infancy, their full potential has yet to be exploited. The quest to produce a smart and micron-sized artificial cellular machine for future applications ranging from nanotechnology to medicine is making good progress. Artificial (or model) membranes have been studied to investigate mechanical and physical properties of membranes in a simpler surrounding compared to the complex cellular environment. ^[32, 33] The combination of biomolecules (e.g. proteins or nucleic acids) with synthetic material such as polymer based vesicles can direct to the creation of supramolecular materials with improved functionality. ^[32, 34] Vesicular cell models will undoubtedly find their use as microreactors in biotechnology, drug delivery systems and as biosensors. To achieve the construction of vesicle based artificial cells various interdisciplinary research fields need to closely collaborate. ^[2] So far, limitations of known cell models are their vastly reduced complexity compared to living cells. Due to tunability and robustness are polymeric artificial vesicles used for development of cell mimics that have the potential to perform multiple spatially separated biochemical reactions and trigger release within a confined space, resembling organelles in cells. In this work, we studied biomimetic polymer vesicle based multicompartement system that

serves as a scaffold of an artificial cell. First, amphiphilic block copolymers and their self-assembly of nanostructures are introduced.

1.2.1. Copolymers

A polymer (from the Greek term *poly* meaning many and *meros* meaning parts) is a macromolecule composed of repeating units called monomers. They can be classified as linear, branched, crosslinked (covalent bonds between polymer chains) or dendrimers (repetitively branched polymers).^[35] If all monomer units are the same, they are called homopolymers. In contrast, copolymers are formed from two or more types of monomers.^[36] Copolymers can be classified by the sequence repeat units as alternating, random, block and graft copolymers.^[35] Random copolymers possess random distribution of different repeating units, while block copolymers are long segments of the same repeating units and graft copolymers have a chain of a type of repeating units grafted onto a linear chain composed by another type of repeating unit.

Amphiphilic block copolymers, consisting of blocks with different polarities that are connected with covalent bonds, can be used as building blocks of polymeric vesicles. An amphiphile (from the Greek terms *amphis* meaning affinity for both and *philia* meaning love or friendship) is built from two components: a hydrophilic (from the Greek term *hydros* meaning water) part, which is attracted to water and a hydrophobic (from the Greek term *phobos* meaning fear) part, which is repelled by water and favors non-polar solvents.

An important parameter is the molecular weight of the polymer, which is characterized by the molar mass distribution and molar mass averages, since polymers are known to be polydisperse. The number average molar mass M_n is defined as

$$M_n = \frac{\sum_i N_i M_i}{\sum_i N_i} \quad (1)$$

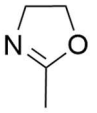
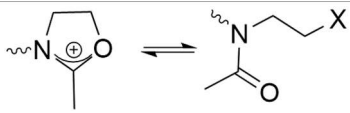
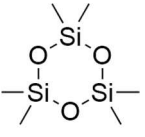
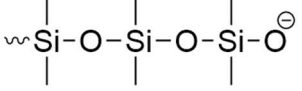
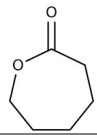
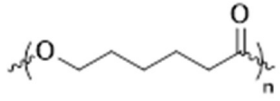
whereas N_i is the number of molecules with molecular weight M_i .

The weight average molar mass M_w is defined as follows

$$M_w = \frac{\sum_i N_i M_i^2}{\sum_i N_i} \quad (2)$$

In this study, the block copolymer PMOXA-*b*-PDMS-*b*-PMOXA, which is composed of the polymer poly(2-methyloxazoline)(PMOXA) and the hydrophobic poly(dimethylsiloxane) (PDMS), and PMOXA-*g*-PCL with the hydrophobic polycaprolactone (PCL) block were used (Table 1). PDMS, the hydrophobic block, is biocompatible, and widely used as material for pacemakers, contact lenses or breast implants. PDMS with lower molecular weight (5 kDa) degrades slowly in the body, is easily removed from the body and is filtered out through the kidney. [37] PCL is known for its semi-crystalline nature and biodegradability. [38] PMOXA, the hydrophilic block, is biocompatible and known to be mostly cleared out from the blood stream after 24 h. The non-ionic and protein-repellent nature of PMOXA is favored, since charged polymers tend to induce stronger immune response. [37]

Table 1. Polymerizable monomers and the corresponding active species.

Monomer	Growing chain	Polymerization Method
2-methyloxazoline 	PMOXA 	Cationic Ring Opening Polymerization
dimethylsiloxane 	PDMS 	Anionic Ring Opening Polymerization
ε-caprolactone 	PCL 	Coordination–insertion Ring Opening Polymerization

1.2.2. Principle of Self-Assembly Process of Amphiphilic Block Copolymers

When amphiphilic block copolymers are introduced into an aqueous solution, they form supramolecular assemblies or self-organize spontaneously into a variety of structures

depending on specific properties and concentrations. ^[35, 39] Copolymer chains arrange to a bilayer for diblock copolymers and looped conformations (both hydrophilic ends in the same leaflet) of triblock copolymers, while triblock copolymers in a stretched conformation form a monolayer. ^[40] Supramolecular structures are held together by forces like Van der Waals, hydrophobic interactions and hydrogen bonding and not by covalent bonds. ^[35] The role of molecular geometry is important to predict the shape of assemblies. A whole spectrum of morphologies can be observed depending on the relative volume fraction of blocks. These morphologies expand from spherical and cylindrical micelles, to bilayers and vesicles. ^[39] The morphology of nanostructures depends on the geometry of the amphiphile with its ratio of hydrophobic and hydrophilic fragments (Figure 5). ^[41]

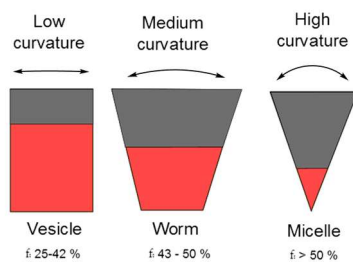


Figure 5. Due to the curvature of the amphiphilic block copolymer, the packing parameter P_c can be estimated. Relative volume fraction of blocks; f: hydrophilic fraction. Adapted with permission from ref ^[42]. Copyright (2009) John Wiley and Sons.

One unifying rule to generate mainly vesicles in aqueous solution is a ratio of hydrophilic to total mass of $f \approx 35\% \pm 10\%$. Block copolymers with more than 45% of hydrophilic part form mainly micelles whereas close to this region also wormlike micelles can be formed. Inverted structures can be built with less than 25% of hydrophilic part.

^[43]

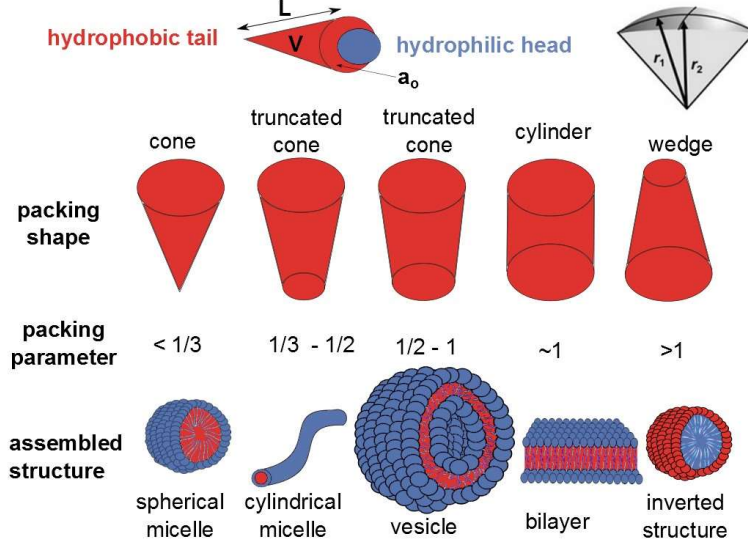


Figure 6. Morphology predicted by packing parameter. Adapted from ref ^[44].

The critical packing parameter P_c describes the geometry of amphiphile as depicted in Figure 6 and is defined as follows

$$P_c = \frac{v}{a_0 L} \quad (3)$$

where v is the volume of hydrophobic block, a_0 is the area covered by the hydrophilic block and L is the length of the hydrophobic block. ^[35, 45] P_c directly correlates with the type of assembly and can be related to the radius of curvature. ^[35]

$$P_c = 1 - HL + \frac{K_G L^2}{3} = 1 - \frac{1}{2} \left(\frac{1}{r_1} + \frac{1}{r_2} \right) L + \frac{L^2}{3r_1 r_2} \quad (4)$$

The mean curvature H is defined as

$$H = \frac{1}{2} \left(\frac{1}{r_1} + \frac{1}{r_2} \right) \quad (5)$$

and the Gaussian curvature K_G as

$$K_G = \frac{1}{r_1} \cdot \frac{1}{r_2} = c_1 \cdot c_2 \quad (6)$$

where r_1 and r_2 are curvature radii, which are the reciprocals of the principle radii of curvature c_1 and c_2 . The morphology of structures corresponds to the minimal elastic energy at a given vesicle area and volume. ^[45] Planar bilayers are predominant when P_c is close to 1 ($r_1 = r_2 = \infty$, $H = 0$). Spherical ($r_1 = r_2$, $H = \frac{1}{r_1}$) and cylindrical ($r_1 = r$, r_2

$= \infty$, $H = \frac{1}{2r}$) micelles are formed with $P_c < 0.5$ and smaller curvature for $0.5 > P_c > 1$.
[35]

A large variety of well-defined structures can be built spontaneously as a result of self-organization, which is a consequence of non-covalent forces [45, 46] and their unique properties need to be well understood to optimize their performances. The driving force for all processes is the minimization of free energy. [35]

The basic principle of self-association is based on the balance between the disordered and the organized system, the interactions between the moieties of the amphiphilic molecules and solvent molecules, and poor solubility of the hydrophobic block. Hydrophobic substances tend to aggregate in aqueous medium to exclude water molecules. [35] Linear non-polar structures are more hydrophobic than branched ones, since they have a smaller area of contact with the aqueous environment. Inert surface molecules, such as alkanes, hydrocarbons and fluorocarbons, are not able to form hydrogen bonds. Therefore, water molecules close to the inert surface rearrange themselves to form hydrogen bonds with other water molecules to minimize the contact to the inert surfaces and are more ordered compared to free moving water molecules. [47] The so-called hydrophobic effect is thought to be the main driving force of the phenomenon self-assembly of amphiphiles [35] This effect is an entropic driven process whereas the free energy of a process is dependent on the enthalpic H and entropic S terms as follows [35]

$$\Delta G = \Delta H - T\Delta S \quad (7)$$

Temperature plays an important role because of the contribution $T\Delta S$ to the free energy. Considering thermodynamics, amphiphiles organize in aqueous media, so this self-association leads to loss of entropy, which would be technically unfavorable from the entropic perspective. [35] But amphiphilic molecules in water cause a higher ordering of the amphiphile-surrounding water molecules, which form a cage around hydrophobic

moieties. Therefore, the self-assembly of amphiphiles leads to a minimization of interactions of the hydrophobic part with neighboring water molecules, which overcompensates the loss of entropy by the aggregation of amphiphilic molecules.^[35] The hydrophobic effect is dependent on changes in temperature, pH, concentration, geometrical constitution of amphiphiles and solution properties (salinity, flexibility).^[35, 48] The hydrophobic effect takes place when a sufficiently high amphiphile concentration are put in aqueous solution.^[48] In colloidal chemistry, the critical micelle concentration (CMC) is defined as the concentration of amphiphiles above which micelles are spontaneously formed. At CMC, the moiety of free molecules in bulk solution is equal to the moiety of molecules forming micellar assemblies.^[49] The increase in concentration leads to an increase of the number of molecules in the aggregate with unchanged concentration of monomers in solution. When the concentration of amphiphiles is above the CMC, they form structures depending on temperature and geometry of the moieties.^[35]

The bilayer-to-vesicle model, known in literature as “mechanism I”, is the most commonly accepted mechanism for the formation of vesicles. This model describes the vesicle formation as a result of a two-step process, where first the planar membrane is formed from micelles, that then bends and rolls up and finally closes into spherical hollow vesicles.^[50] An alternative vesicle formation mechanisms is a model referred as “mechanism II” in literature, where micelles grow into vesicles without aggregating first into a planar membrane. The solvent molecules diffuse into the micelles until the bending energy is sufficiently lowered and then the micelles reorganize into semi-vesicles and lastly into vesicles. There is no universal explanation for the vesicular self-assembly mechanism due to variations of polymer properties and therefore, some pathways have not yet been discovered.^[50]

1.2.3. Comparison of Liposomes and Polymersomes

Liposomes are lipid based vesicles that are well-studied and most commonly used as a chassis for artificial cells since their discovery in 1964. The key advantage of liposomes is the use of lipids, which are the building blocks of living cell membranes and allow the reconstitution of biological components without loss of functionality and the ability to be simplistic. ^[51] The cell plasma membrane is known to be significantly less fluid than model lipid membranes due to links between proteins in the membrane and the cytoskeleton. ^[6, 52, 53] However, the major limitations are that liposomes are known for their instability, unintended permeability and the lack of specificity/tuneability. ^[54] To overcome these challenges, polymersomes, have been widely explored and gained popularity. ^[55, 56] Polymersomes are a class of vesicles based on synthetic amphiphilic block copolymers and are fully synthetic analogs of liposomes. ^[51] Liposomes and polymersomes comprise an aqueous lumen that is protected from the external environment by a hydrophobic membrane which allows the encapsulation of both hydrophilic and hydrophobic cargo. Besides the similar properties, these nano- to micrometer sized spherical structures, possess significant differences, such as lateral mobility, permeability and stability (**Figure 7**). ^[57] There is a large diversity of copolymers with a molecular weight up to 10s of kDa to form polymersomes, ^[40] while in comparison, membrane forming lipids are limited and have a molecular weight less than 1 kDa. ^[58] Polymeric vesicles are mechanically and thermodynamically much more stable than the well investigated lipid vesicles. The advantages of amphiphilic block copolymers over lipids are an increased stability and robustness due to higher molecular weight. The polymer membrane has a greater chemical versatility and its thickness can be easily controlled. ^[59] The polymeric membrane can have thicknesses in the range of 5-30 nm, while lipid membranes are 3-5 nm thick, allowing larger hydrophobic solutes to be incorporated into the polymer membrane. ^[59]

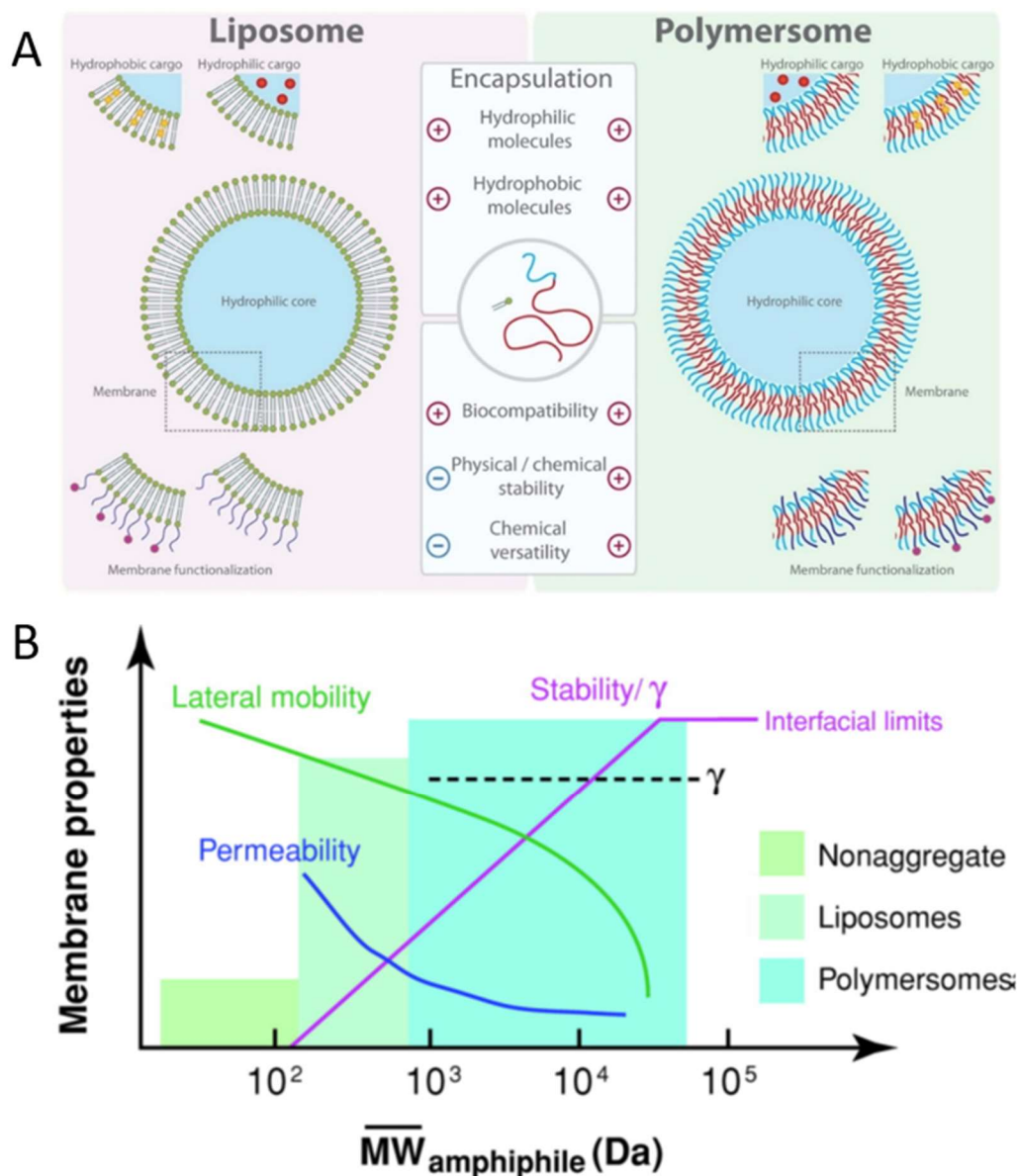


Figure 7. Properties of liposomes and polymersomes. **(A)** Comparison of liposomes and polymersomes. Reproduced with permission from ref ^[60]. Copyright (2014) Elsevier Ltd. **(B)** Membrane properties due to difference in molecular weight of amphiphiles. Reproduced with permission from ref ^[43]. Copyright (2006) Annual Review of Biomedical Engineering.

The majority of studies focus on nanoscale vesicles (~ 100 nm), the so-called small and large unilamellar vesicles (SUVs and LUVs, Table 2), that offer innovative solutions as cargo delivery systems for therapy and diagnostics or as artificial organelles loaded with active compounds (e.g. enzymes, proteins, catalysts, mimics) to provide confined reactions. On the other hand, the large size (microscale, from 1 to 200 μm) of giant unilamellar giants (GUVs) makes them more suitable for research as cell models or artificial cells to understand complex biological processes. ^[1] Lipid based GUVs are the

most common model membrane system for synthetic cells. ^[61] Size affects factors such as stability, membrane curvature, volume and effective encapsulated. The spherical micron-scale GUVs have the advantage to be directly observable by conventional light microscopy, differential interference contrast microscopy and phase contrast microscopy. ^[54] Manipulations of single GUVs and their response towards external factors can be immediately visualized. One possible technique for visualization is to use a dense solution, such as sucrose, to swell the GUVs and subsequently dilute in an isotonic solution (less dense than sucrose) to prevent GUVs from collapsing due to the osmotic difference to the surrounding solution.

Table 2. Comparison of properties of liposomes, polymersomes and eukaryotes. Adapted with permission from ref ^[62]. Copyright (2018) Royal Society of Chemistry.

	Liposomes	Polymersomes	Eukaryotic cells
Molecular weight of building compounds	$10^2 - 10^3$ Da	$10^3 - 10^4$ Da	$10^2 - 10^5$ Da
Membrane thickness	3–5 nm	5–50 nm	8–10 nm (including membrane proteins)
Diameter		SUV: 20–100 nm LUV: 100–1000 nm GUV: 1–200 μ m	Animal cells: 10–30 μ m Plant cells: 10–100 μ m
Encapsulating volume (calculated)	SUV: $10^{-15} - 10^{-13}$ μ L LUV: $10^{-13} - 10^{-9}$ μ L GUV: $10^{-9} - 10^{-3}$ μ L	SUV: $0 - 10^{-13}$ μ L LUV: $0 - 10^{-9}$ μ L GUV: $10^{-9} - 10^{-3}$ μ L	Animal cells: $10^{-6} - 10^{-5}$ μ L Plant cells: $10^{-6} - 10^{-3}$ μ L

The choice of block copolymers influences the biocompatibility, biodegradability, permeability and release conditions. ^[63] For biological applications, the materials used need to be ideally non-toxic, biocompatible with bioactive molecules and stable under various conditions. ^[40] Over the past decades, a vast range of technologies were developed to fabricate vesicular structures. The choice of the vesicle formation technique has an enormous influence on the properties such as sizes and polydispersity of vesicles. ^[63, 64] A short overview of selected approaches using hydration, solvent switch, electroformation, double emulsion and microfluidics are given. Reviews discuss the methodologies in more details are Supramaniam et al 2019, ^[6] Palivan et al 2016 ^[32] or Kamiya et al 2017. ^[65]

1.2.4. Fabrication Techniques of Vesicles

1.2.4.1. Film Hydration

For the first time in the 1960s, Reeves and Dowben have reported a gentle hydration approach to self-assemble GUVs by resuspending lipid bilayers. Vesicular structures are formed by spontaneous swelling of the dry film after introduction of an aqueous buffer. Film hydration is straightforward and minimal traces of organic solvent are present. The method simply involves the formation of a dry amphiphile film on a solid surface (glass) by dissolving the amphiphiles in organic solvent, followed by evaporation. The resuspension by aqueous buffer containing the cargo of interest results in formation of vesicles. Nevertheless, the process can take usually several hours towards several days for the vesicle formation. The quality of vesicles strongly depends on the amphiphile, buffer composition and drying parameters. A major disadvantage is the probability to generate multilamellar or multivesicular vesicles and debris of the amphiphiles. ^[66] Homogenization of vesicles can be achieved through sonication, extrusion, freeze-thaw method and vortexing, or a combination of these techniques. ^[45] SUVs, GUVs and multilamellar vesicles with a large polydispersity are formed. ^[62]

1.2.4.2. Solvent Switch Method

The solvent-switch method is performed by dissolving the amphiphiles in organic solvents where all blocks are soluble. The vesicular structures are formed after dropwise addition an aqueous buffer. The procedure is much faster with this method compared to film rehydration, since the polymers are in solution from the beginning, and it is highly dependent on the balance between the state of the polymers (assembled and non-assembled). The organic phase is excluded, but technically not all solvent can be removed. The major drawback are the traces of organic solvents. ^[45, 67] Mainly SUVs, with a large polydispersity are formed. ^[62]

1.2.4.3. Electroformation

Another technique to form vesicular structures is electroformation which was developed in 1986. An alternating electric current is applied via electrodes to the dry film in an aqueous buffer, requiring non-physiological low concentrations of salt. ^[68] This was a big disadvantage for the use as artificial cells, since biological elements need physiological buffers. Use of higher frequencies (500 Hz compared to 10 Hz) could overcome this disadvantage. ^[69] A major drawback is also that applied electric field in general could cause damage to biological machineries as reported earlier. ^[70] Mainly GUVs are formed with a low polydispersity. ^[62]

1.2.4.4. Gel-Assisted Swelling

An alternative method without the use of electric current is the gel-assisted swelling technique. Horger et al first reported the deposition of the dry amphiphile film on a porous agarose gel spin coated on a glass slide and vesicles were formed in presence of a flow of buffer from below. ^[71] The benefits of this technique are higher rate of homogenous GUV formation under physiological condition and biocompatibility. ^[62] A drawback is the fusion of the vesicles over time and that agarose and the amphiphiles interact which affects the vesicle property. ^[72] To overcome this, polyvinyl alcohol (PVA) ^[73] or dextran(ethylene glycol) ^[74] can be used as an alternative which is also compatible with a variety of biomolecules. The major drawback is the contamination of the vesicles by the gel and the difficult detachment of the vesicles from the gels. ^[73]

1.2.4.5. Inverse Emulsion Phase Transfer

Vesicles can also be fabricated from a water-in-oil droplet by the emulsion based approach or the so-called inverse emulsion phase transfer. The amphiphiles stabilize the oil-water interphase. This technique results in narrow polydispersity GUVs. ^[62] The procedure is not well-studied, and vesicles are heterogenous. The main disadvantage of this approach is the low yield and traces of oil in the GUV membrane. ^[15, 75]

1.2.4.6. Double Emulsion using Microfluidic Techniques

To upscale vesicle production, the emulsion base approach was transferred to microfluidic devices for an improved control of the individual steps including a continuous droplet interface. Double emulsion droplets are water droplets within thin oil layer surrounded an aqueous phase. Microfluidic technology shows several benefits such as high encapsulation efficiency, high throughput formation of monodisperse vesicles (SUVs or GUVs) and high degree over size. ^[62] One of the major disadvantages are the technically complexity and the content of organic solvents in the interphase. The evaporation of the organic solvent is not efficient and therefore the remaining solvent residue can interfere with membrane functionality and biological mechanisms. ^[6] The amount of oil and alteration on the mechanics is not simply measurable. ^[76] The use of emulsion droplets requires the use of Pluronic F-68, PEG, PVA in the aqueous outer phase which may not be biocompatible. ^[65]

1.2.5. Stimuli-Responsiveness

In nature, cells require local dynamic changes subcellular compartments and can sense external environmental changes to maintain biological functions. Similarly, smart materials, such as synthetic polymer assemblies have potential applications as ‘on demand’ cargo release in delivery systems and as self-repairing supplies in the biomedical field. ^[8] Stimuli-responsiveness was achieved either by designing copolymers with a special chemical nature, inducing a change in the membrane permeability or even its disintegration upon a change in their environment. ^[4] Stimuli responsive materials provide additional functionality and allow the fabrication of efficient transduction mechanisms for use in sensors. Copolymers play an important role in the design of responsive artificial cell systems. Stimuli responsive synthetic materials are capable of chemical and conformational changes due to a specific external stimulus as trigger and respond to their environment in an intelligent way, allowing a higher degree of control. Light, temperature, pH, redox potential enzymatic activities, temperature, light, magnetic field, electric field and mechanical force can serve as physiological or external stimuli of smart responsive materials (Figure 8). ^[77-79]

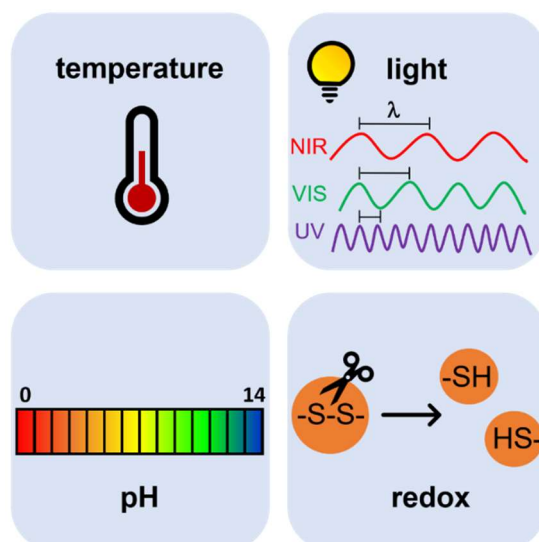


Figure 8. Some examples of stimuli triggers for responsive materials.

Researchers developed a vast diversity of macromolecules that can self-assemble into desired morphologies. For instance, poly(N-isopropylacrylamide) (PNIPAAm) is a temperature responsive polymer with a lower critical solution temperature (LCST, $\sim 32^{\circ}\text{C}$). At rising temperatures this polymer goes through a phase transition from an extended random coil to a compressed conformation. Above its LCST the polymer is hydrophobic and below the LCST it becomes hydrophilic.^[80] pH sensitive systems react to changes in the concentration of protons. An example is the charged hydrophilic Poly(N,N-dimethylaminoethyl methacrylate) (PDMAEMA) that forms a cationic polyelectrolyte and has ionizable functional groups to accept or donate protons.^[81] Light responsive materials are sensitive towards light illumination and results in light triggered isomerization or ionization. Mabrouk et al used a mixture of the non-responsive copolymer poly(ethylene glycol)-*b*-polybutadiene (PEG-*b*-PBD) and UV-responsive LC-based copolymer PEG-*b*-PMAazo444 to form vesicles with potential application in the field of drug delivery and cosmetics.^[82] The LC block contains an azobenzene group that undergoes a trans-to-cis conformational change upon exposure to UV light. UV and visible light are limited due to smaller penetration depth due to strong scattering, so near infrared illumination is preferred, having deeper penetration and minimal harm.^[83] Reduction sensitive materials play a potential role as drug delivery systems in the field of nanomedicine. Disulfide bonds between block

copolymers are sensitive to reduction with high thiol concentrations. ^[57, 78] PEG-*b*-poly(propylene sulfide) polymersomes containing disulfide bonds was first developed by Cerritelli et al and demonstrated to be destabilized in the presence cysteine and GSH. ^[84]

In this work, subcompartments with stimuli responsive properties are used as organelle-mimics and loaded into a microscale compartment. The spatial organization in artificial cells offers the possibility for dormant compartments to activate their functions in presence of relevant stimuli. The stimuli responsive behavior in a hierarchical organization is important to develop systems that can receive signals and respond by changes in the material. ^[2, 77, 78]

1.2.6. Characterization Techniques of Cell Mimics

Specific characteristics of artificial cell mimics, such as size, structure, permeability, responsiveness to stimuli and functionality need to be in-depth characterized to fully understand the systems. For the characterization of intrinsically fluorescent or fluorescently labelled micron-sized cell mimics (e.g. GUVs), confocal laser scanning microscopy (CLSM) can be used for visualization and fluorescence correlation spectroscopy (FCS) for follow up of fluorescent species in their native solution.

Fluorescence is a useful tool for many studies to distinguish between what is interesting (signal) and what is not (background noise). The phenomenon “fluorescence” is the emission of light of a molecule and occurs from the excited electronic state after the absorption of light. The difference in energy, the so-called Stokes shift occurs when the adsorbed photon has more energy than the emitted photon. For singlet states, the electron that is transitioned into a higher electronic excited state and its paired electron in the ground state have opposite spins which is essential for fluorescence. In contrary, for the phenomena called phosphorescence, the spins are parallel and called triplet excited state. The basic principle of fluorescence is illustrated in the Jablonski diagram

(Figure 9), illustrating the electronic states of a molecule and the possible transitions between them (developed by Alexander Jablonski in 1933).

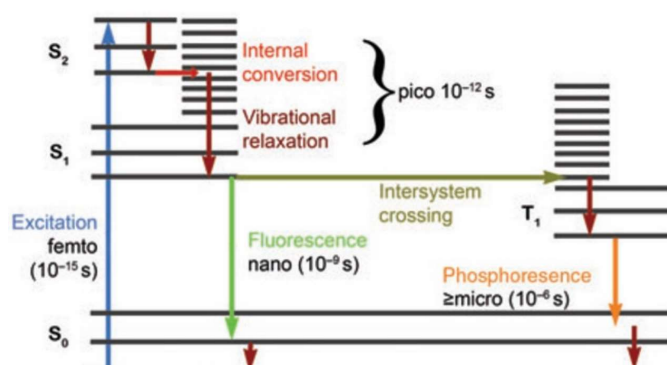


Figure 9. Jablonski diagram: possible energy transitions after absorption of a photon – fluorescence and phosphorescence. Reproduced with permission from ref [85]. Copyright (2005) Springer Nature.

On the left side of the Jablonski diagram are the single states (S_0 , S_1 , S_2), while the triplet states (T_1) are positioned on the right. The ground state S_0 is defined as the energy of a molecule that is non-excited by light, while S_1 and S_2 are excited singlet states. Over the past years, a vast number of fluorophores, molecules with fluorescent properties, have been provided to study biologically relevant systems. The valence electron orbital of the fluorophore determines the absorbed and emitted wavelength, as well its efficiency. [85]

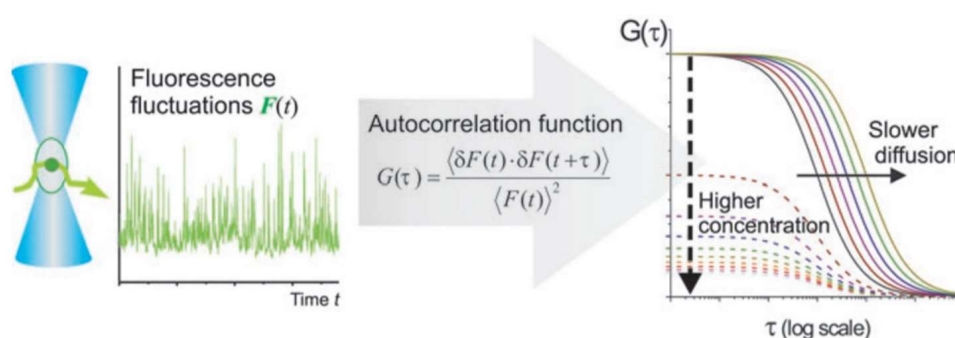


Figure 10. Fluorescent molecules diffuse through the confocal volume and a fluctuating fluorescence signal is recorded. FCS autocorrelation curve $G(\tau)$ is obtained when the time trace is subjected to an autocorrelation algorithm. Reproduced with permission from ref [86]. Copyright (2006) Nature Springer.

Fluorescence correlation spectroscopy (FCS) has become a widely used routine techniques for studies of various field such as physical, chemical and biological sciences in the recent years. FCS was originally introduced in the early 1970s to measure

diffusion coefficients of fluorescent molecules. This technique enables the detection of fluorescence intensity fluctuations in a subfemtoliter confocal volume (1 fL) generated by a focused laser beam and provides information about thermodynamics and kinetics of fluorescent molecules at nanomolar concentrations. ^[87] The tiny, spontaneous fluctuations are caused by deviations from thermal equilibrium in an open system (Brownian motion) and for chemical reaction (Poisson process). ^[88] With FCS, the diffusion properties, chemical rate constants, hydrodynamic radii, molecular concentrations, molecular brightness and interactions are measured *in vivo* and *in vitro* in solution. FCS is carried out on a confocal microscope and the fluorescent signal originates from an illuminated single spot (confocal volume). The intensity fluctuations are recorded and autocorrelated over time. Small rapid diffusing species produce rapidly fluctuating patterns, while larger slower diffusing molecules yield rather sustained bursts of fluorescence (Figure 10). ^[89]

The diffusion coefficient D can be calculated using the relation between τ and the x-y dimension of the confocal volume (ω_{xy}):

$$\tau = \frac{\omega_{xy}^2}{4D} \quad (8)$$

ω_{xy} is given by the laser wavelength and the numerical aperture (NA):

$$\omega_{xy} = \frac{\lambda}{2 \cdot NA} \quad (9)$$

The Einstein-Stokes equation uses the diffusion coefficient D , the Boltzmann's constant k_B , absolute temperature T and viscosity of the surrounding medium η to calculate the hydrodynamic radius (R_H) of the nanostructures.

$$D = \frac{k_B T}{6\pi\eta R_H} \quad (10)$$

The spatial and temporal correlation of fluorescent species with each other is measured and a statistical analysis of the fluctuation data are mathematically quantified by an

autocorrelation algorithm. ^[88] The fluorescence fluctuation autocorrelation function $G(\tau)$ is defined as follows:

$$G(\tau) = \frac{\langle \delta F(t) \delta F(t + \tau) \rangle}{\langle F(t) \rangle^2} \quad (11)$$

The symbols $\langle \dots \rangle$ stands for averaging over a long period of time and τ as an interval. $\delta F(t + \tau)$ is the fluctuation at the shifted time $t + \tau$. The fluorescence intensity fluctuation is defined as

$$\delta F(t) = F(t) - \langle F \rangle \quad (12)$$

where $\langle F \rangle$ is the time averaged value of $F(t)$. ^[88] The initial amplitude of the autocorrelation function is inversely proportional to the average number of particles $\langle N \rangle$ in the confocal volume and yielded as follows

$$G(0) = \frac{1}{\langle N \rangle} = \frac{1}{V_f \langle C \rangle} \quad (13)$$

The time at the half intensity of the autocorrelation curve is the diffusion time τ_D . The detection volume V_f results in the concentration C of the particles and the number of particles N .

In this work, CLSM coupled with *in situ* FCS was selected for the characterization our responsive multicompartments systems due to its sensitivity towards tracking individual cascade reaction steps or to measure the encapsulation efficiency of biomolecules and subcompartments within the giant vesicles. In future, this method can be used as a standard characterization for artificial cells.

1.2.7. Combination of Biomolecules and Synthetic Materials

Numerous characteristics of living cells, including signalling cascades, energy transduction, complex compartmentalization, protein expression, growth and division, have been successfully modelled in isolation using artificial cells. ^[61, 62, 90-92] Artificial

assemblies can serve as potential scaffolds, carriers and/or subcompartments. Since the functionality of various membrane proteins can also be preserved when inserted in polymer membranes, ^[32, 34] the basis for creating complex protocells from combinations of synthetic and biological components is given. Specific ions, solutes and molecules can be exchanged across the artificial membrane. Possible techniques of selective permeability are the use of polymers that form porous membranes, pore formation by chemical modifications or the insertion of membrane proteins, transporters, ion channels or pore-forming peptides. Functional insertion of ion channels (biopores) and membrane proteins allow the permeability of polymer membranes as in PMOXA-PDMS based studies. ^[93] The incorporation of gramicidin ion channels into nanoscale polymersomes was studied for selective permeability of protons, sodium and potassium ions. ^[94] Size selective pores in polymersomes can be formed by embedding channel forming proteins ^[95] or using stimuli-responsive copolymers to generate pores. ^[81] For catalysis process within vesicles, channel proteins are a suitable choice for passage of substrate molecules while encapsulating enzymes inside. A single compartment designed to perform an explicit reaction is known as a nanoreactor (artificial organelle). The first nanoreactor was demonstrated by Meier and coworkers. ^[96] A spatially confined metabolic reaction can be performed in a single nanoscale compartment to replicate cellular metabolic procedure. ^[96] In this particular scenario, the outer membrane protein F (OmpF), a channel forming protein was incorporated into the polymeric membrane. This allowed the size selective entry of a substrate into the polymersome lumen for subsequent hydrolysis by encapsulated B-lactamase.

Two common membranous structures that are being utilized for building cell-like entities are giant liposomes and giant polymer vesicles (polymersomes), ^[34, 62] besides other systems such as proteinosomes, coacervates, colloidosomes, polypeptide or polymer capsules. ^[97] Some example for enzymatic reactions in microscale polymersomes are summarized in Table 3. ^[34]

Table 3. List of enzyme loaded micrometric polymer vesicles. Adapted with permission from ref [34]. Copyright (2018) Elsevier.

Polymer	Encapsulated protein	Organization	Permeabilization	Application	Ref.
PMOXA-PDMS-PMOXA	Horseradish peroxidase	Enzyme-loaded	OmpF	Model for artificial cell	[98]
PEO-PB	Catalase	Enzyme-loaded	Inherent and rupture	Model for cargo release	[99]
PLL, PMAc, PDA	Glutamate dehydrogenase, Glutathione reductase, β -galactosidase, Glucose oxidase, Catalase	Enzyme-loaded liposomes embedded within	Inherent	Model for artificial cell	[100]
PAH/PMA/PNMD/PEG-PDEAEMA-stat-BCP)	Catalase, Myoglobin, Glucose oxidase	Enzyme-loaded polymersomes embedded within	Temperature-driven and pH-driven	Model for artificial cell	[101]
PLL/Liposomes/PMA/PMAc/ PNVP	Glucose oxidase, Horseradish peroxidase	Enzyme-loaded	Inherent	Model for artificial organelle	[102]
PLL/Liposomes/PDA/PMA/PMAc	Catalase	Enzyme-loaded liposomes embedded within	Inherent	Model for tissue engineering/ cell structural support	[103]

An alternative to functionalizing polymersomes is incorporating surface ligands to mimic the behavior of immune cell targeting antigens as presented by Hammer et al, 2008 using avidin–biotin chemistry. [104] In another example, giant polymersomes were decorated with sugar moieties on their surface to interact with lectin-functionalized particles. [105] In a more advanced way, giant polymersomes were functionalized with heparin moieties to function as red blood cell mimics and inhibit malaria parasites. [106] Key examples of protocells made from giant polymer vesicles include demonstration of protein expression (actin monomer) via encapsulation of the whole expression machinery and building blocks, [107] energy (ATP) production, [108] signal transduction via responsive subcompartments, autonomous growth/blebbing/division [109] and beating. [110]

1.2.8. Compartmentalization within Cell Mimics

Synthetic multicompartament assemblies are referred to as multiple functional compartments in a single compartment (e.g. multivesicular vesicles), an important step towards the architectural mimicry of eukaryotic cells. The fabrication of

multicompartmentalized synthetic cell like system requires an elaborated methodology. [111, 112] Diverse systems based on a multicompartment architecture were reported including liposomes in liposomes (also known as vesosomes), [112, 113] polymersomes in liposomes, polymersomes in liposomes, liposomes in capsules, [114] polymersomes in capsules, [115] capsules in capsules, [116] cubosomes in capsules. [117] The use of capsules requires layer by layer deposition, [29, 118-120] with the drawback of requiring up to 50 steps for their fabrication. [111] Emulsion centrifugation was used for liposomes in polymersomes [112] and film rehydration method for polymersomes in liposomes [121] Vesosomes were historically the first compartmentalized systems [122] and can be prepared in various ways such as wrap them in cochleate cylinders, [123] the glass bead method, [124, 125] film rehydration [126] or internal bilayer partitions. [127] Polymersomes in liposomes, are maintained using the solvent switch method, [128] direct dissolution method, [129] double emulsion in water/oil/water system, [130] double emulsion via microfluids [130-132] and emulsion centrifugation method. [133] The film rehydration method provides the advantages to avoid traces of organic solvent and no oil phases or templates are necessary, which is essential for the encapsulation of biologically relevant molecules. All these techniques to form multicompartment structures listed above vary in size and number of compartments with various unique functions. [111, 134] Many limitations still affect the most common approaches and therefore, there is a need for an easy way with less barriers to allow the creation of a multicompartment cell-inspired scaffold with even more outstanding properties.

Responsive multicompartmental systems are of interest due to the controllability of content and release trigger, as well the connectivity between each subcompartments. Various strategies/technologies (described in Chapter 1) have been studied to engineer multi-step reactions within a confined space. The capability to sense and respond to their environment makes responsive multicompartment very attractive for the construct of artificial cells. Only few examples for stimuli responsive multicompartment systems are known so far. For example, simple responsive cellular mimics were proposed

using capsosome-based compartments loaded with stimuli-responsive adamantyl-modified polymersomes,^[101] capsules containing pH-dependent liposomes,^[135] lipid giant vesicles loaded with UV-responsive liposomes^[136] and microscale polymersomes encapsulated with temperature-dependent liposomes to trigger specific chemical reactions.^[112]

In addition, microfluidic techniques promise high encapsulation efficiency inside microcompartments and size monodispersity, but up to now, their production rates are low and with reduced diversity. Despite these promising examples, the potential of microscale multicompartments as novel functional materials is still restricted by a limited implementation of responsiveness to external stimuli, not taking advantage of the time dimension to modify the behavior and architecture of such multicompartments in a controlled manner.^[4]

1.2.9. Vesicular Cytoskeleton Mimics

Reconstitution studies of cytoskeletal components paves the way to understand the complex dynamics during shape changes of cell migration and cell division.

1.2.9.1. Bottom-Up Reconstitution of Cytoskeleton

Cytoskeleton component encapsulation in vesicular structures is an essential tool to study the complexity of each cytoskeletal element and their individual properties. Scientists use a bottom-up approach by reconstituting the cytoskeletal subunits into vesicular structures. In 1989, cytoskeletal proteins were encapsulated into lipid vesicles by Elson and co-workers, providing information about changes on vesicle shape due to encapsulated actin.^[137] The cytoskeleton construction inside liposomes is a non-trivial procedure, where numerous different methods exists according to literature.^[138] The process of encapsulation should not harm the cytoskeletal proteins and no unintended changes in the GUV properties.

Up to date, gentle hydration,^[139] electroformation,^[140] gel-assisted swelling,^[141, 142] droplet microfluidics^[143-145] and particularly conventional inverse emulsion^[76, 146-148]

approaches were reported for cytoskeletal component encapsulation. By the proof of principle studies, actin filaments were shown to influence mechanics of vesicular structures ^[140, 149] while little rheological studies for mechanical response in vesicular systems exist. ^[150-152] A recent example by Weiss et al includes microinjection of F-actin or polymerization during protocell formation using lipid-based GUV system produced via microfluidics and the help of copolymer-stabilized water-in-oil droplets, demonstrating a functional bottom-up assembly that would not self-assemble when simply mixed together. ^[153]

1.2.9.2. *In situ* Triggering of Cytoskeletal Polymerization

Another approach than encapsulation of cytoskeletal filaments is the *in situ* triggered polymerization of cytoskeletal components. Polymerization is slowed down by working at low temperatures ^[154] or by exchanging solution to initiate the filament formation by inserting pore-forming peptides or proteins into the membrane to transfer ions across the membrane. ^[155, 156] In various studies, actin polymerization was induced using self-propelled PS beads ^[157] or in lipid vesicles. ^[158] A study was reported, where G-actin was encapsulated in liposomes and the polymerization was induced by introducing Mg^{2+} via electroporation or ionophore mediated influx. ^[156, 159-161] More recently, Lee et al presented a photo-switchable ATP-generation coupled with actin filament production in liposome GUVs leading to its morphology changes and eventually rupture. This was achieved using magnesium ionophores in the membrane and G-actin in the lumen. ^[162] Dhir ^[136] et al demonstrated nanosized worm-shaped tubular vesicles (proteotubularsomes) including light induced ATP generation and actin polymerization. ^[163]

2. Aim of the Thesis

The aim of the research that is described in this thesis is the *de novo* design of a cell-inspired multicompartiment as a smart material that transduces a signal via triggered disruption of inner subcompartments and contributes towards the development of artificial cells. The development of cell mimics with the ability to sense changes in the environment and subsequently respond, find many useful applications and plays an important role to generate knowledge of complex biological processes in a molecular level and simplified communication pathways. This research area is still in its infancy and is limited by the low availability and low stability of materials and lack of *in situ* characterization methods. Nonetheless, this field may offer opportunities and substantial inroads for innovative strategies towards the development of a smart artificial cell. In recent years, biomimetic structures were built in a new way by combining chemical and biological components via a bottom-up approach.

The scope of this thesis addresses a new technology for the fabrication of a functional multicompartiment by self-assembling polymers that serve as building blocks. It is important to use a biodegradable and biocompatible basis to mimic biorelevant reactions. To do this, a strategy for the preparation of compartmentalized assemblies was elaborated where giant polymersomes (in the range of sizes of cells, micron-scale) serve as a basis/scaffold to further build a higher order complex organization loaded with synthetic nanostructures. This multicompartiment system has potential to perform cell-like functions and mimic a simple cellular architecture. Our aim is to use a non-assisted gentle film rehydration technique to simulate the self-assembly process found in nature. This formation method results in more polydisperse vesicles compared to other formation methods, such as microfluidics, but it allows to the use of mild, biologically relevant conditions and is easy to adapt to new conditions. Synthetic

materials can offer an additional feature of being responsive to an external trigger. In addition, it is desirable to minimize the complexity of the fabrication steps to achieve a smart material which fulfills application-oriented requirements. In this strategy, the combination of synthetic compounds (e.g. block copolymers, fluorescent dyes, dye coupled substrates) and biological elements (e.g. receptor like molecules, enzymes, ion channels) was chosen to study cell-relevant mechanisms.

The research presented in this dissertation aims to further advance the fields of cell mimics and to fulfill following goals (Figure 11):

- (i) The preparation and physicochemical evaluation of synthetic multicompartments formed by film rehydration method.
- (ii) Fine tuning of a responsive multicompartment to an external stimulus to release the cargo of the subcompartment.
- (iii) Introducing receptor like molecules on the membrane to interact with specific ligand.
- (iv) Inducing a compartmentalized primitive enzymatic activity
- (v) Recruiting an ion channel to allow on-demand flux of ions across the membrane of the multicompartment.
- (vi) Study artificially constructed cytoskeleton by initiating actin polymerization in multicompartments.

The bottom-up approach developed in this research aims at recreating cellular processes, starting from simplified compartmentalization. There is a tremendous interest to find innovative strategies to develop and carefully control such stimuli-responsive multicompartment systems to function as “cell mimics”. Inspired from nature, our purely polymeric self-assembled multicompartment structure is equipped with fine-control over outer and inner compartment responsiveness, essentially

mimicking cellular signaling transduction pathways. The combination of compartmentalization and stimuli responsiveness allows complex signal transduction in an artificial polymer system and is a high impact strategy to have multifunctional applications. Eventually, our responsive multicompartments could be suitable as a framework within the ultimate goal creating of an artificial cell. The findings of this thesis are presented in the following chapters.

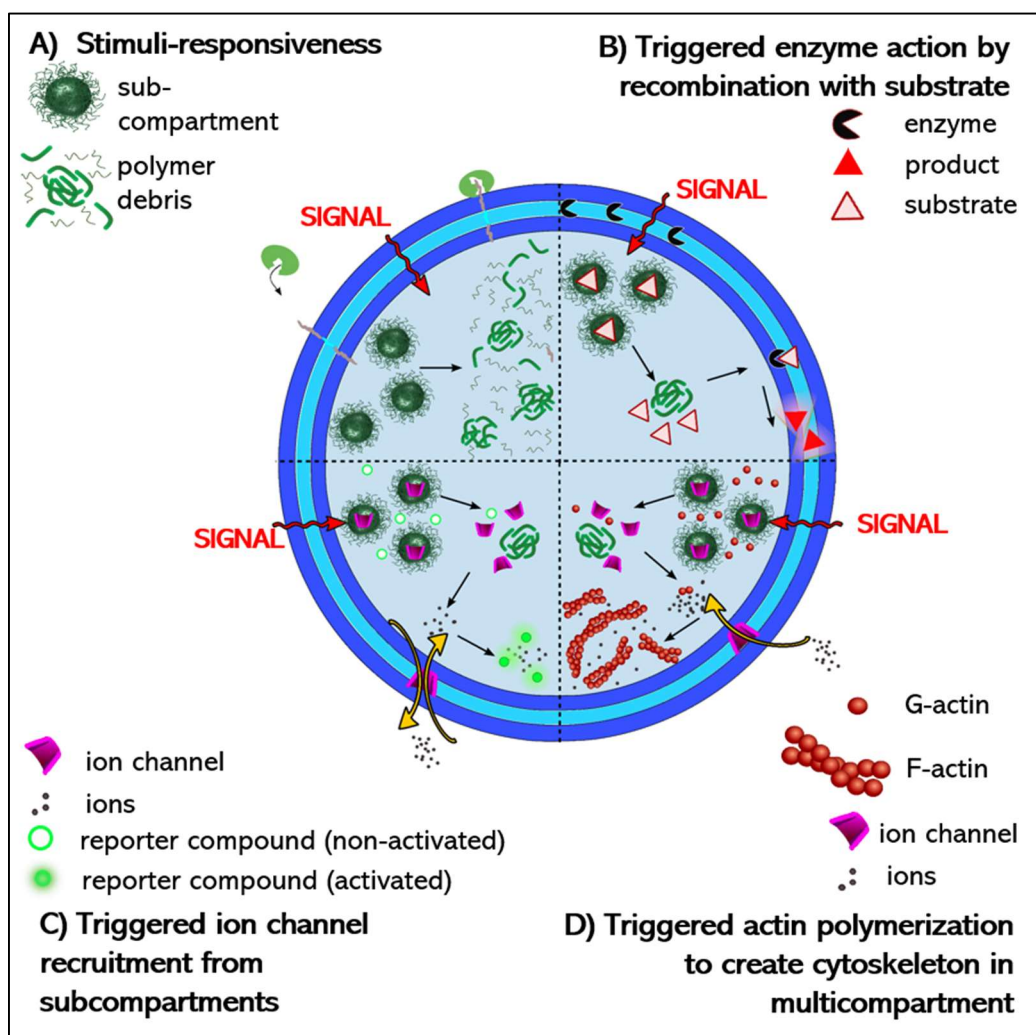
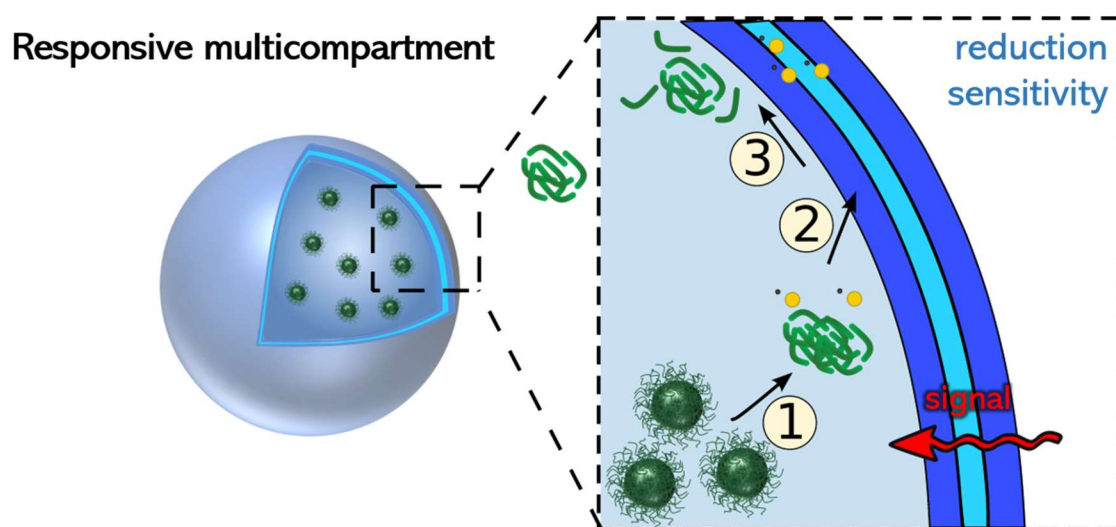


Figure 11. Schematic overview of a polymer vesicle based protocell. A modular multicompartiment system composed of reduction sensitive subcompartments encapsulated within polymeric giant unilamellar vesicles for triggered enzymatic activity, ion channel recruitment or cytoskeleton formation. The reducing agent DTT was used as the signal (red arrow) that passively traverses the polymeric GUV membrane without addition of biopores or channels.

All raw data of the results are saved in the following server: \\131.152.106.67 and in external hard drives.

3. Self-Assembly and Characterization of Stimuli- Responsive Multicompartments

Next generation multifunctional materials will be built from hierarchical assemblies of multicomponent and stimuli-responsive systems. In this work, purely polymer-based multicompartment systems were obtained by introducing various subcompartments (nanoparticles, micelles, polymersomes), optionally with stimuli-responsive properties into the lumen of receptor decorated giant unilamellar vesicles (GUVs) via film rehydration method and characterized by fluorescence correlation spectroscopy and confocal laser scanning microscopy.



PARTS OF THIS CHAPTER HAVE BEEN PUBLISHED AND REPRINTED HEREIN WITH PERMISSION FROM REFERENCE [1]. COPYRIGHT (2019) JOHN WILEY AND SONS:

SAGANA THAMBOO, ADRIAN NAJER, ANDREA BELLUATI, CLAUDIO VON PLANTA, DALIN WU, IOANA CRACIUN, WOLFGANG MEIER^x AND CORNELIA G. PALIVAN^x. MIMICKING CELLULAR SIGNALING PATHWAYS WITHIN SYNTHETIC MULTICOMPARTMENT VESICLES WITH TRIGGERED ENZYME ACTIVITY AND INDUCED ION CHANNEL RECRUITMENT, *ADVANCED FUNCTIONAL MATERIALS*, 2019, 1904267.

PARTS OF THIS CHAPTER ARE A MANUSCRIPT IN PREPARATION:

SAGANA THAMBOO*, ANDREA BELLUATI*, ADRIAN NAJER, VIVIANA MAFFEIS, CLAUDIO VON PLANTA, IOANA CRACIUN, CORNELIA G. PALIVAN^x, WOLFGANG MEIER^x, MULTICOMPARTMENT POLYMER VESICLES WITH ARTIFICIAL ORGANELLES FOR SIGNAL-TRIGGERED CASCADE REACTIONS INCLUDING CYTOSKELETON FORMATION, *ADVANCED FUNCTIONAL MATERIALS*, 2020, 2002949.

**These authors contributed equally*

3.1. Introduction

The spatiotemporal separation of biochemical reactions plays a fundamental role in nature: their compartmentalization allows the steering of reaction kinetics via controlled diffusion through specialized microenvironments, while also protecting their content from degrading agents or generally incompatible compounds.^[100] Due to their importance in nature, both compartmentalization, at the micro and nanoscale, and stimuli-responsiveness are a source of inspiration for development of advanced functional materials.^[7] In particular, stimuli-responsive single polymer-based nanocompartments were proposed as drug delivery systems,^[164] nanoreactors,^[34] artificial organelles^[165]/cells,^[166] depending on their payload and the properties of their membrane.

Here, multicompartments based on hierarchical compartment organization have been introduced with a long-term goal of designing simple artificial cells as tools to better understand natural mechanisms and provide innovative solutions for biomedical and chemical challenges.^[29] Polymeric giant vesicles were loaded with dye-encapsulated nanoscale subcompartments (polymersomes, micelles or reduction sensitive nanoparticles). Heparin moieties serve as molecular recognition module on the surface of the giant vesicles. Hierarchical assembly and subcompartment responsiveness were characterized in detail by using confocal laser scanning microscopy (CLSM) coupled with *in situ* single-particle detection method, fluorescence correlation spectroscopy (FCS), directly within the lumen of the micron-scaled multicompartment assemblies. This is a unique direct measure of inner compartment integrity, dynamics and responsiveness within the final multicompartment assembly, which is typically extremely challenging to study *in situ* with other techniques. A microscale reactor capable of predictable self-regulation would thus be an important step in the development of materials with a smart behavior.^[1]

3.2. Results and Discussion

3.2.1. Multicompartment Self-Assembly: Loading

Synthetic Giant Vesicles with Subcompartments

The production of multicompartmentalized synthetic giant unilamellar vesicles (GUVs) that expose receptor-like molecules on the polymer membrane and contain subcompartments, was achieved by formation of GUVs loaded with prior self-assembled nanoscale assemblies (polymersomes, nanoparticles and micelles) (Figure 12A).

GUVs were self-assembled from a mixture of PMOXA₅-*b*-PDMS₅₈-*b*-PMOXA₅ and PDMS₆₅-*b*-heparin co-polymers (8 wt%), ^[167] the latter negatively charged copolymer serving to expose heparin on the GUV membrane as a mimic for heparan sulfate, known to be exposed on the plasma membrane of most cell types. ^[168]

First, we investigated the self-assembly of empty GUVs formed by gentle film rehydration method in order to optimize formation of unilamellar vesicles. After drying the copolymer film under vacuum overnight to eliminate traces of organic solvents, a rehydration solution was added to induce the self-assembly process at room temperature, and CLSM was used to characterize the resulting system (Figure 12B). When used as a rehydration solution, water and PBS buffer generated a mixture of various assemblies, ranging from multilamellar vesicles up to polymer junk and filled assemblies (Figure 13B, C). According to CLSM micrographs, the use of increasing concentrations of sucrose (30 - 300 mM) decreased the fraction of multivesicular and multilamellar giant vesicles, while increasing the fraction of unilamellar giant vesicles (Figure 12D-G). The optimum sucrose concentration of 300 mM predominantly induced the formation of unilamellar GUVs (Figure 12C, Figure 13A) and thus was further used for generating multicompartments. According to cryonic transmission electron

microscopy (cryo-TEM) images, the membrane thickness of the extruded synthetic GUVs is approximately 11 nm (Figure 13D).

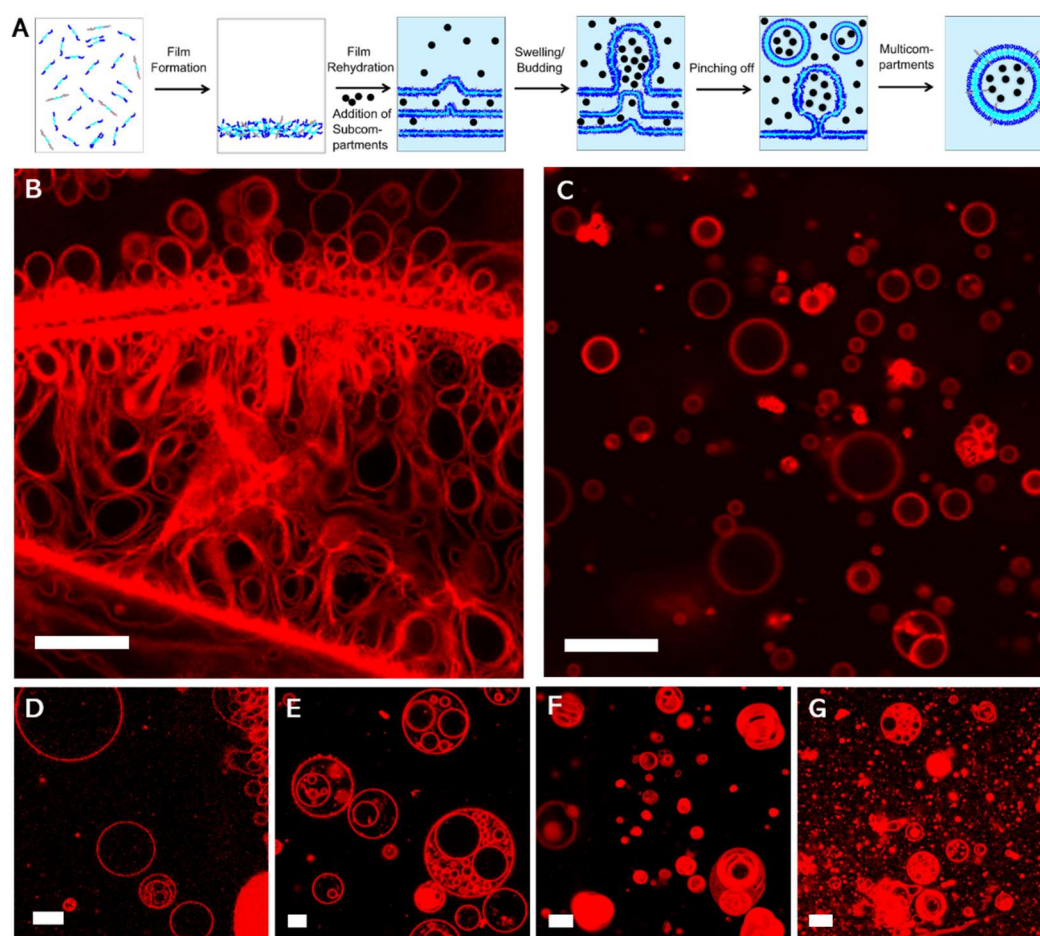


Figure 12. Self-assembly of giant vesicles using film rehydration method. **(A)** Illustration of the formation of multicompartment. The block copolymer mixture was dissolved in an organic solvent, which was evaporated to form a thin dry polymer film. Subsequently, a rehydration buffer including smaller nanocompartments (black dots) and sucrose, was added to induce self-assembly. The swollen film started to form buds followed by pinching-off of the buds to form multicompartment. **(B-G)** CLSM images of GUVs. To enhance visualization of the structures, we added the hydrophobic fluorophore Bodipy630/650 (red) that inserts into the vesicle membrane. GUVs were formed **(B)** directly in the observation chamber of an 8-well plate in 300 mM sucrose and **(C-G)** in rehydration solutions with decreasing concentration of sucrose in vials: **(C)** 300 mM sucrose, **(D)** 200 mM sucrose, **(E)** 100 mM sucrose, **(F)** 60 mM sucrose and **(G)** 30 mM sucrose. Scale bar, 20 μm .

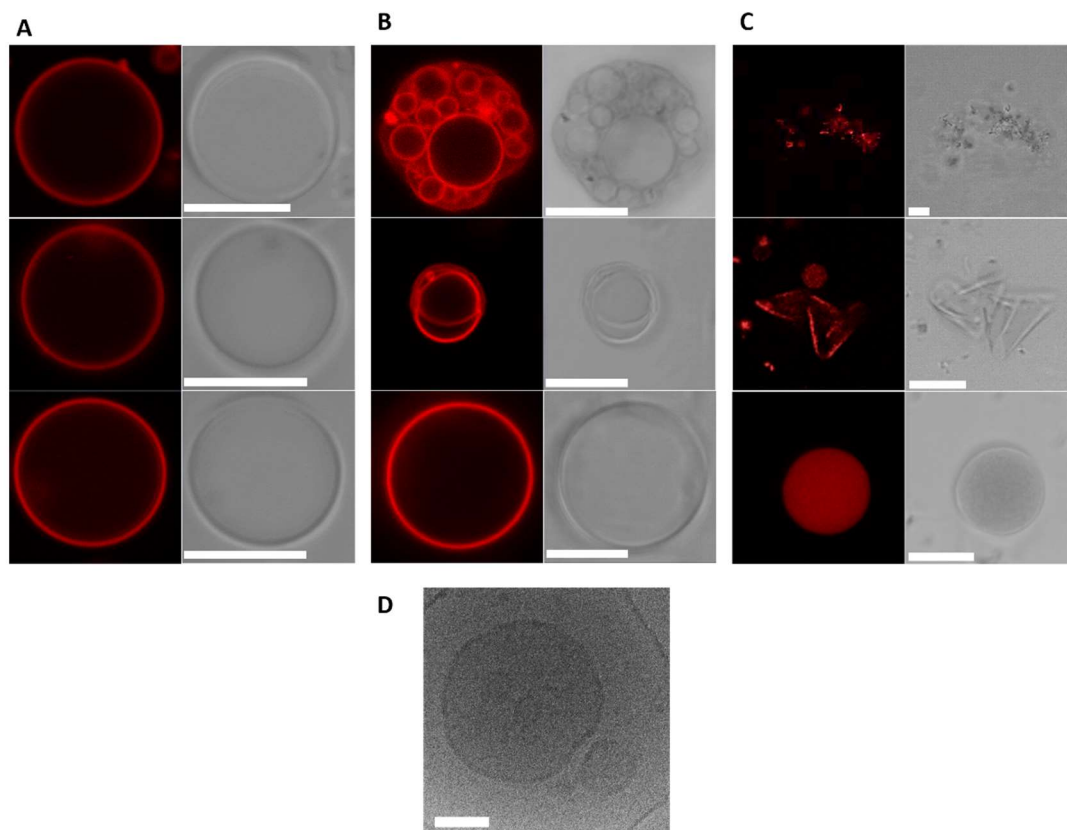


Figure 13. GUV characterization by CLSM and cryo-TEM of extruded GUV. (**A-C**) Optimization of GUV production with CLSM image of GUVs (left) and corresponding bright field image (right). GUVs were formed in (**A**) a 300 mM sucrose (resulting giant unilamellar vesicles), (**B**) pure water (resulting mixture of multivesicular, multilamellar and unilamellar vesicles) and (**C**) PBS (resulting polymer junks and filled structures) using the gentle film rehydration method. Scale bar 10 μm . (**D**) Cryo-TEM of the giant membrane (extruded, 400 nm) after rehydration in sucrose. The membrane thickness is approximately 11 nm. Scale bar, 100 nm.

To investigate the accessibility of the receptor-like molecule heparin on the GUVs membrane, we examined its interaction with protamine, a positively charged peptide known to bind to the negatively charged heparin.^[169] Empty GUVs assembled in the presence and absence of PDMS₆₅-*b*-hep, were first mixed with Bodipy630/650, a fluorescent hydrophobic molecule that aids in the visualization of formed GUVs, and then with Oregon Green 488 (OG488) labeled protamine. CLSM micrographs of individual GUVs reveal co-localization of OG488-protamine and Bodipy630/650 fluorescent signals only at the membrane of GUVs containing PDMS₆₅-*b*-hep (Figure 14). This indicates a specific membrane binding interaction between heparin-exposing GUVs and the peptide, while there was no unspecific binding between heparin-free GUVs and the peptide. A similar behavior was previously reported when heparin

attached GUVs were mixed with malaria parasite ligands. ^[106] By mimicking cell membrane receptor-exposure, we now have a tool to probe heparin-binding interactions with various biologically active ligands that will support further development of such GUVs for medical applications.

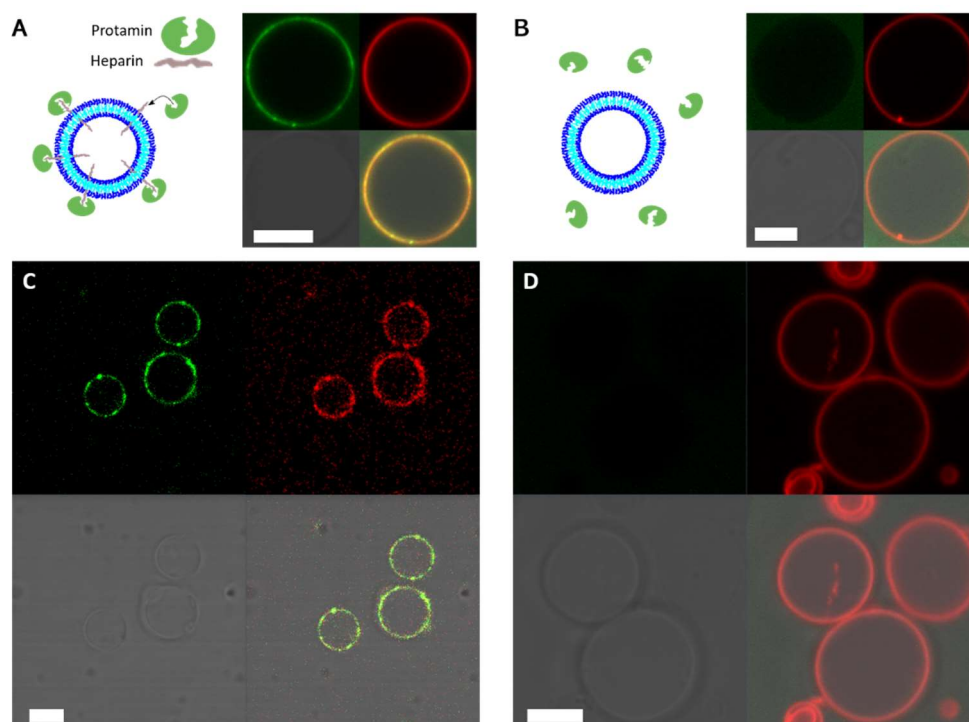


Figure 14. Membrane functionalization of GUVs (red, top right) with heparin and interaction with protamin-OG488 (green, top left) with corresponding bright field image (bottom left) and merge (bottom right). CLSM image of the heparin-decorated (**A, C**) and heparin-free giant vesicles (**B, D**). Scale bar 5 μm .

We then loaded nanoassemblies into GUVs with the intention of creating a multicompartmentalized architecture (Figure 15A). Depending on the chemical nature of the copolymers and their molecular properties, various nanoassemblies were formed: i) reduction-sensitive nanoparticles (*NP-Graft*) based on $(\text{poly}(2\text{-methyl-2-oxazoline})_{88}\text{-graft}(\text{SS})\text{-poly}(\epsilon\text{-caprolactone})_{238})$ (PMOXA_{88-g(SS)}-PCL₂₃₈), ii) non-sensitive nanoparticles (*NP-Control*) based on $\text{poly}(2\text{-methyl-2-oxazoline})_{30}\text{-block-poly}(\epsilon\text{-caprolactone})_{62}$ (PMOXA_{30-b}-PCL₆₂), iii) micelles resulting from PDMS_{65-b}-heparin (*M100*) and iv) polymersomes formed from a mixture of PMOXA_{5-b}-PDMS_{58-b}-PMOXA₅ combined with 5% or 25% PDMS_{65-b}-heparin (*Ves5* and *Ves25*, respectively).

^[167, 170] We investigated the architecture and size of these nanoassemblies by a

combination of transmission electron microscopy (TEM) and dynamic light scattering (DLS). TEM micrographs indicated the formation of spherical nanoparticles and DLS revealed hydrodynamic diameters of 52 ± 23 nm (for NP-Graft), and 104 ± 40 nm (for NP-Control). The hydrodynamic diameter of micelles M100 was 99 ± 34 nm, while polymersomes had diameters of 142 ± 55 nm (for Ves5) and 159 ± 57 nm (for Ves25), in agreement with our previous conclusions. ^[167, 170] Hydrophobic Bodipy630/650 was entrapped in the core of both types of nanoparticles (NP-Graft and NP-Control), while OG488 was incorporated in M100, Ves5 and Ves25 to allow their investigation by FCS.

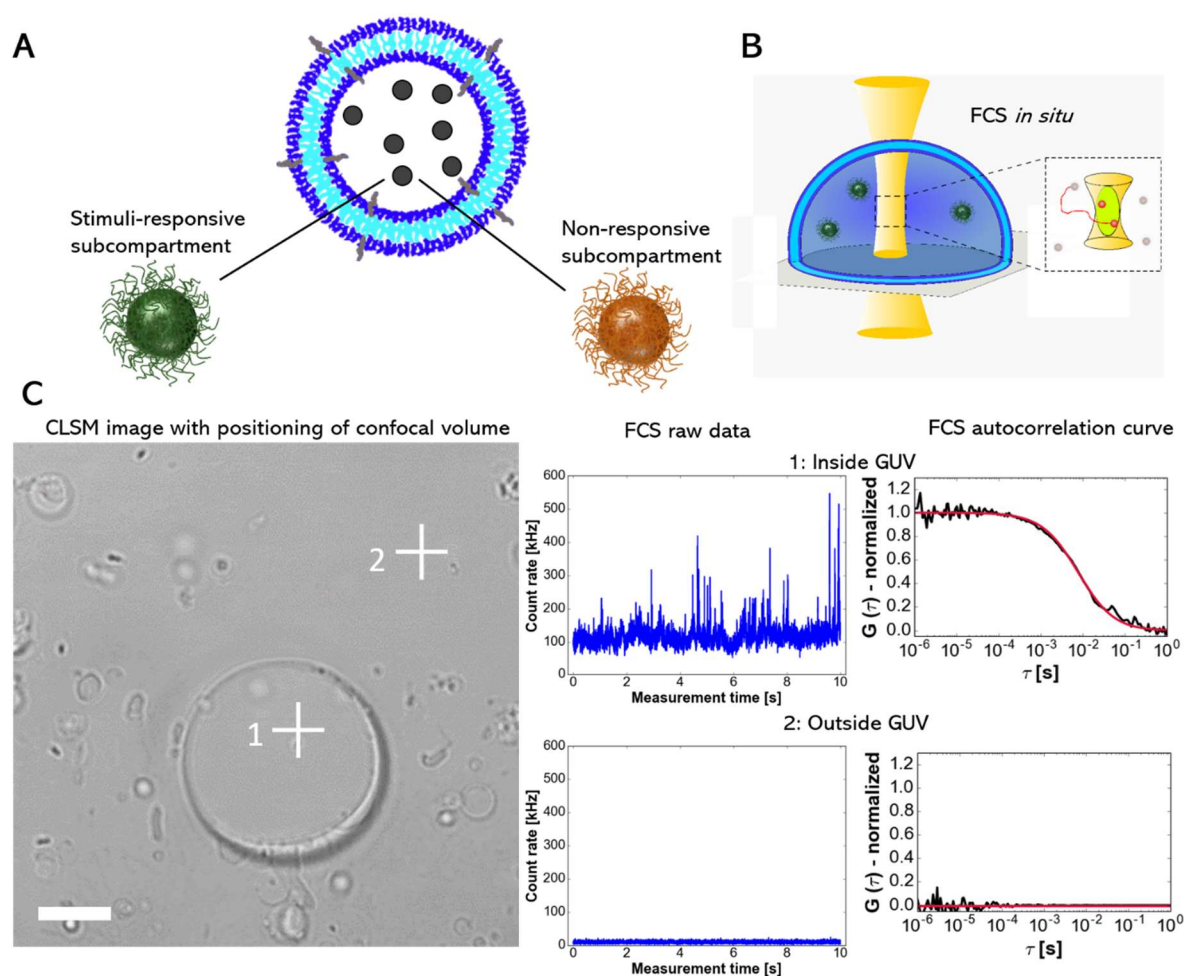


Figure 15. Schematic illustration and characterization of multicompartment vesicles. (A) Multicompartment, where subcompartments (e.g. stimuli responsive NP-Graft or non-responsive NP-Control) are loaded into a polymeric giant vesicle. (B) In depth *in situ* analysis of subcompartments in a giant vesicle with FCS/CLSM by localizing the confocal volume into the GUV cavity. (C) FCS measurement in combination with CLSM mode of subcompartments in giant vesicles and its surrounding solution. FCS raw data and autocorrelation curves inside and outside of the NP-Graft loaded giant vesicle. Diffusion time inside the GUV was 5257 ± 1517 μ s; outside measurement gave no correlation curve indicating diffusing fluorescent species is at a concentration below the detection limit. Count rate inside was 101 ± 9 kHz and outside was 0.7 ± 0.5 kHz. Scale bar, 10 μ m.

Synthetic multicompartments were formed by slowly adding a 300 mM sucrose solution containing fluorescently labeled nanoassemblies to a polymer film (PMOXA₅-*b*-PDMS₅₈-*b*-PMOXA₅ with 8 wt% PDMS₆₅-*b*-heparin) followed by rehydration overnight at 22°C. Each type of nanoassembly (nanoparticles, micelles and polymersomes) was separately loaded into GUVs (4–50 μm) and investigated by *in situ* FCS to directly measure their dynamics inside the giant vesicles, prior localized by CLSM (Figure 15B). In FCS, the fluctuation of the fluorescence intensity of fluorophores due to Brownian motion is measured in the femtolitre-sized confocal volume.^[171] Freely diffusing fluorescent molecules can be distinguished from fluorophores inserted in membranes or encapsulated in nanoassemblies by a difference in their diffusion times.^[172, 173] As the autocorrelation function analysis allows for an estimation of the hydrodynamic diameter of the fluorescent molecules/assemblies passing through the confocal volume, we used it to follow the nanoassemblies located inside GUVs. We placed the small confocal volume (about 300 nm x-y dimension and 1 μm height)^[171] inside the cavity of the GUV to precisely measure the presence, size and stimuli-responsiveness of the nanoassemblies serving as subcompartments (Figure 15B). Only unilamellar, stable and non-moving giant vesicles with a minimum diameter of 4 μm were selected for FCS measurements. Smaller GUVs were not suitable, because the center of the vesicle was not distinguishable from the membrane and the confocal volume approaches the size of the aqueous inner compartment. As we precisely positioned the confocal volume inside the cavity of the GUVs, the removal of non-encapsulated nanoassemblies was not necessary for FCS measurements and was disregarded by the space precision (Figure 15C). In addition, the concentration of the non-encapsulated nanoassemblies in the surrounding solution of the GUVs, after the dilution required for FCS measurements, was below the detection limit. NP-Graft diffused inside GUVs with a diffusion time of 5257 ± 1517 μs (average count rate of 101 ± 9 kHz), while measurements performed outside of the GUVs did not yield an autocorrelation curve. Only background signal was detected (average count rate = 0.7 ± 0.5 kHz), confirming the encapsulation of

the subcompartments inside the cavity of GUVs and no non-encapsulated subcompartment were detectable in the surrounding GUV solution.

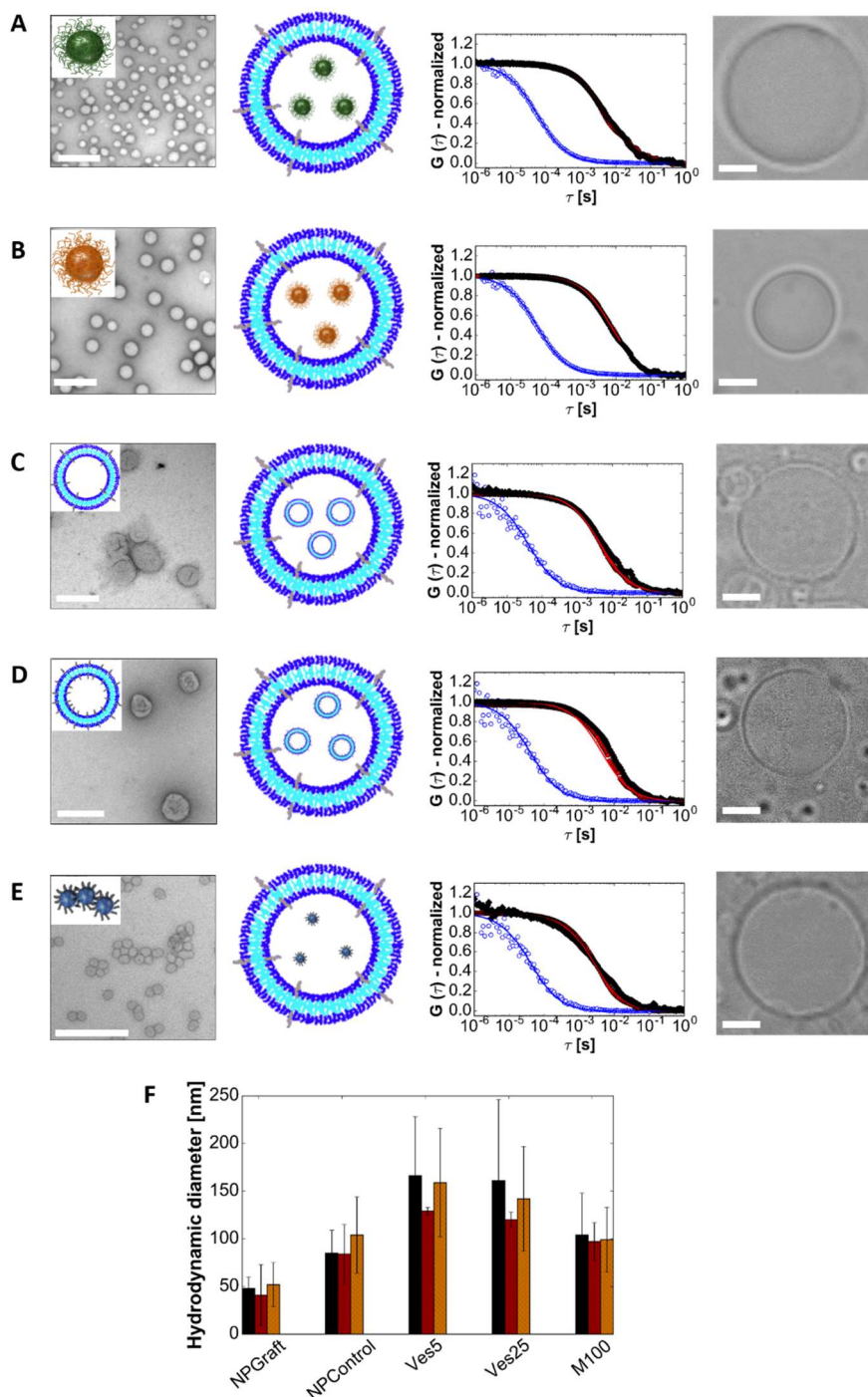


Figure 16. Characterization of multicompartment. (A-E) Transmission electron micrograph and schematic illustration of nanoassemblies followed by schematic illustration of multicompartment (left column). FCS measurement in combination with CLSM mode of subcompartments inside giant vesicles (right column). For the FCS measurements: normalized autocorrelation curves are shown with symbols, corresponding fits as solid lines, measurements of the free dye in blue, the nanoassemblies inside giant vesicles in black, and the free nanostructures in solution in red (right column). (A) NP-Graft, (B) NP-Control, (C) Ves5 (5%-Heparin vesicles), (D) Ves25 (25%-Heparin vesicles) and (E) M100 (100%-Heparin micelles) loaded in giant vesicles. Scale bar, 200 nm for TEM and 5 μ m for CLSM images. (F)

Comparison of the hydrodynamic diameter determined from FCS measurements of nanostructures inside giant vesicles (black bars), in solution (red bars), and from DLS measurements of nanostructures in solution (yellow bars). Values are indicated as mean \pm standard deviation.

The dynamics of free or encapsulated nanoassemblies, the diffusion times of free dye and free nanoassemblies in solution were compared to those inside of multicompartment GUVs (Figure 16A-E). The autocorrelation curves of encapsulated nanoassemblies were similar to those of freely moving nanoassemblies in solution, as their diffusion times were preserved upon encapsulation. Consistently, the hydrodynamic diameters calculated for the nanoassemblies inside GUVs were comparable to those from DLS data obtained for the free nanoassemblies in solution (Figure 16F). This data agrees with the values reported previously. ^[167]

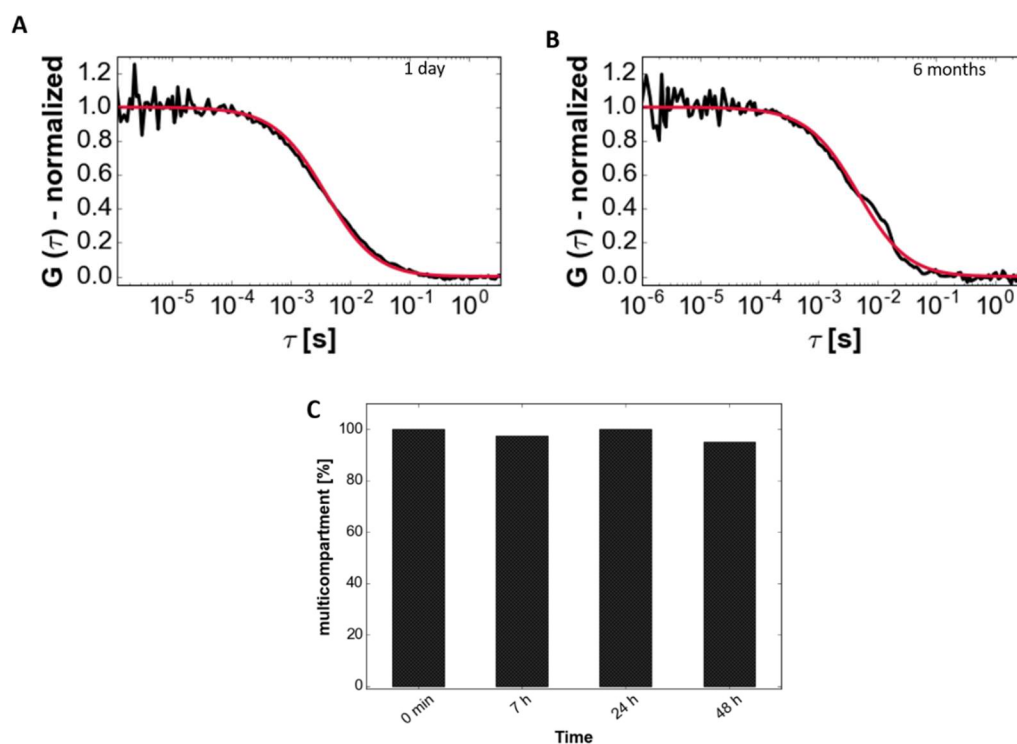


Figure 17. Stability and loading efficiency of multicompartments determined with FCS measurements and CLSM mode. **(A)** Autocorrelation curve of freshly formed NP-Graft loaded in giant vesicle. Diffusion time = 4066 ± 1265 μ s. **(B)** Autocorrelation curve of NP-Graft in giant vesicle 6 month after formation. Diffusion time = 3437 ± 945.0 μ s. **(C)** NP-Graft loaded giant vesicles can be observed in over 95% of the samples and stay stable at least 48 h in the observation chamber. Number of particles: $N > 0$. Mean of 40 giant vesicles per time point.

The subcompartments freely diffused within the lumen of the GUVs and did not aggregate inside. In addition, the subcompartments remained intact within the GUVs and preserved their architecture at least six months (Figure 17A, B). We also estimated

the encapsulation efficiency by analyzing 40 giant vesicles in PBS with size $>4 \mu\text{m}$. According to our FCS data, in 95% of measured giant vesicles, we found loaded NP-Graft (Figure 17C).

3.2.2. Multicompartments with two different Subcompartments

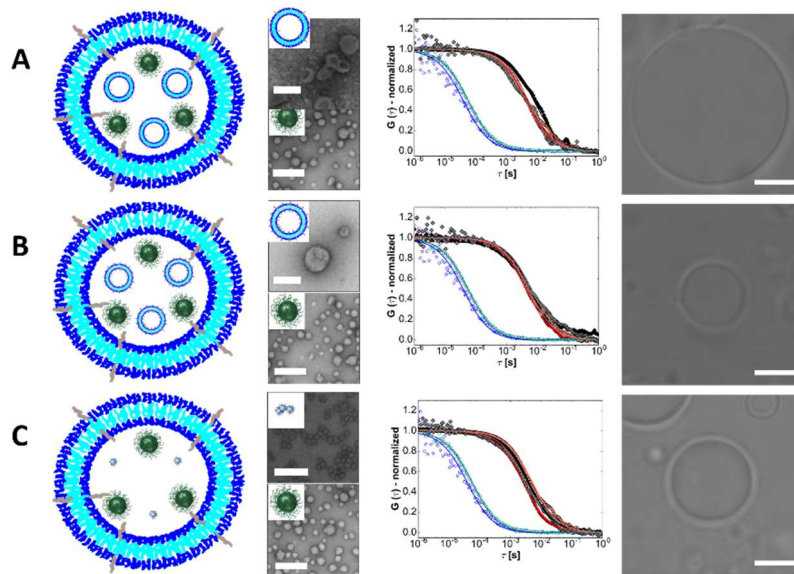


Figure 18. Characterization of multicompartments formed by loading GUVs with two different nanoassemblies (reduction-sensitive nanoparticles and non-reduction sensitive heparin nanostructures). Schematic illustration of multicompartiment followed by transmission electron micrograph of each nanoassembly (left column). FCS measurement in combination with CLSM mode to quantify subcompartments inside giant vesicles (right column). For the FCS measurements: normalized autocorrelation curves are shown with symbols, corresponding fits as solid lines, measurements of the free dye (OG488 in blue, Bodipy630/650 in light blue), the nanoassemblies inside giant vesicles (OG488 loaded heparin nanostructure in black, Bodipy630 loaded NP-Graft in grey), and the free heparin nanostructures in solution (OG488 loaded heparin nanostructure in red, Bodipy630 loaded NP-Graft in light red), (right column). NP-Graft was co-loaded with (A) Ves5 (5%-Heparin vesicles), (B) Ves25 (25%-Heparin vesicles) and (C) M100 (100%-Heparin micelles) in giant vesicles. Scale bar, 200 nm for TEM and $5 \mu\text{m}$ for CLSM images.

Next, we herein report the fabrication of a two-type responsive multicompartments, the evolution of our previously described multicompartments.^[1] The membrane of the microscale polymer GUVs was formed from a mixture of $\text{PMOXA}_5\text{-}b\text{-PDMS}_{58}\text{-}b\text{-PMOXA}_5$ and $\text{PDMS}_{65}\text{-}b\text{-heparin}$ co-polymers and used to load two kinds of subcompartments, such as fluorescently labelled reduction sensitive nanoparticles (NP-

Graft) and heparin-exposing nanostructures were simultaneously used as subcompartments of GUVs (Figure 18A-C). The heparin-nanostructures were composed of polymersomes formed from a mixture of PMOXA₅-*b*-PDMS₅₈-*b*-PMOXA₅ combined with 5% or 25% PDMS₆₅-*b*-heparin (**Ves5** and **Ves25**, respectively) and micelles resulting from pure PDMS₆₅-*b*-heparin (M100), while NP-Graft was based on the graft copolymer PMOXA₈₈-*g*(SS)-PCL₂₃₈, whose disulfide bridge disconnects in a reductive environment, which disassembles the particles. The latter is thus the responsive subcompartment; NP-Graft can be loaded with several hydrophobic compounds (dyes, substrates, biopores). ^[1, 170]

The two-type multicompartments were first characterized by in situ FCS assisted by CLSM to monitor the changes in diffusion time, corresponding size, and number of loaded subcompartments over time (Figure 18A-C, Table 4). Additionally, we loaded two polymersomes-based subcompartments (Ves5), each carrying a different fluorophore (Bodipy 630/650 and OG488), to visualize both the compartments at once, with CLSM (Figure 19). The results are in agreements to what was discussed above for the one-type multicompartment. ^[1] The non-encapsulated nanoassemblies are in low concentration and not detectable by FCS. We have demonstrated the robustness of our detection system, where the fluorescently labelled subcompartments can be tracked *in situ*.

Table 4. Diffusion time and hydrodynamic diameter obtained from FCS measurements inside of two-type multicompartments. Each NP-Graft was loaded with Bodipy630 and heparin nanostructures (Ves5, Ves25 or M100) were loaded with OG488 to distinguish both types of nanostructures within the same GUV. (Values are indicated as mean \pm standard deviation; data for compartment in bold is given in table).

Multicompartments	Diffusion time (ms)	Hydrodynamic diameter (nm)
MC-(NP-Graft)+ Ves5	5514 \pm 1407	204 \pm 52
MC-NP-Graft +(Ves5)	5685 \pm 1477	81 \pm 21
MC-(NP-Graft)+ Ves25	3157 \pm 2367	117 \pm 88
MC- NP-Graft +(Ves25)	5558 \pm 1487	80 \pm 21
MC-(NP-Graft)+ M100	3408 \pm 1375	126 \pm 51
MC- NP-Graft +(M100)	3140 \pm 931	45 \pm 13

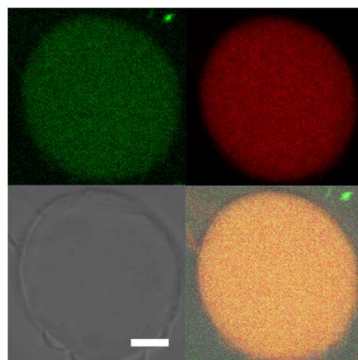


Figure 19. CLSM image of a two-type multicompartiment with OG488 loaded Ves5 (top left, green) and Bodipy630/650 loaded Ves5 (top right, red), bright field (bottom left) and its merge (bottom right). Scale bars 5 μm .

3.2.3. Stimuli Responsiveness - Triggerable

Multicompartments with Reduction-Sensitive Inner Subcompartments

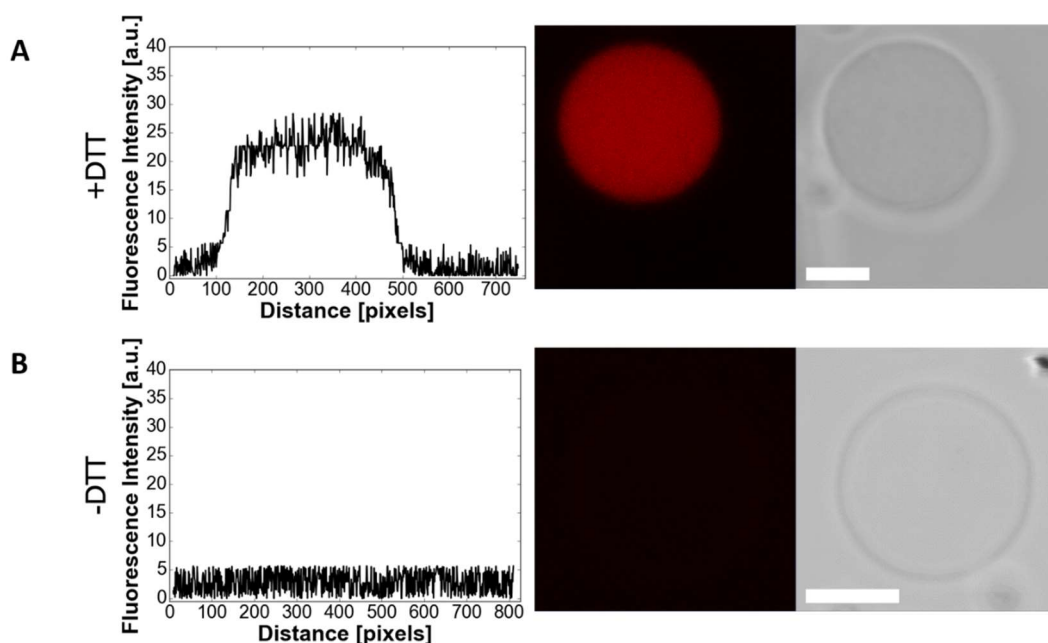


Figure 20. Reduction responsiveness of multicompartments in absence of biopores or ion channel. (**A**, **B**) Resazurin loaded giant vesicles analyzed by CLSM. Plot profile of the fluorescence intensity along the diagonal of the image (left), CLSM image of resazurin filled giant vesicles (middle) and corresponding bright field image (right): (**A**) In the presence of 10 mM DTT after 2 h incubation and (**B**) in the absence of reducing agents after 2 h incubation. Scale bars, 5 μm .

In order to achieve stimuli-responsive multicompartments mimicking a simple signaling reaction as in cells, we encapsulated stimuli-responsive subcompartments (NP-Graft) inside GUVs with the aim of inducing their disassembly in the presence of a specific external stimulus.

First, we evaluated the controlled diffusion of reducing agents (external stimulus) through the polymer membrane of GUVs by encapsulating a reduction-sensitive fluorophore resazurin (RZ) as a reporter compound inside GUVs. RZ is converted into the fluorescent resorufin product under reducing conditions (Figure 20A, Figure 21A, B), while it is non-fluorescent in non-reducing environment (Figure 20B, Figure 21C). We added dithiothreitol (DTT) or glutathione (GSH) as reducing agents to the outside of RZ-loaded GUVs, at specific concentrations similar to the physiological concentration of GSH in the cell cytosol. ^[174, 175] The fluorescence intensity, associated with resorufin production, increased already 2 h after addition of DTT, indicating that the reductive agent diffused through the polymer membrane and converted RZ inside GUVs with and without the exposed heparin (Figure 21A, B). On the contrary, GSH showed no effect even after 72 h (Figure 21D), most probably due to its higher molecular weight and charged residues. ^[176] This behavior is in agreement with reports indicating that exogenous tripeptide GSH does not penetrate the cell membrane, whereas the reducing agent DTT can cross it, ^[176-179] highlighting a similarity between natural and synthetic polymer based membranes.

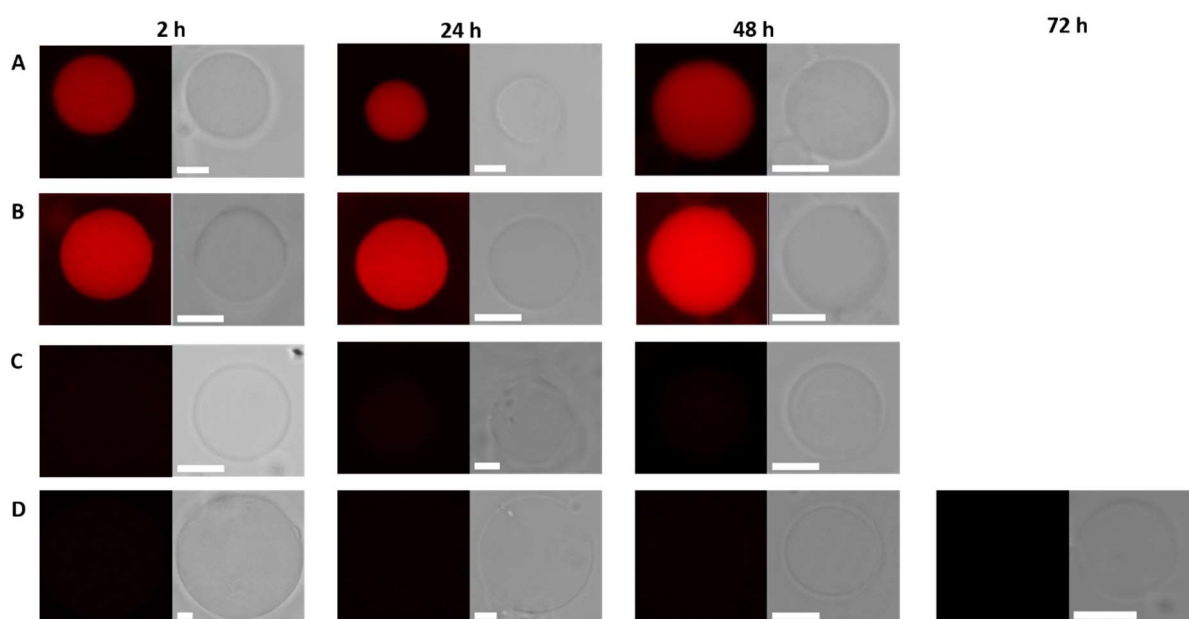


Figure 21. Reduction responsiveness of resazurin loaded giant vesicles over time. CLSM image of resazurin filled giant vesicles (left) and corresponding bright field image (right): (A) In the presence of 10 mM DTT, (B) in the presence of 10 mM DTT where no heparin moieties were present in the giant’s membrane, (C) in the absence of reducing agents, (D) in the presence of 10 mM GSH. Scale bars, 5 μ m.

We achieved the selective diffusion of DTT across the polymer membrane, otherwise impermeable to other molecules with higher molecular weight. We then encapsulated NP-Graft nanoparticles as subcompartments inside GUVs and studied the action of external DTT on their integrity when loaded with Bodipy630/650 as model molecule. Molecular brightness (counts per molecule) values obtained by FCS measurements were used to get an estimate for number of Bodipy630/650 per NP-Graft, which resulted in 46 dye molecules per NP-Graft.

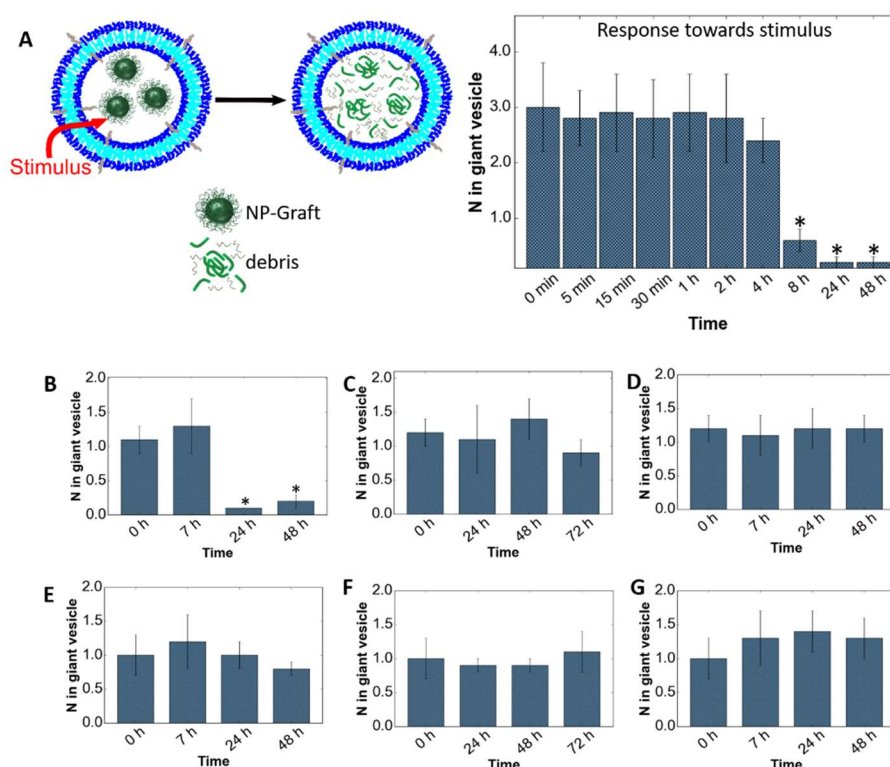


Figure 22. Nanocompartments loaded in giant vesicles. The signaling cascade is illustrated by the schematic. The number of particles (N) in the confocal volume (blue bars) of NP-Graft in giant vesicles were studied by FCS with CLSM mode. Mean of 40 giant vesicles per time point were measured during a 48 h period in presence of 10 mM DTT. The FCS data of the reduction sensitive multicompartment was analyzed where the number of particles (N, blue bars) of NP-Graft encapsulated in giant vesicles were measured at following conditions over time: (A) in presence of 10 mM DTT (B) in presence of 10 mM DTT with no heparin moieties in the giant's membrane and (C) in presence of 10 mM GSH and (D) in absence of any reducing agents. As a control the FCS data of the non-reduction sensitive NP-Control in giants was acquired at the following conditions: (E) in presence of 10 mM DTT, (F) in presence of 10 mM GSH and (G) in the absence of any reducing agents. Statistical comparison of the reduction responsive multicompartment (mean of 40 giant vesicles per time point) and its controls was performed using one-way ANOVA followed by Tukey's HSD test, $p < 0.05$. Significant difference relative to time point at 0 min.

Time-resolved FCS measurements performed inside GUVs revealed that addition of DTT to multicompartment induced a significant decrease in the number of

Bodipy630/650-loaded NP-Graft particles inside the observation volume to almost 0 after 24 h incubation (average of 40 GUVs/time point, Figure 22A). The disulfide bonds that connect hydrophilic and hydrophobic polymers of NP-Graft were cleaved and induced the rupture of NP-Graft subcompartments. In addition, a significant decrease in the count rate was observed after 24 h incubation with 10 mM DTT (Figure 23A, B).

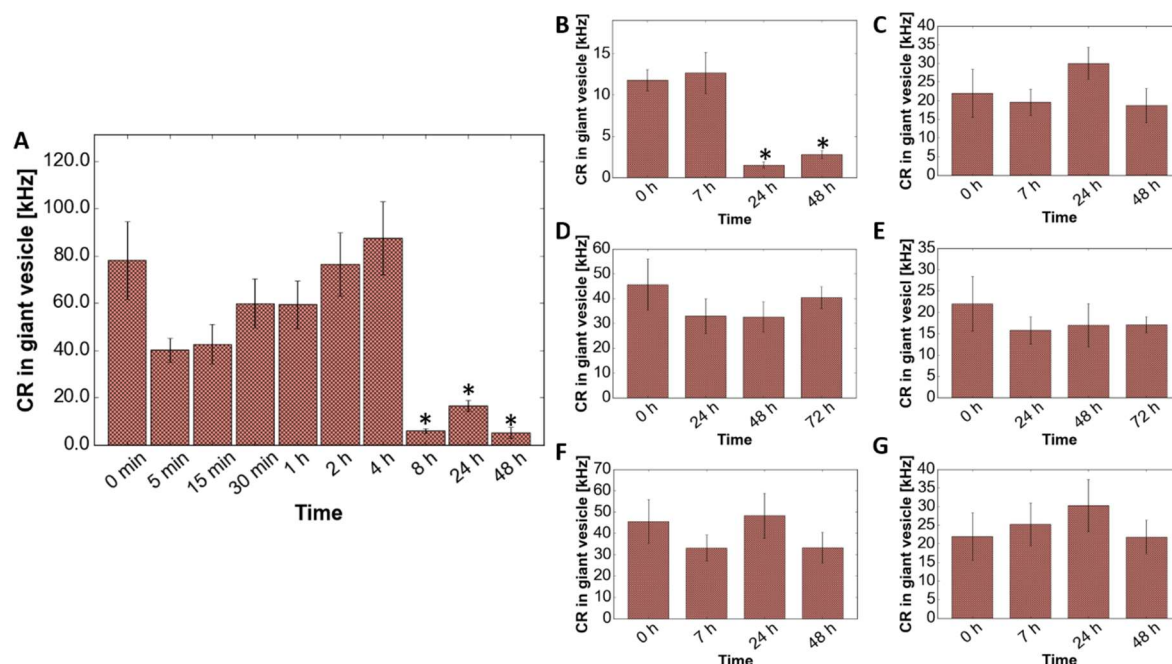


Figure 23. The FCS data of the reduction sensitive multicompartment were analyzed. Count rate (CR, brown bars) of NP-Graft encapsulated in giants were measured at following conditions over time: (A) in presence of 10 mM DTT, (B) in presence of 10 mM DTT with no heparin moieties in the giant's membrane, (D) in presence of 10 mM GSH and (F) in the absence of any reducing agents. As a control the FCS data of the non-reduction sensitive NP-Control in giants were acquired at the following conditions: (C) in presence of 10 mM DTT, (E) in presence of 10 mM GSH and (G) in the absence of any reducing agents. Statistical comparison of the reduction responsive multicompartment (mean of 40 giant vesicles per time point) and its controls was performed using one-way ANOVA followed by Tukey's HSD test, $p < 0.05$. Significant difference relative to time point at 0 min.

This decrease can be attributed to the migration of the hydrophobic Bodipy630/650 towards the GUV's membrane, once released upon disintegration of the NP-Graft. As expected, the nanoparticle disassembly was delayed when encapsulated within GUVs due to the additional barrier (GUV membrane). Indeed, in solution, the disassembly of NP-Graft nanoparticles and their content release was complete within 90 min,^[170] whereas it took 24 h to reach 90% for NP-Graft as subcompartments within GUVs.

More specifically, in an average GUV volume of $1112 \pm 407 \mu\text{m}^3$, the average nanoparticle number of 4082 ± 1051 initially encapsulated dropped to 80 ± 23 after 48 h in presence of DTT (Figure 24A). The triggered structural change of these subcompartments was successfully observed in individual GUVs by FCS. The presence of negatively charged heparin molecules on the polymer membrane did not impact the cleavage of the disulfide bonds of the NP-Graft inside the multicompartment system (Figure 22B, Figure 23B). When no reducing agent was added, NP-Graft subcompartments preserved their integrity inside GUVs (Figure 22D, Figure 23F). All experiments were performed at room temperature and studied over 48 h in presence and absence of DTT.

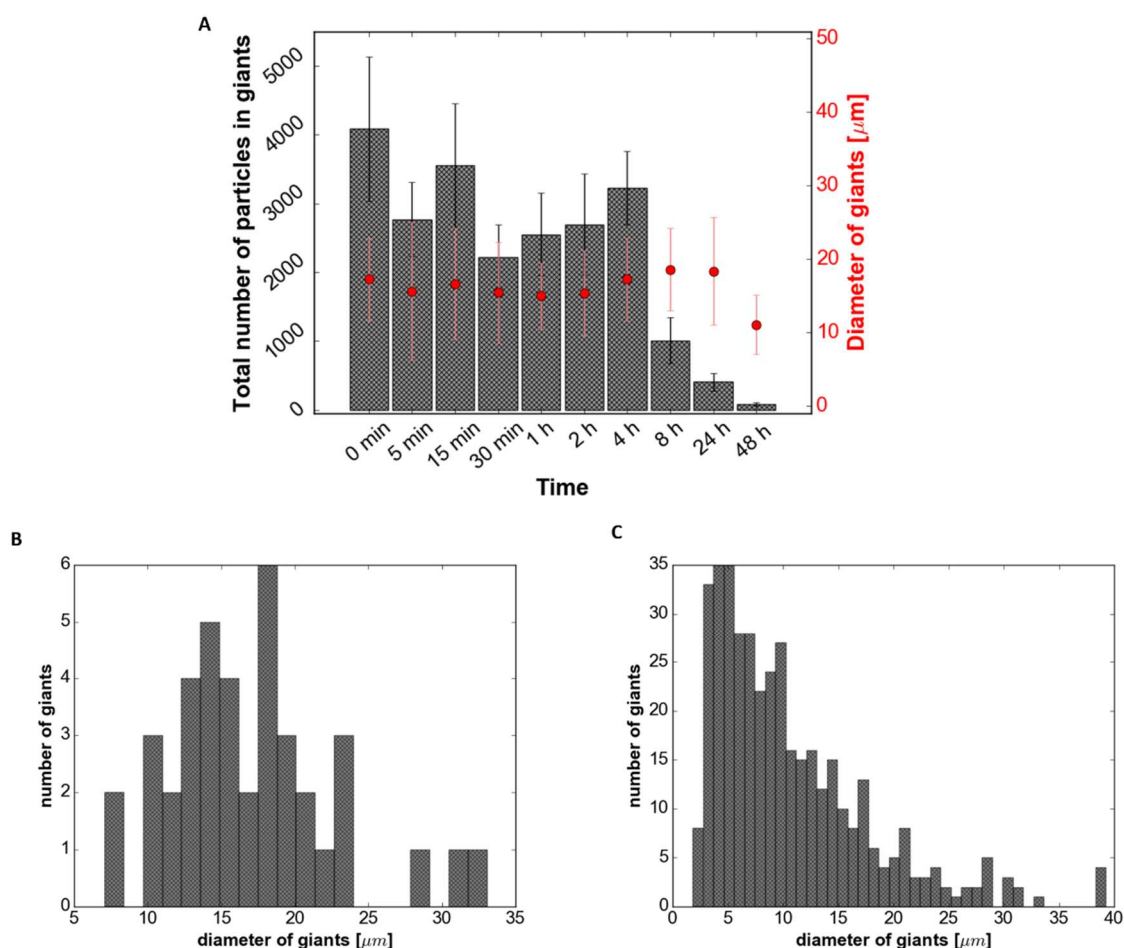


Figure 24. Estimation of the total number of particles in the GUVs in presence of DTT over time and the GUV size distribution. (A) The number of particles in giant vesicles (grey bars) was compared to the diameter of giant vesicles (red dots). Some standard deviations are too small to be distinguished from the symbol. (Values are mean \pm standard deviation). (B) Histogram of the size distribution of Bodipy630/650 loaded NP-Graft in GUVs before addition of DTT selected for FCS measurements (N=40 GUVs). (C) Histogram of the size distribution of Bodipy630/650 loaded NP-Graft in GUVs before addition of DTT (N=400 GUVs) representing polydispersity of GUVs formed by film rehydration.

According to the histogram the size distribution of the NP-Graft loaded GUVs used for FCS measurements before addition of DTT was between 7 and 33 μm ($N= 40$ GUVs, Figure 24B). In general, the simple and rapid formation of multicompartment vesicles via gentle film rehydration method provided a polydisperse mixture of sizes in the range between 2 to 40 μm ($N= 400$ NP-Graft-loaded GUVs, Figure 24C). Only GUVs with sizes above 4 μm , where the aqueous core can clearly be distinguished from the membrane, were chosen for FCS and CLSM analysis of the functionality of the assemblies. If a better control of the size distribution is needed, one can use a patterned surface for film rehydration ^[180] or transfer the system to a microfluidics-based formation method. ^[181, 182] As expected, GSH had no observable effect on encapsulated NP-Graft (Figure 23D, Figure 22C). No GUV swelling was observed after DTT addition, excluding a dilution effect (Figure 24A).

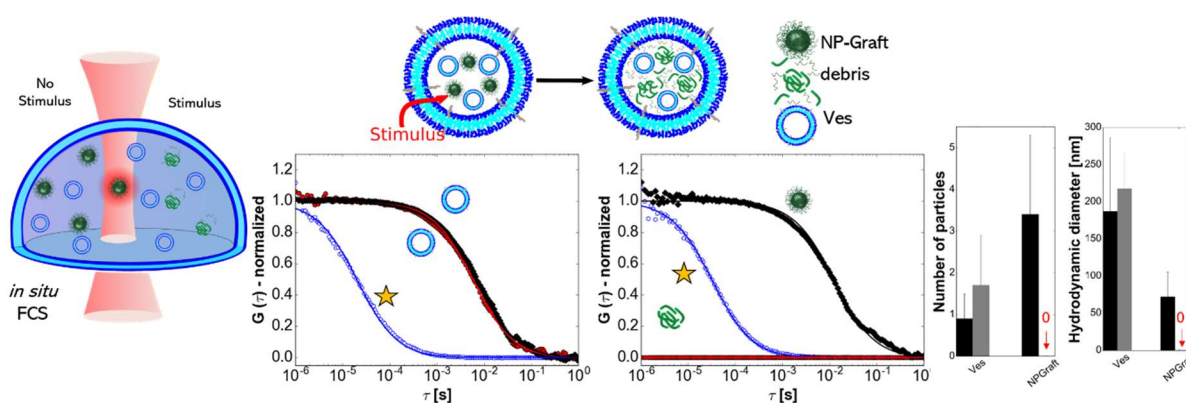


Figure 25. Characterization of the selective reduction sensitiveness of multicompartment vesicles loaded with two different subcompartments (reduction-sensitive nanoparticles (NP-Graft) and non-responsive polymer vesicles (Ves)). Schematic illustration of multicompartment vesicle before and after addition of stimulus (DTT). The diffusion times and number of particles (average in confocal volume) in the GUV show that in presence of DTT (grey) only the reduction sensitive NP-Graft disassembled, while the non-responsive subcompartments (Ves) stayed intact. In absence of DTT, both subcompartments were stable (black) ($N=3$ GUVs before and after DTT per channel). For the FCS measurements: normalized autocorrelation curves are shown with symbols, corresponding fits as solid lines, measurements of the free dye in blue (Bodipy630/650 or OG488), particles in GUV in absence of DTT (black) and after addition of DTT (red), incubation times 24 h.

As NP-Control nanoparticles were not stimuli-responsive, they were not affected by the presence of the reducing agent, and the multicompartment vesicles remained intact (Figure 23C, E, G and Figure 22E-G). Therefore, the disassembly of the encapsulated NP-

Graft nanoparticles proceeded via cleavage of disulfide bonds between PMOXA domains and PCL blocks upon addition of DTT as signaling molecule from the surrounding environment of the GUVs. When the subcompartments are non-responsive or the external stimulus is not present in the lumen, the multicompartments preserve their architecture and remain in a “silent mode” for several months (Figure 17).

Then we moved on to selectively release cargo from a subcompartment (NP-Graft) in the presence of a specific external stimulus *i.e.* the membrane-permeating DTT, while the other subcompartment (Ves5) should stay intact (Figure 25). In absence of the external stimulus, both the subcompartments remained intact inside the lumen of the GUV, confirmed by the FCS measurements. After a 24 h incubation time with DTT, the reduction sensitive NP-Graft disassembled via disulfide bond cleavage as seen by the disappearance of the correlation curve and hence a drop in the number of particles in the confocal volume inside the GUV from 3.0 ± 2.9 to background levels. The non-responsive subcompartments preserved their architecture (Figure 25) confirming that the selective disassembly of only one subcompartment was successful. This set the basis for using this hierarchical assembly to create simple polymeric protocells with two subcompartments that act as artificial organelles performing cascade reactions triggered via an external signal.

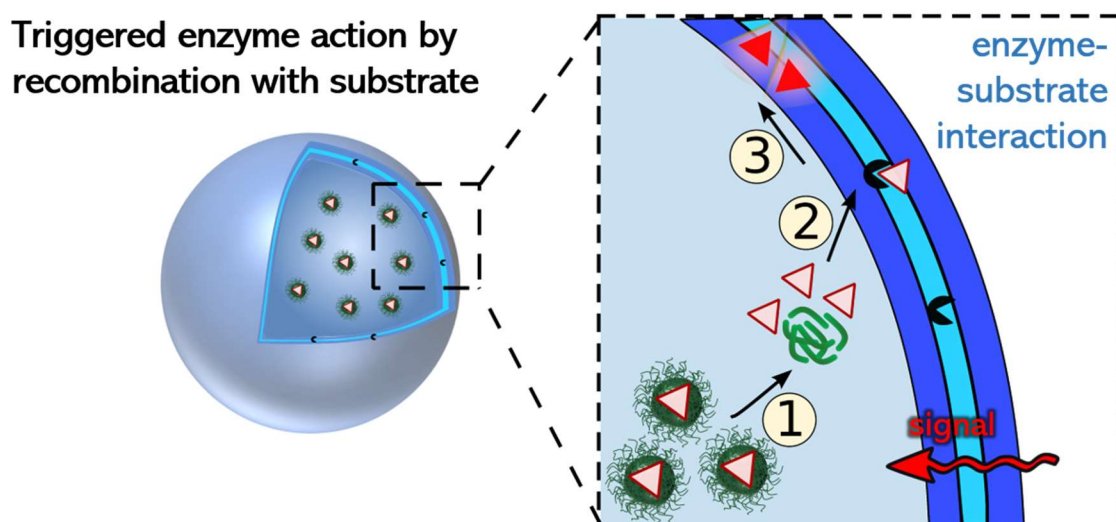
3.3. Conclusion

The results presented in this chapter clearly indicate that various types of multicompartments, via encapsulation of dye-loaded subcompartments in giant polymer vesicles, were successfully formed using a gentle self-assembly procedure (film rehydration). The membrane of the GUV (11 nm membrane thickness) was shown to be permeable for DTT, while molecules with higher molecular weight, such as GSH did not permeate through the membrane. We decorated the membrane with the model

receptor molecule heparin that interacted with a ligand model (protamine). To study the permeability of the membrane towards reducing agents, we loaded the GUVs with resazurin. The fluorescence intensity, associated with resorufin production, increased already 2 h after addition with DTT, while GSH showed no effect even after 72 h. This allowed to use DTT as an externally added stimulus to selectively induce the release of cargo from the reduction sensitive subcompartments NP-Graft. For detailed FCS measurements performed directly inside the GUV lumen, we could conclude that encapsulated NP-Graft nanoparticles successfully disassembled – proceeding via cleavage of disulfide bonds between PMOXA domains and PCL blocks – upon addition of DTT as signaling molecule from the surrounding environment of the GUVs. Our multicompartments were generated in high yields (95% of the giant polymersomes were loaded with polymeric subcompartments). For the two-type multicompartments, we successfully co-loaded the reduction sensitive nanoparticles with non-sensitive subcompartments within a single GUV. Thereby, we could selectively release the cargo from one type of subcompartments, while the other stayed intact as observed by *in situ* FCS. The multicompartment systems preserve their architecture for several months when no external stimulus is present, highlighting suitability to progress towards future applications as cell mimics, biosensors and *in vivo* diagnostics.

4. Enzymatic Activity via Triggerable Multicompartments

In this chapter, we introduce triggered release of an enzymatic substrate (DGGR) from an internal subcompartment upon arrival of an external stimulus (DTT) across the outside membrane of the multicompartments. This signal disassembled the subcompartments and the liberated substrate recombined with its enzyme (lipase) to form the fluorescent product methylresorufin. The enzymatic cascade reaction was studied in a one-type and a two-type responsive multicompartment system in isolated reaction steps.



PARTS OF THIS CHAPTER HAVE BEEN PUBLISHED AND REPRINTED HEREIN WITH PERMISSION FROM REFERENCE ^[1]. COPYRIGHT (2019) JOHN WILEY AND SONS:

SAGANA THAMBOO, ADRIAN NAJER, ANDREA BELLUATI, CLAUDIO VON PLANTA, DALIN WU, IOANA CRACIUN, WOLFGANG MEIER^x AND CORNELIA G. PALIVAN^x. MIMICKING CELLULAR SIGNALING PATHWAYS WITHIN SYNTHETIC MULTICOMPARTMENT VESICLES WITH TRIGGERED ENZYME ACTIVITY AND INDUCED ION CHANNEL RECRUITMENT, *ADVANCED FUNCTIONAL MATERIALS*, 2019, 1904267.

PARTS OF THIS CHAPTER ARE A MANUSCRIPT IN PREPARATION:

SAGANA THAMBOO*, ANDREA BELLUATI*, ADRIAN NAJER, VIVIANA MAFFEIS, CLAUDIO VON PLANTA, IOANA CRACIUN, CORNELIA G. PALIVAN^x, WOLFGANG MEIER^x, MULTICOMPARTMENT POLYMER VESICLES WITH ARTIFICIAL ORGANELLES FOR SIGNAL-TRIGGERED CASCADE REACTIONS INCLUDING CYTOSKELETON FORMATION, 2020, 2002949.

**These authors contributed equally*

4.1. Introduction

Subcellular compartmentalization of cells, a defining characteristic of eukaryotes, is fundamental for the fine tuning of internal processes and the responding to external stimuli.^[2] Cellular organelles can achieve highest efficiency, where optimal conditions can be created within each compartment, to allow the simultaneous regulation of various cascade reactions.^[11] Reproducing and controlling such compartmentalized hierarchical organization, responsiveness and communication is important for understanding biological systems and applying them to smart materials.^[183]

Herein, a cellular signal transduction strategy (triggered release from subcompartments) was leveraged to develop responsive, purely artificial, polymeric multicompartment assemblies. Incorporation of responsive nanoparticles^[170] – loaded with enzymatic substrate – as subcompartments inside micrometer-sized polymeric vesicles (polymersomes) allowed to conduct us bioinspired enzymatic signaling cascades. Signal triggered activity of an enzymatic reaction was demonstrated in multicompartments through recombination of compartmentalized substrate and enzyme. To mimic cellular functions, a substrate was segregated into separate inner compartment of the NP-Graft and entrapped the enzyme into the giant polymersome membrane due to its hydrophobicity. To demonstrate the proof of concept, we selected a common enzymatic reaction using a hydrophobic fluorogenic substrate (DGGR). The substrate was released from the reduction sensitive NP-Graft inside the GUV. The hydrophobic model enzyme lipase in the giant polymersome subsequently catalyzed the production of the fluorophore methyl-resorufin only when triggering NP-Graft disassembly and substrate release via an externally added signal (DTT).

4.2. Results and Discussion

4.2.1. Triggered Enzymatic Reactions in Multicompartments

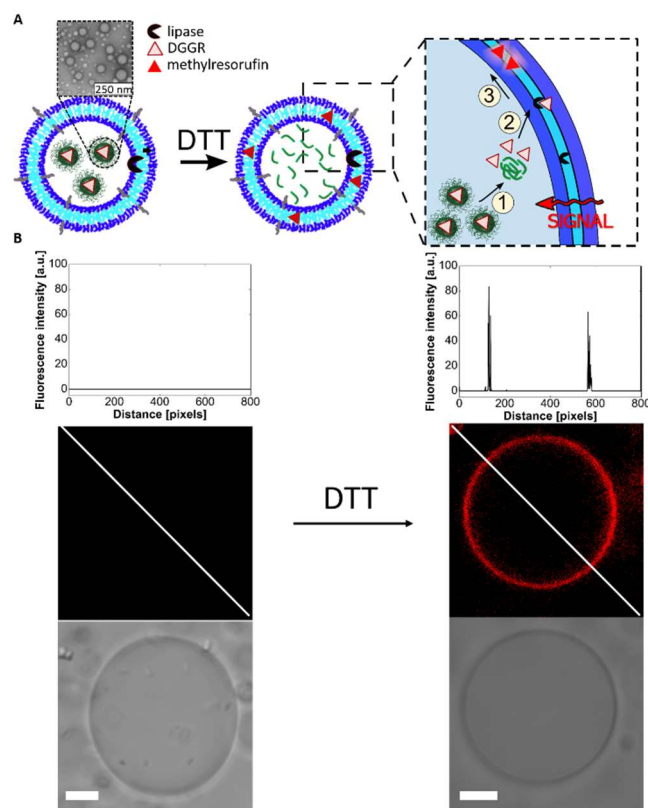


Figure 26. Compartmentalization of enzyme reaction. (A) Schematic representation of signaling pathway resulting in lipase activity. The DGGR loaded NP-Graft and lipase were co-encapsulated in the giant vesicles. The substrate was released in presence of DTT and was transformed by lipase to form the fluorescent product (methylresorufin) which preferentially associated with the giant vesicle membrane. (B) CLSM imaging of DGGR loaded NP-Graft and lipase loaded giant vesicles in absence (left) and presence of DTT (right). Histogram along diagonal of fluorescence image (top), fluorescence image (middle) and bright field image (bottom). Scale bars, 5 μm .

In order to increase the complexity of the stimuli-responsive multicompartments and trigger a desired reaction, we co-encapsulated enzymes and NP-Graft nanoparticles loaded with their corresponding substrates within GUVs. We then controlled the triggered subcompartment's destruction by applying an external signal to switch on the enzymatic reaction. The straightforward production and the mild conditions for the formation of GUVs make them compatible with biomolecules thus allowing us to encapsulate enzymes.

We used as a model enzyme, pancreatic lipase, which is hydrophobic, and therefore expected to be entrapped in the GUV's membrane. To achieve a controlled and responsive multicompartment, the fluorogenic lipase substrate 1,2-Di-O-lauryl-rac-glycero-3-(glutaric acid 6-methylresorufin ester) (DGGR) ^[184] was first incorporated in the NP-Graft to segregate it from the enzyme when they were co-loaded inside GUVs (Figure 26A). When the reducing agent is added to the exterior medium a three-step pathway is hypothesized to provide the functionality: 1) DTT penetrates inside GUVs, 2) it induces the disintegration of the NP-Graft and the release of DGGR, and 3) the substrate is free to participate in the enzymatic reaction.

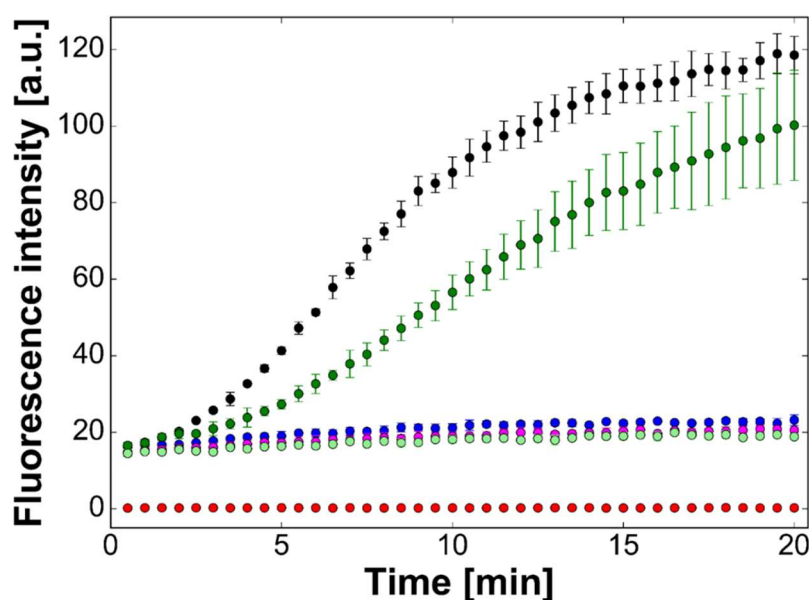


Figure 27. Enzymatic reactions in solutions (PBS and sucrose). In PBS: Lipase mixed with DGGR loaded NP-Graft and DTT (black), Lipase and DGGR loaded NP-Graft alone (red), DGGR loaded NP-Graft and DTT alone (pink); Lipase, DGGR loaded NP-Graft, DTT and lipase inhibitor Orlistat (blue). In sucrose: Lipase mixed with DGGR loaded NP-Graft and DTT (dark green); DGGR loaded NP-Graft and DTT alone (light green). Error bars are given as mean \pm standard deviation ($n = 3$), and in some cases, bars are smaller than the corresponding dot. Ex/Em 529/600 nm.

In solution, when lipase, DGGR loaded NP-Graft and DTT were mixed, a significant increase of fluorescence associated with product formation was observed (Figure 27). This indicates that the substrate entrapped inside NP-Graft was released in the presence of DTT to finally form the fluorescent product by the subsequent lipase activity. When only DGGR loaded NP-Graft and lipase were mixed in solution, no fluorescence signal was detected indicating that the enzyme and its substrate are

completely separated. As a control, DGGR loaded NP-Graft and DTT mixture in absence of lipase, led to a minimal increase of fluorescence in PBS and 300 mM sucrose. In presence of the lipase inhibitor Orlistat, lipase was completely inhibited and yielded no product.

Next, we encapsulated DGGR loaded NP-Graft nanoparticles and lipase within GUVs to obtain multicompartments. The absence of fluorescence after assembly of the multicompartments indicated successful compartmentalization of the substrate with no contact with the enzyme (Figure 26B, Figure 28B). Upon addition of DTT to the GUVs' environment, the increase in the fluorescent signal associated with the product (methylresorufin) confirms the enzyme activity triggered by the release of the substrate from the sacrificial nanoparticles, as observed by CLSM (Figure 26B, Figure 28A).

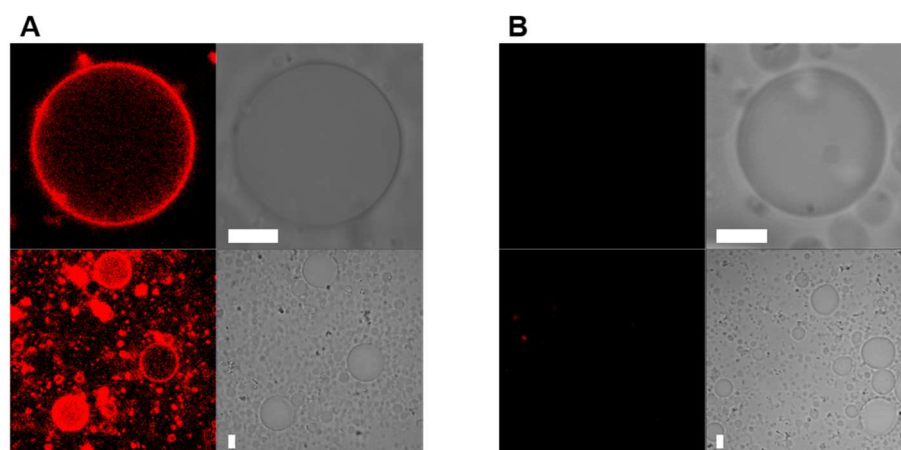


Figure 28. Compartmentalization of enzyme reaction. Fluorescence image (left) and bright field image (right) of the DGGR loaded NP-Graft and lipase loaded giant vesicles (**A**) in presence of DTT after 24 h of incubation. (**B**) In absence of DTT after 24 h of incubation. Orlistat (lipase inhibitor) was added to the external solution to inactivate free lipase. Scale bars, 5 μm .

In 83% of GUVs, methylresorufin tended to partition into the membrane (red ring) (Figure 29). As lipases are known to typically work at the interphase between hydrophobic and hydrophilic environments, methylresorufin was produced close to the outer membrane. In 12% of the vesicles, the membrane and the lumen showed fluorescence (red vesicle), indicating that a fraction of the substrate was activated by lipase and tended to stick to the NP-Graft debris. The remaining 5% of multicompartments showed no fluorescence. Note that any free, non-encapsulated

lipase in the surroundings of the GUVs was inhibited by adding Orlistat to the solution to avoid bias of reactions outside the vesicles. Therefore, no further purification was necessary. Outer membrane of GUVs with incorporated DGGR loaded NP-Graft and lipase remained stable in presence of DTT after 24 h incubation with a size distribution between 6 and 22 μm for measured GUVs ($N=40$ GUVs, Figure 29E).

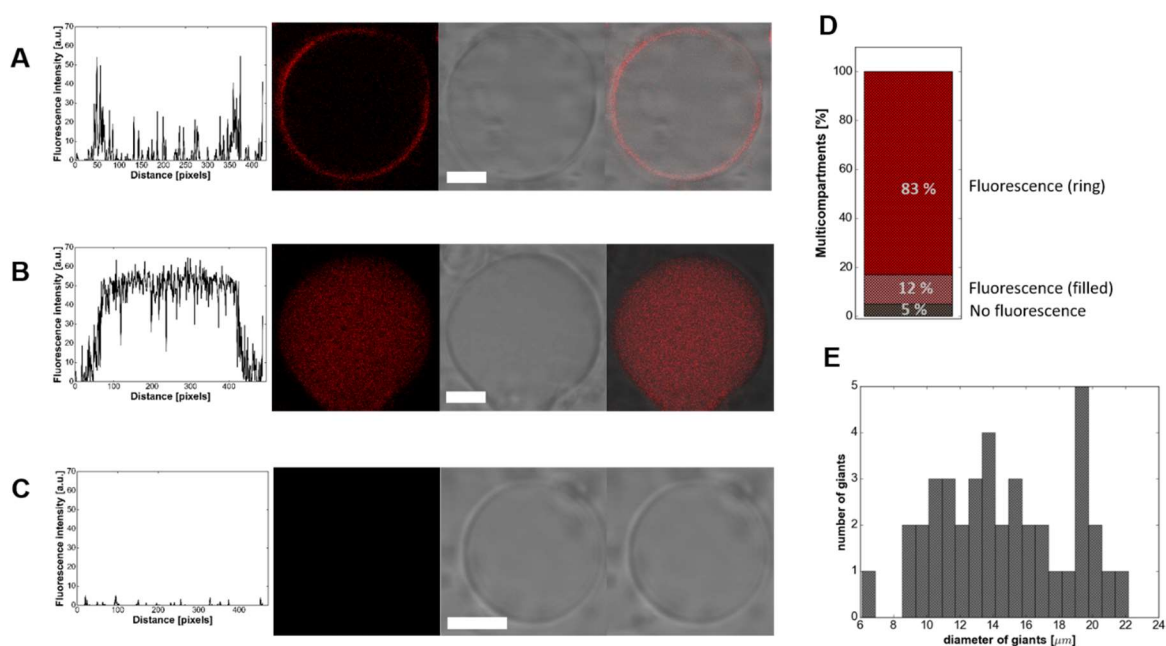


Figure 29. Efficiency of the compartmentalization of enzyme reaction in presence of 10 mM DTT after 24 h incubation time and corresponding GUV size distribution. (A-C) Plot profile of the fluorescence intensity along the diagonal of the image (left), CLSM image of lipase and DGGR loaded NP-Graft in giant vesicles (middle) and corresponding bright field image (right), indicating: (A) production of methylresorufin adsorbed to the polymer membrane (83%), (B) production of methylresorufin in the cavity of the giant vesicle (12%) and (C) remaining empty (5%, no fluorescence). (D) Histogram of efficiency of DGGR loaded NP-Graft in giant vesicles. (E) Histogram of size distribution of measured DGGR loaded NP-Graft and lipase in GUVs in presence of DTT after 24 h incubation ($N=40$ GUVs). Scale bars, 5 μm .

An enzymatic reaction inside multicompartments was successfully triggered via a cascade involving DTT that induced a change in the internal architecture and release of the DGGR substrate to encounter the encapsulated lipase. Here we used an enzyme that exhibits its highest catalytic activity at the interface between the hydrophobic membrane of the GUV and hydrophilic content; in general, this type of multicompartment could be used as a tool to study reaction kinetics of hydrophobic enzymes that otherwise would be difficult to study in solution.

4.2.2. Compartmentalized Enzymatic Reactions using Two Internal Subcompartments

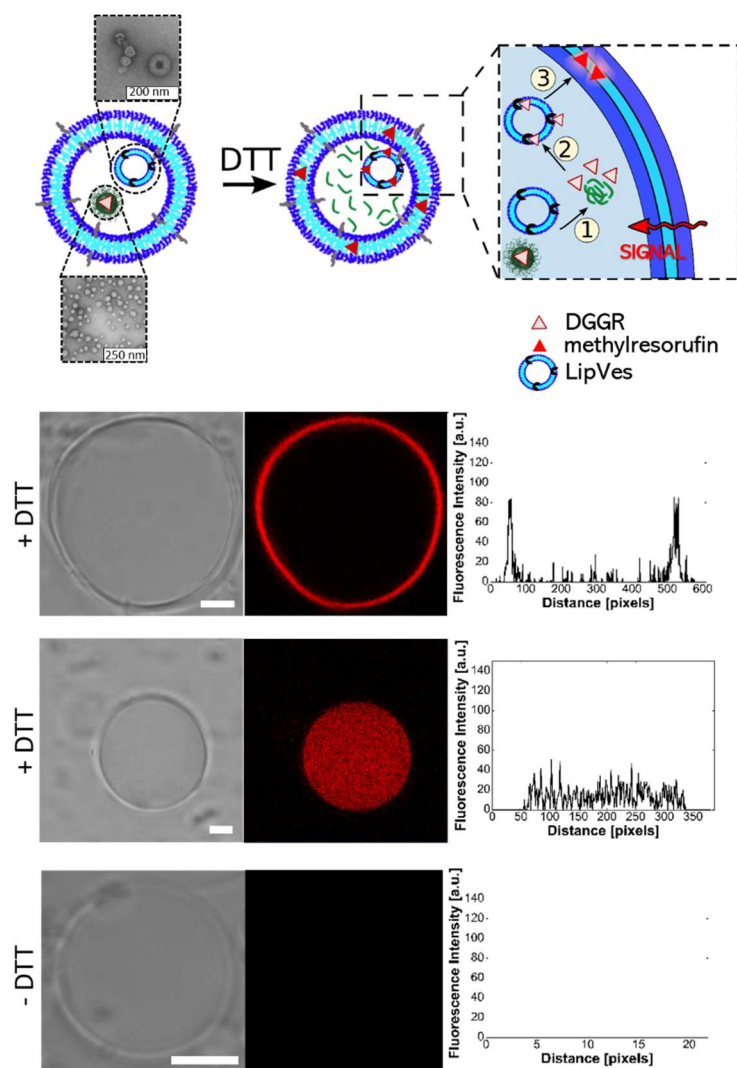


Figure 30. Triggered enzyme activity and ion channel recruitment using two different internal subcompartments within GUVs. Schematic representation of enzymatic reaction (top) using substrate (DGGR) loaded NP-Graft and enzyme (lipase) adsorbed polymersomes (LipVes) co-loaded into GUVs with corresponding TEM images of subcompartments. Substrate was released from NP-Graft in presence of DTT and transformed into the fluorescent product (methylresorufin). CLSM imaging of DGGR loaded NP-Graft and LipVes in GUVs in absence (left) and presence (right) of DTT. Histogram along diagonal of fluorescence image (top), fluorescence image (middle) and bright field image (bottom). Scale bars, 5 μm .

The responsive multicompartments were further upgraded by spatially segregating lipase from its substrate in two distinct subcompartments, for the two-type system. Upon arrival of a signal from the external medium, the enzymatic reaction should be triggered by recombining substrate – release from stimuli-responsive substrate-containing subcompartment – with enzymes of secondary subcompartment (artificial

organelles). The lipase substrate DGGR was incorporate in the NP-Graft as described for the two-type multicompartment (Figure 30, Figure 31, Figure 32).

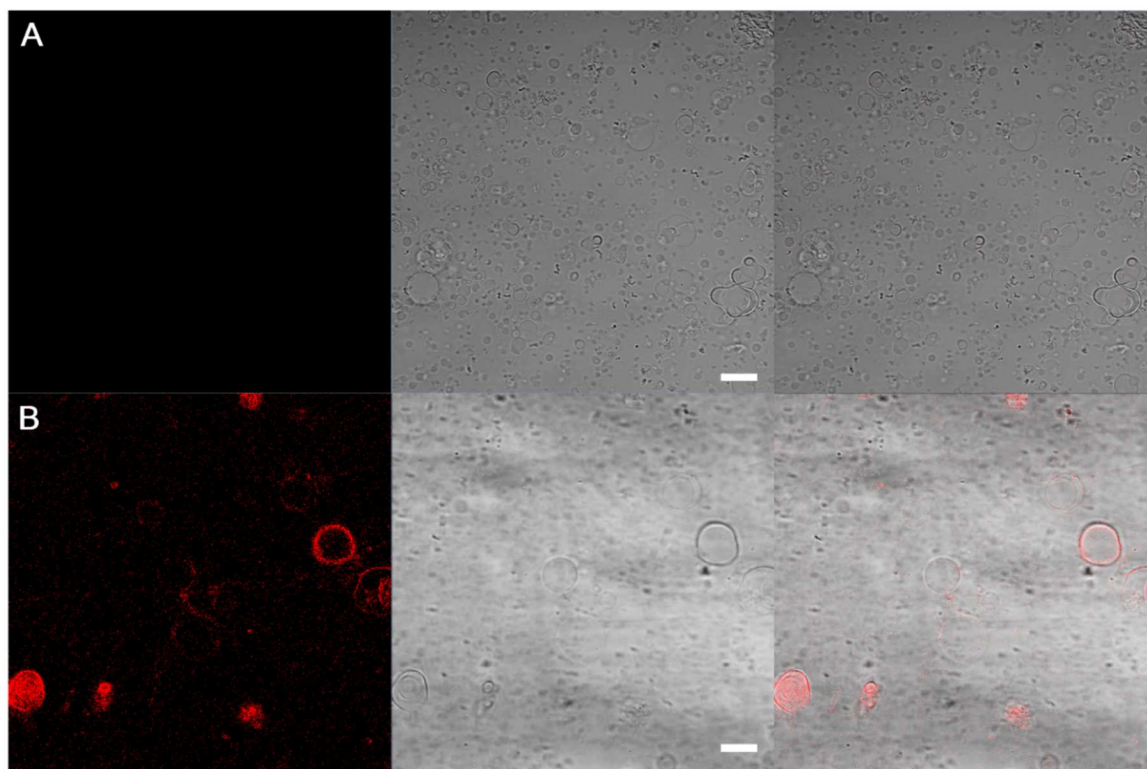


Figure 31. Compartmentalization of enzyme reaction via two different internal subcompartments. Fluorescence image (left), bright field image (middle) and merge (right) of the DGGR loaded NP-Graft and lipase adsorbed polymersomes (LipVes) co-loaded giant vesicles (**A**) in absence and (**B**) in presence of DTT after 24 h of incubation. Orlistat (lipase inhibitor) was added to the external solution to inactivate unloaded LipVes. Scale bars, 5 μm .

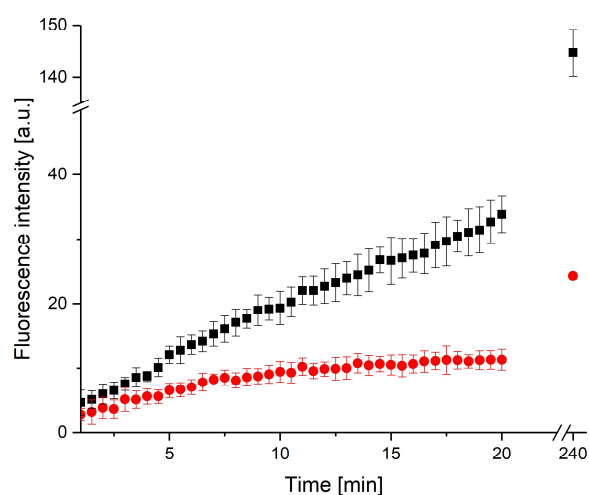


Figure 32. Enzymatic reactions in 300 mM sucrose. Lipase adsorbed on vesicle (LipVes) and DGGR loaded NP-Graft in solution in presence (black) and in absence (red) of DTT. Error bars are given as mean \pm SD ($n = 3$). Ex/Em 529/600 nm.

For the secondary artificial organelle, we adsorbed the enzyme lipase on nanoscale polymersomes (LipVes). We first formed the nanoscale polymersomes and then added lipase that adsorbed to the hydrophobic membrane, followed by purification via size exclusion. For the secondary artificial organelle, we adsorbed the enzyme lipase on nanoscale polymersomes (LipVes), with an adsorption efficiency of 73%. Both artificial subcompartments were co-loaded into our polymer GUVs during the rehydration procedure. No fluorescence was observed in a non-reductive environment thanks to spatial segregation of substrate and enzyme in the two subcompartments. Upon addition of the signaling molecule DTT to the GUVs, enzymatic substrate (DGGR) was released from the signal-responsive artificial organelle (NP-Graft) to interact with the enzyme on the secondary artificial organelle (LipVes) and form the fluorescent product (methylresorufin). The triggered enzyme activity was achieved in 90% of GUVs (size distribution between 4 and 29 μm , N= 40 GUVs) where methylresorufin either partitioned on the GUVs membrane or stuck on the remaining subcompartments in the lumen, while 10 % of the GUVs showed no fluorescence (Figure 33). Any non-encapsulated LipVes were inactivated by using Orlistat, a lipase inhibitor in the outside solution. In conclusion, the lipase reaction inside the two-type multicompartments was successfully triggered by an external signal that induced a change in the internal architecture to initiate the formation of the fluorescent product.

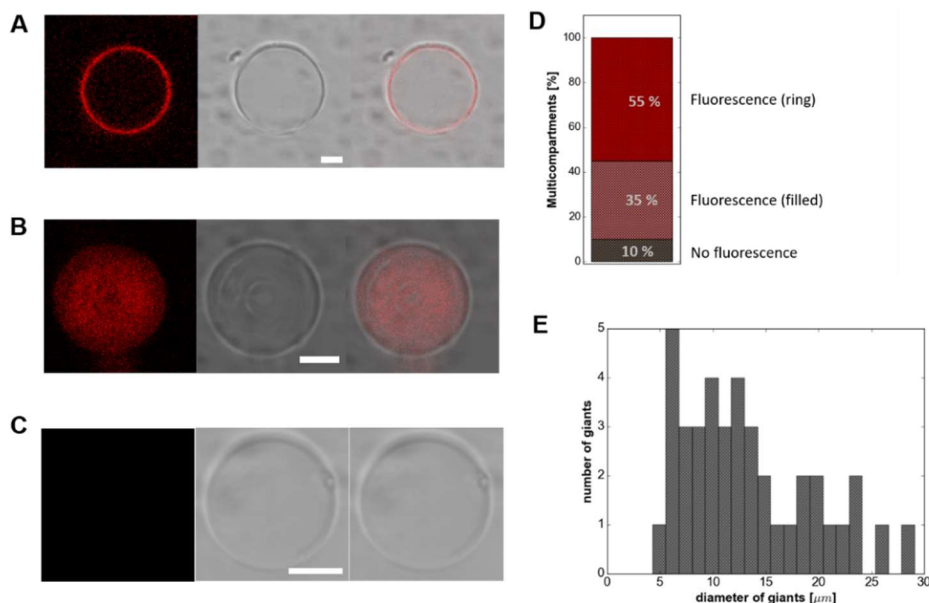


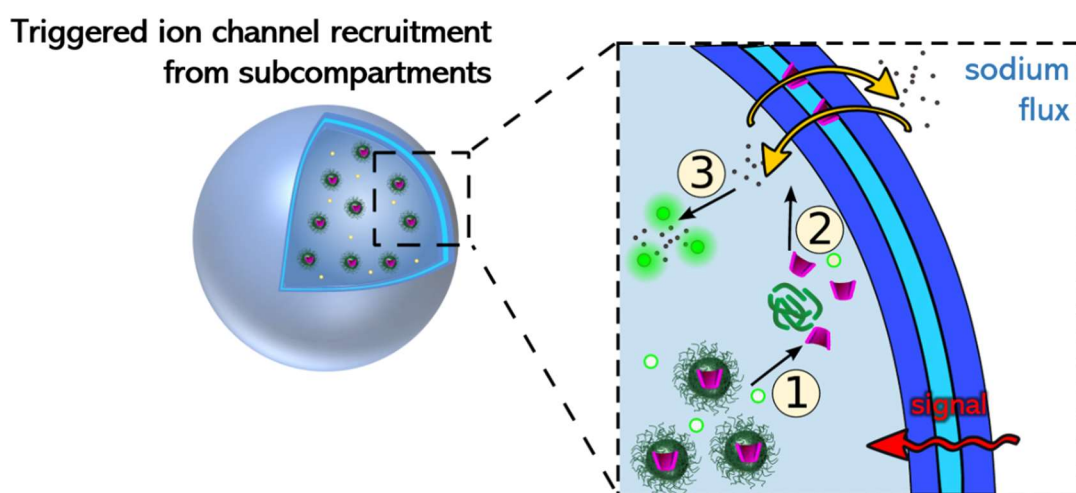
Figure 33. Efficiency of the compartmentalization of enzyme reaction in presence of 10 mM DTT after 24 h incubation time and corresponding GUV size distribution. (**A-C**) CLSM image of lipase adsorbed polymersomes (LipVes) and DGGR loaded NP-Graft co-loaded in giant vesicles (left), corresponding bright field image (middle) and merge (right), indicating: (**A**) production of methylresorufin adsorbed to the polymer membrane (55%), (**B**) production of methylresorufin

4.3. Conclusion

The experimental results in this chapter clearly reveal that a stimulus triggered enzymatic reaction can be performed within polymeric GUVs formed by film rehydration technique. We can conclude, that an enzymatic reaction inside multicompartments was successfully triggered via a cascade involving an external signal that induced a change in the internal architecture (sacrificial subcompartments) and accompanied release of the substrate allowing it to encounter the encapsulated enzymes. The reaction only took place when the stimuli (DTT) was present, otherwise the spatial segregation of substrate away from enzyme remained intact. Due to the fluorescent property of the product, CLSM imaging revealed that the triggered enzymatic reaction was achieved in 95% for one-type multicompartments and in 90% of two-type multicompartments. In future studies, the combination of hydrophobic and hydrophilic enzymes can be used within the multicompartmental system to analyze more complex sequential biological reactions.

5. Ion Channel Recruitment in Triggerable Multicompartments

Here, a signal transduction cascade including the combination of a primary signal (presence of stimulus in the environment of multicompartments) with a secondary one (induced ion flow to/from the environment) is represented as a straightforward model of ion channel recruitment from internal subcompartments to the membrane upon signaling. This is a process naturally occurring in neuronal cells that can recruit ion channels from endosomes to the cell membrane when needed.



PARTS OF THIS CHAPTER HAVE BEEN PUBLISHED AND REPRINTED HEREIN WITH PERMISSION FROM REFERENCE ^[1]. COPYRIGHT (2019) JOHN WILEY AND SONS:

SAGANA THAMBOO, ADRIAN NAJER, ANDREA BELLUATI, CLAUDIO VON PLANTA, DALIN WU, IOANA CRACIUN, WOLFGANG MEIER^x AND CORNELIA G. PALIVAN^x. MIMICKING CELLULAR SIGNALING PATHWAYS WITHIN SYNTHETIC MULTICOMPARTMENT VESICLES WITH TRIGGERED ENZYME ACTIVITY AND INDUCED ION CHANNEL RECRUITMENT, *ADVANCED FUNCTIONAL MATERIALS*, 2019, 1904267.

PARTS OF THIS CHAPTER ARE A MANUSCRIPT IN PREPARATION:

SAGANA THAMBOO*, ANDREA BELLUATI*, ADRIAN NAJER, VIVIANA MAFFEIS, CLAUDIO VON PLANTA, IOANA CRACIUN, CORNELIA G. PALIVAN^x, WOLFGANG MEIER^x, MULTICOMPARTMENT POLYMER VESICLES WITH ARTIFICIAL ORGANELLES FOR SIGNAL-TRIGGERED CASCADE REACTIONS INCLUDING CYTOSKELETON FORMATION, *ADVANCED FUNCTIONAL MATERIALS*, 2020, 2002949.

**These authors contributed equally*

5.1. Introduction

Triggered recruitment of cellular receptors, transporters and ion channels from internal compartments (early endosomes or recycling endosomes) to the cell membrane and *vice versa* is important to control and fine-tune cellular signaling, as has been described for neurons^[185, 186] and cardiac muscle cells.^[187, 188] Successful functional insertion of ion channels (biopores) and membrane proteins into artificial polymer membrane allows induction of membrane permeability owing to the channel's intrinsic functionality.^[189] In here, a two-step signaling cascade was achieved by triggering the recruitment of ion channels from inner subcompartments to the giant vesicle membrane, inducing ion permeability, mimicking endosome-mediated insertion of internally stored channels. A triggered insertion of the ion channel from the inside introduced permeability of the outer membrane to ions, which mimics a natural process of signal-triggered ion channel recruitment from inner compartments. This inside-out incorporation of ion permeability to the outer membrane can be utilized in both ways, to release a secondary messenger to the environment (outflux of encapsulated ions) or let a secondary signal in (influx of ions). Our setup allows a precise temporal control over spatially confined components, demonstrating that responsive multicompartiment systems open up vast design options for various applications in fields such as catalysis and biomedicine.

5.2. Results and Discussion

5.2.1. Triggered Ion Efflux via Compartmentalized Giant Polymersome

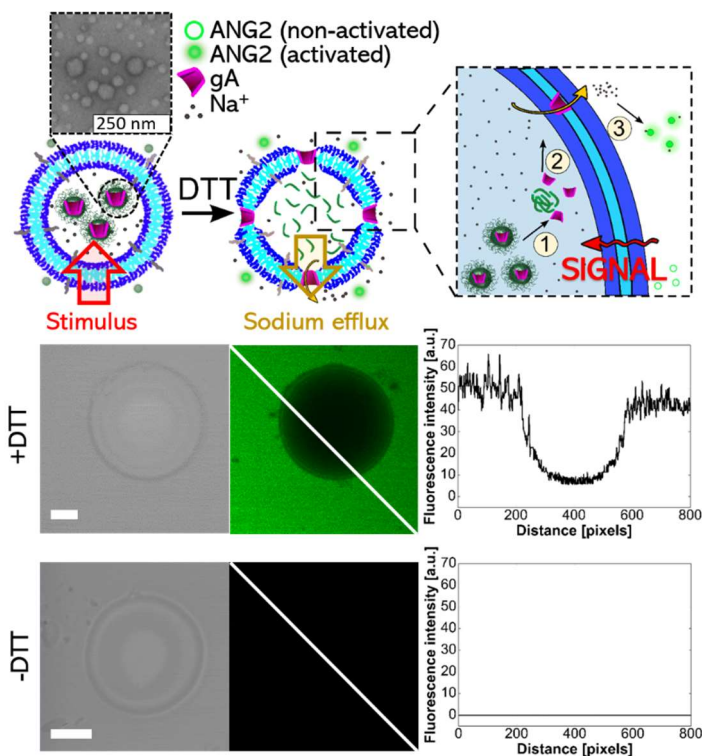


Figure 34. Schematic representation (top) of gA mediated efflux of sodium ions from the GUV cavity. DTT induced gA permeabilization of the GUV membrane, allows sodium ions in the interior to exit the vesicle and activate the ANG2 in the surrounding environment of the multicompartments. Bright field image (left), fluorescence image (middle) and histogram along the diagonal of fluorescence image (right) in presence (middle) and absence (bottom) of DTT. Scale bars, 5 μm .

Moving a step further in the development of our stimuli-responsive multicompartments system, we aimed to induce selective membrane permeabilization, for signaling purposes, by recruiting ion channels from internal subcompartments to the GUV membrane. Dynamic ion channel recruitment to the cell membrane, to modulate permeability, was for example demonstrated in neurons. Endosomal compartments are involved in these processes of reducing or increasing the number of these specific membrane proteins by endocytosis and exocytosis, respectively. ^[185] As a suitable model, we chose to study the induced passage of monovalent cations through the GUV membrane when mediated by a recruited biopore, the peptide ion channel gramicidin A

(gA).^[94] The gA ion channel is pre-entrapped in NP-Graft, the primary signal (DTT) comes from the environment, while the secondary signals (sodium ions) are subsequently released from the inner cavity of the GUVs to induce a change in the external medium (Figure 34, Figure 35, Figure 36). In this respect, we entrapped gA loaded NP-Graft together with sodium ions (PBS) in the GUV lumen, while Asante Natrium Green2 (ANG2) dye was added to the multicompartments' environment, in a sodium-free buffer. When DTT was added from the outside, it induced the gA recruitment from the subcompartments and incorporation into the GUV membrane. This resulted in the diffusion of encapsulated sodium ions from the interior of the multicompartments to their exterior where the sodium sensitive dye ANG2 was activated. As expected, the sequence did not occur in the absence of DTT. The triggered recruitment and functional insertion of gA into the membrane of the multicompartments via responsive sacrificial subcompartments showed that we were able to successfully introduce a sequential signaling pathway into our multicompartments. The induced reconstitution of gA allowed the passage of the stored sodium ions “on demand” from the GUV lumen to the surrounding solution, where the sodium sensitive dye ANG2 was activated.

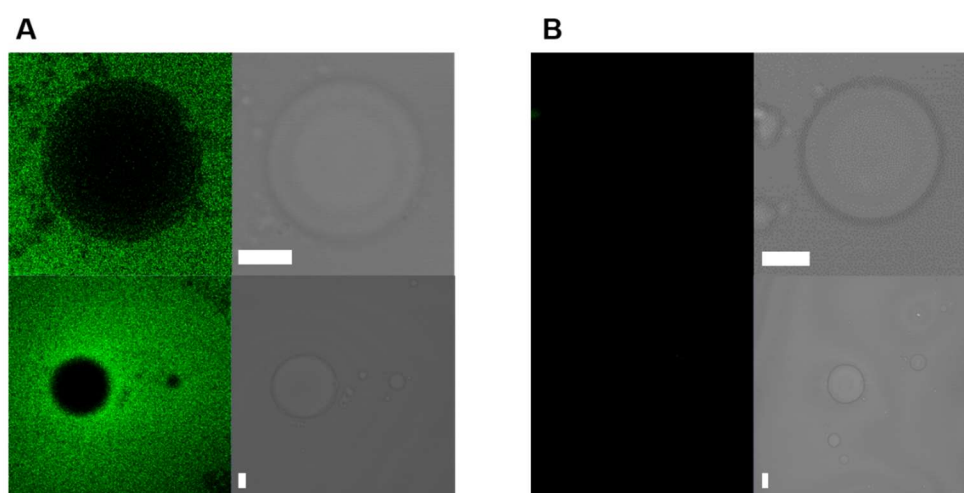


Figure 35. gA-mediated export of sodium ions from the vesicle cavity for sodium ion export. **(A)** Sodium sensitive dye ANG2 activated in presence of DTT for 24 h. **(B)** In absence of DTT after incubation of 24 h. Scale bars, 5 μm .

5.2.2. Triggered Gramicidin Reconstitution for Ion Influx

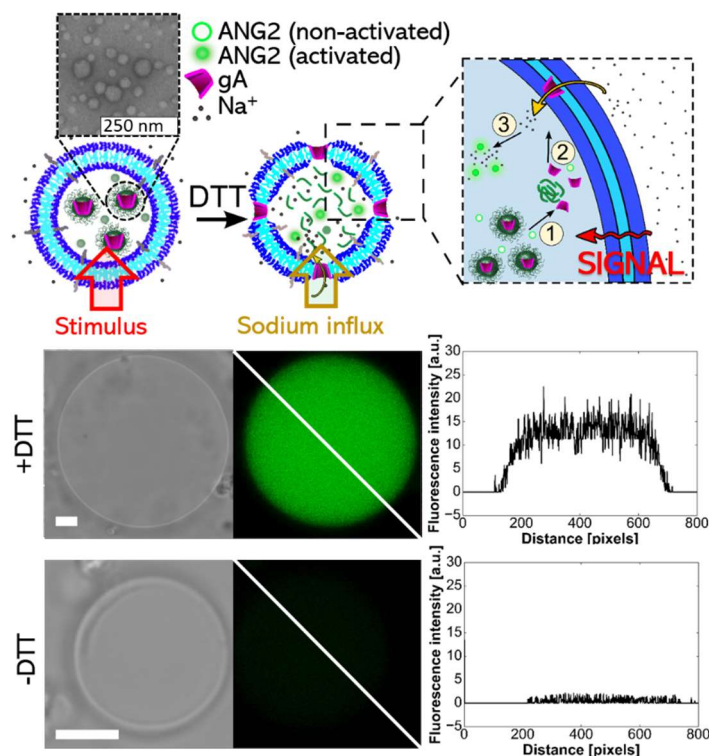


Figure 36. Triggered gramicidin ion channel recruitment from internal subcompartments to the polymer membrane of a multicompartiment using CLSM imaging. Schematic representation (top) of gA mediated import of sodium ions. Upon the addition of DTT, encapsulated gA is released from its NP-Graft and inserts into the GUV membrane boundary. This allows sodium ions from the outside to enter the GUV cavity where they activate the sodium sensitive dye ANG2. Bright field image (left), fluorescence image (middle) and histogram along the diagonal of fluorescence image (right) in presence (middle) and absence (bottom) of DTT.

We then changed the arrangement by inverting the location of the signals in relation to the architecture of the multicompartments, where the signaling pathway from the surrounding environment of multicompartments is based on a primary signal (DTT), inducing a secondary signal (sodium ion flow through the GUV membrane). To achieve this sequence of controlled signals, we first encapsulated gA loaded NP-Graft as subcompartments within GUVs in combination with a sodium sensitive dye ANG2 (Figure 36, Figure 37).

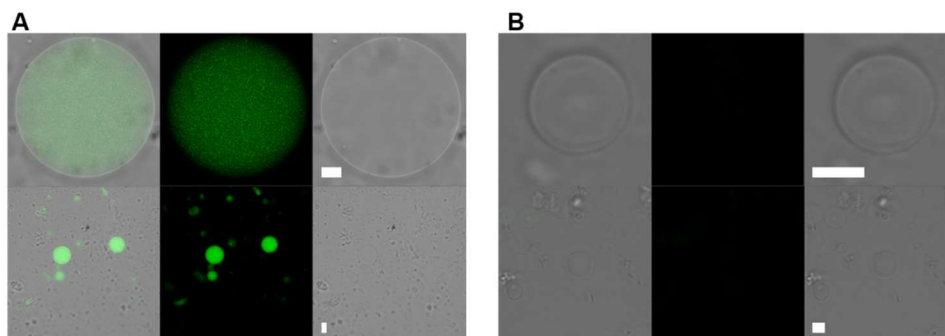


Figure 37. Triggered gramicidin pore assembly in the polymer membrane of a multicompartiment to import sodium ions. **(A)** Sodium sensitive dye ANG2 activated in presence of DTT after 24 h. **(B)** In absence of DTT after incubation of 24 h. Scale bars, 5 μm .

Upon addition of DTT as the first signal, NP-Graft nanoparticles disintegrated and released gA that inserted into the GUV membrane due to its hydrophobicity. gA insertion into GUVs' membrane allowed an influx of Na^+ ions from the environment into the GUVs cavity followed by activation of the Na^+ sensitive dye.

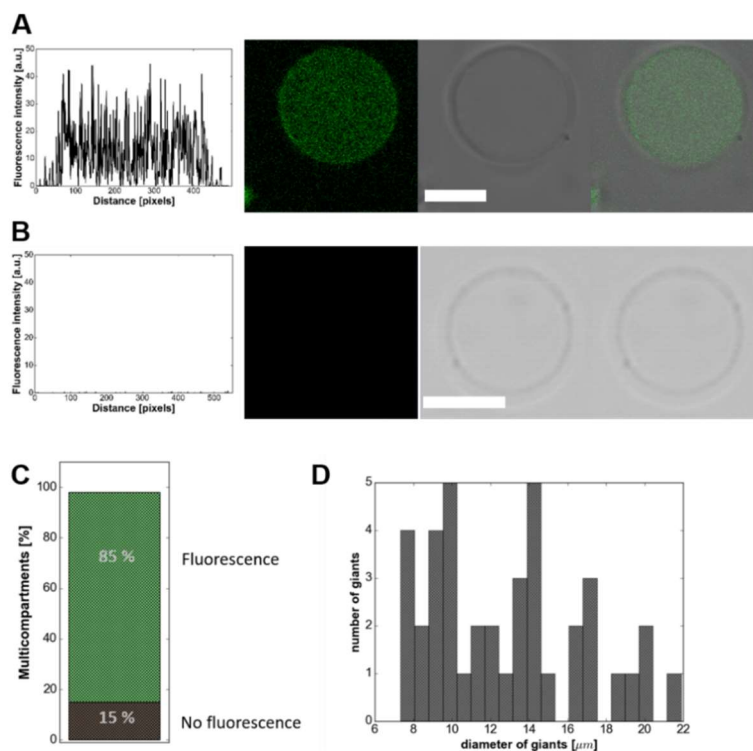


Figure 38. Efficiency of the compartmentalized gA reconstitution into the polymer membrane to import sodium ions in presence of 10 mM DTT after 24 h incubation time and corresponding size distribution. **(A-B)** Plot profile of the fluorescence intensity along the diagonal of the image (left), CLSM image of gA loaded NP-Graft in giant vesicles (middle) and corresponding bright field image (right), indicating: **(A)** activation of ANG2 by sodium ions (85%, fluorescence) and **(B)** remain empty (15%, no fluorescence). **(C)** Histogram of efficiency of gA loaded NP-Graft and ANG2 in giant vesicles in presence of DTT. **(D)** Histogram of size distribution of measured gA loaded NP-Graft and ANG2 in GUVs in presence of DTT after 24 h incubation (N=40 GUVs). Scale bars, 5 μm .

Overall, 85% of multicompartments were functional and induced the recruitment of biopores into the polymer membranes, as indicated by dye activation (Figure 38). In around 15% of multicompartments, no fluorescence was detected, most probably due to an insufficient loading of gA inside NP-Graft, ANG2 or NP-Graft inside GUVs or a combination thereof. According to CLSM images, gA loaded NP-Graft and ANG2 in GUVs used for FCS measurements in presence of DTT after 24 h incubation preserved the outer membrane (GUV) with a size distribution between 7 and 22 μm ($N = 40$ GUVs, Figure 38D).

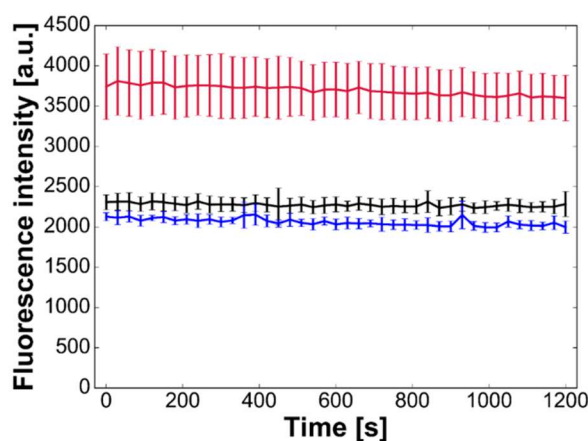
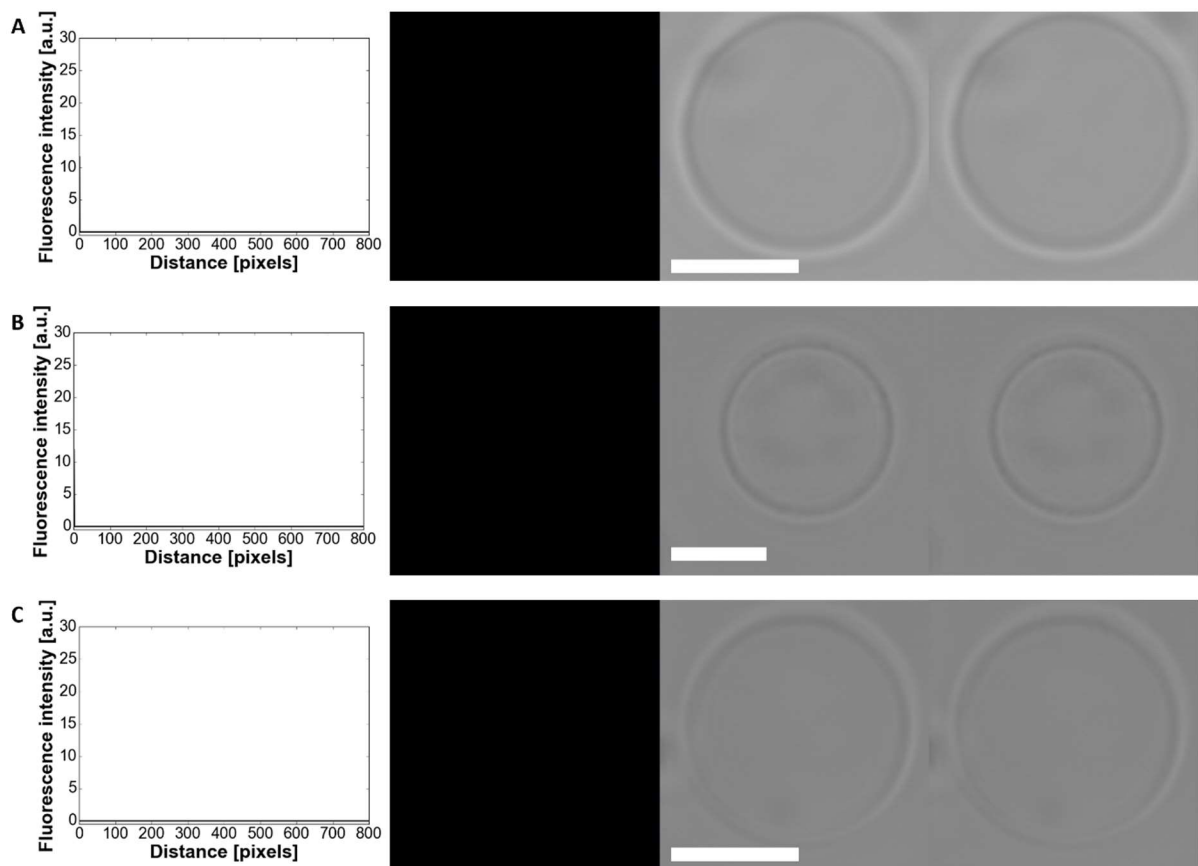


Figure 39. Fluorescence intensity of ANG2 dye in solution. ANG2 in 300 mM sucrose (black), in presence of 10 mM DTT (blue) and in presence of sodium ions (PBS, red). Ex/Em 525/545 nm.

In the absence of the reducing agent DTT, the ion channels remained entrapped inside subcompartments and the multicompartments remained impermeable to Na^+ ions: no increase in fluorescence was detected since there was no activation of ANG2. The dye ANG2 is activated only in presence of sodium ions (PBS) (Figure 39), while in sucrose solution or in HEPES buffer with 10 mM DTT, it remains non-fluorescent. As a control, when NP-Graft nanoparticles without cargo (EmptyNP) were used, the ANG2 dye was not activated inside the GUVs in presence and absence of reducing agent (Figure 40) due to their impermeability towards sodium ions without ion channel insertion. Accordingly, the use of sacrificial subcompartments loaded with desired molecules inside multicompartments represent an elegant manner to provide conditions for sequential signaling pathways.



5.2.3. Ion Channel Recruitment using Two Internal Subcompartments

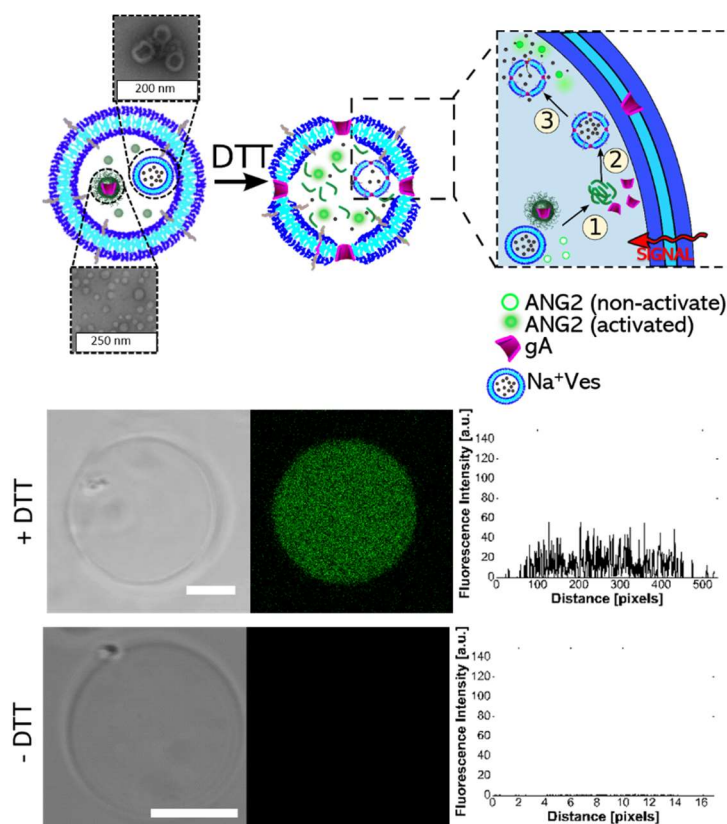


Figure 41. Schematic representation (top) of gA mediated release of sodium ions from subcompartments. Upon the addition of DTT, encapsulated gA is released from its NP-Graft and inserts into the membrane boundary of the polymersomes. This allows sodium ions exit the nanosized vesicle cavity where they activate the sodium sensitive dye ANG2 in lumen of the GUV. CLSM imaging of gA loaded NP-Graft, sodium encapsulated polymersomes (Na^+Ves) and ANG2 co-loaded in GUVs in absence (left) and presence (right) of DTT. Histogram along diagonal of fluorescence image (top), fluorescence image (middle) and bright field image (bottom). The samples were incubated for 24 h. Scale bars, 5 μm .

We further developed another two-type multicompartments that, upon the reducing stimulus, transfers ion channels from one type of artificial organelles (NP-Graft) to secondary membranous artificial organelles (Na^+Ves), hence permeabilizing those to allow the passage of monovalent cations. For the on-demand release of sodium ions from the secondary subcompartment (Na^+Ves), we co-loaded them in GUVs together with primary subcompartment (NP-Grafts) containing ion channel gA. The triggered recruitment of gA from the NP-Graft to the Na^+Ves , following the release of gA from the NP-Graft, was again achieved via the externally added signaling molecule DTT (Figure 41, Figure 42).

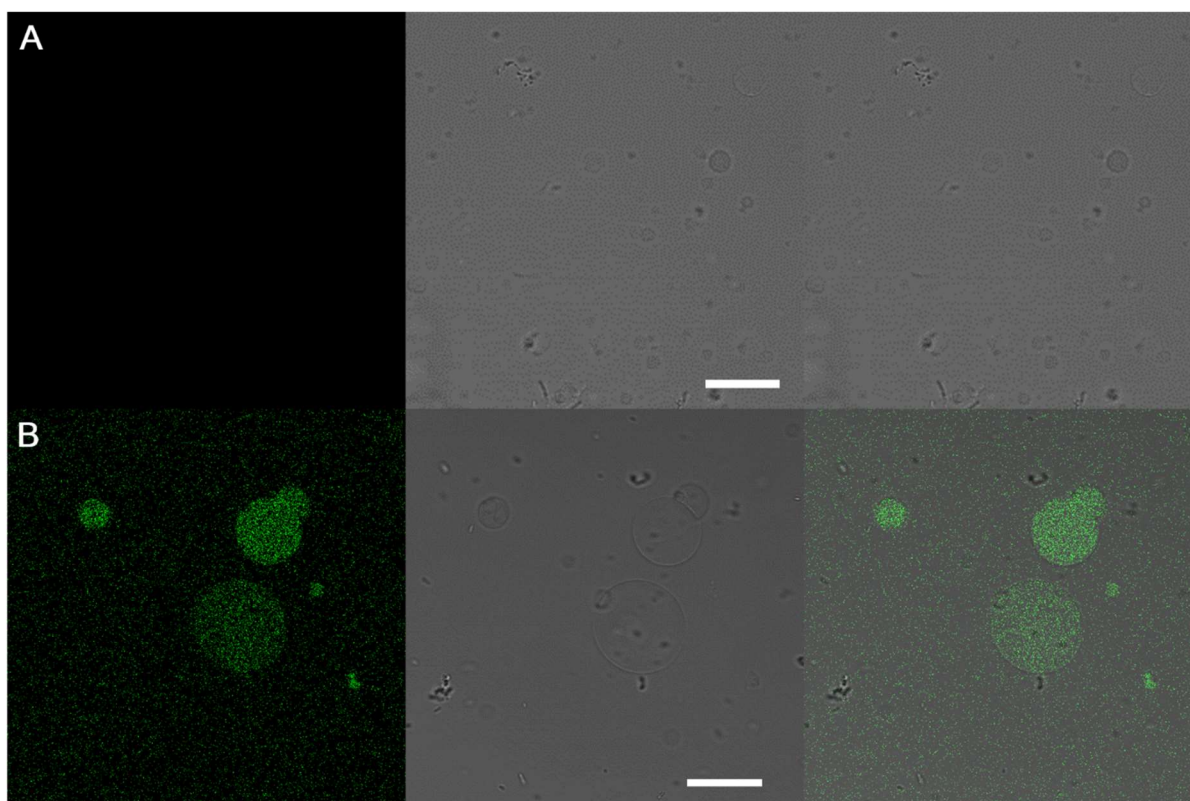


Figure 42. Triggered gramicidin pore recruitment in the polymer membrane of a multicompartment to import sodium ions. Fluorescence image (left), bright field image (middle) and merge (right) of the gA loaded NP-Graft, sodium loaded polymersomes (Na^+Ves) and ANG2 co-loaded giant vesicles (**A**) in absence of DTT and (**B**) in presence of DTT after 24 h of incubation. Scale bars, 5 μm .

With gA incorporated into the hydrophobic part of the membrane of the Na^+Ves , the sodium ions flowed from this subcompartment into the GUV lumen, and there, activated the sodium sensitive dye ANG2. We observed the increase of ANG2 fluorescence within the GUV that had a size distribution between 6 and 43 μm ($N = 40$ GUVs, Figure 43). 73% of multicompartment were functional and induced the dye activation via two internal types of artificial organelles within the GUVs. No fluorescence was detected in the remaining 27%, probably due to insufficient loading of gA in NP-Graft, sodium ion in the Na^+Ves , ANG2 into the GUVs, or a combination thereof (Figure 43). As expected, the recruitment sequence did not occur in the absence of the stimuli, showing no fluorescence. Our system was capable of triggering the recruitment of an ion channel from one subcompartment to another to derive the flux of ions from the secondary subcompartment, mimicking the flux of ions across organelles that is involved in several cell processes, such as signal transduction. ^[190]

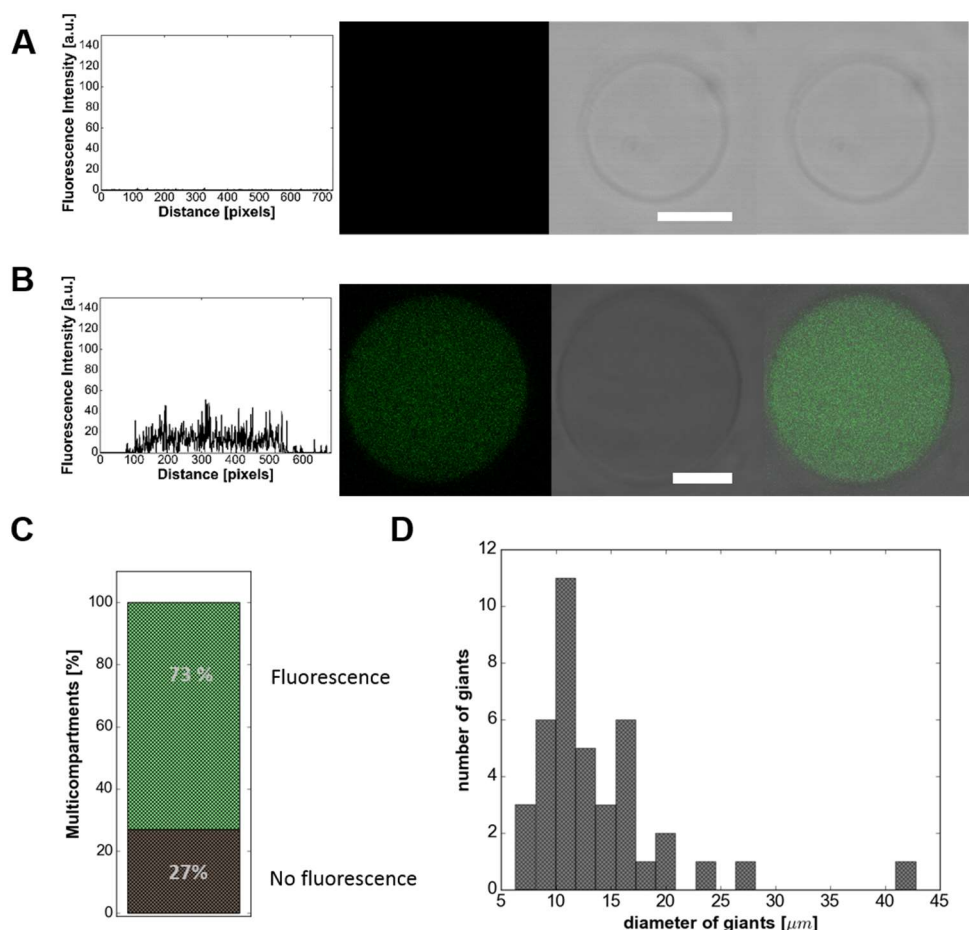


Figure 43. Efficiency of the compartmentalized gA reconstitution into the polymer membrane to import sodium ions in presence of 10 mM DTT after 24 h incubation and corresponding size distribution. (**A-B**) Plot profile of the fluorescence intensity along the diagonal of the image (left), CLSM image of gA loaded NP-Graft and sodium loaded polymersomes (Na^+Ves) in giant vesicles (middle) and corresponding bright field image and merge (right), indicating: (**A**) remain empty (27%, no fluorescence) and (**B**) activation of ANG2 by sodium ions (73%, fluorescence). (**C**) Histogram of efficiency of gA loaded NP-Graft and ANG2 in giant vesicles in presence of DTT. (**D**) Histogram of size distribution of measured gA loaded NP-Graft, sodium loaded polymersomes (Na^+Ves) and ANG2 in GUVs in presence of DTT after 24 h incubation ($N=40$ GUVs). Scale bars, 5 μm .

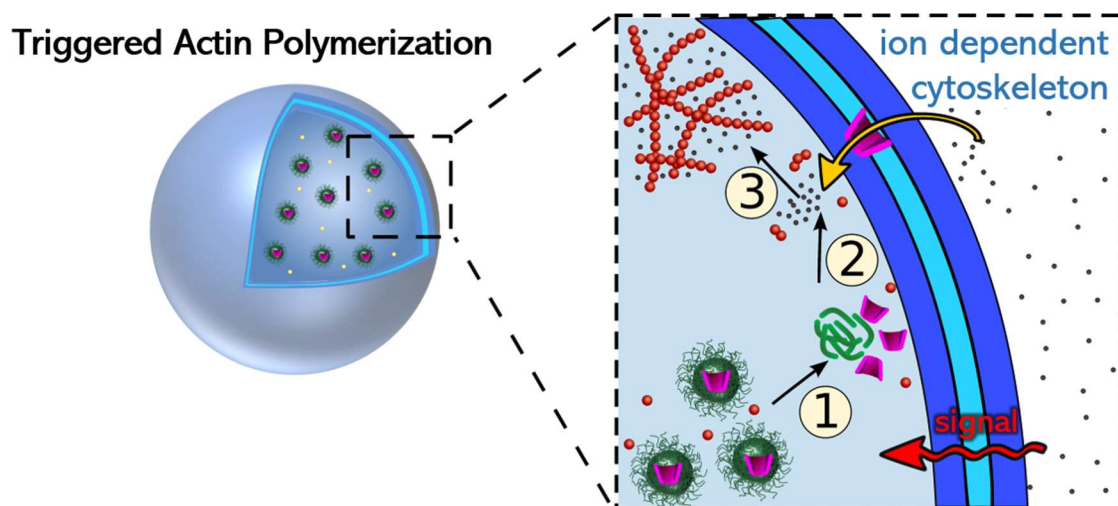
5.3. Conclusion

This chapter presents a new methodology to insert ion channels into giant polymer vesicle membranes. We encapsulated the ion channel gA into the reduction sensitive NP-Graft and used them as subcompartments of a multicompartment assembly. Upon stimuli (DTT) addition to the external medium, the pores were released from their compartment and due to hydrophobic forces, they inserted into the hydrophobic part of the outer polymeric GUV membrane. The activation of the sodium sensitive dye ANG2 in the exterior surrounding medium of GUVs revealed the induced export of

sodium ions from the GUVs using this strategy. In another set of experiments, we studied the *vice versa* scenario, the induced influx of ions from the surrounding solution of GUV upon addition of the signal (DTT). Due to the inside-out recruitment of ion channels to the GUV membrane, ions flowed through the inserted pores which lead to the activation of ANG2 inside the GUV. In the final set-up, we studied induced subcompartment communication via ion channel recruitment from one internal subcompartment to another. We observed that the ion channels were successfully released from NP-Graft and gA then transferred to sodium ions loaded polymersomes (Na^+Ves). The permeabilization of Na^+Ves then led to the efflux of ions from these subcompartments and the ANG2 in the GUV cavity was activated. We showed that the ion channel recruitment was only induced in presence of the stimuli, and the multicompartment stayed in a silent mode in absence of the stimuli. The triggered recruitment and functional insertion of gA into the membrane of the multicompartments via responsive sacrificial subcompartments and release of sodium ions from non-responsive subcompartments demonstrates that we were able to successfully introduce a sequential signaling pathway into our one and two-type multicompartments. For proof of concept, we studied the recruitment of gA and the passage of Na^+ ions. The induced reconstitution of gA allowed the passage of sodium ions “on demand”, either from outside or *vice versa*. Other appropriate ions can be tested with this system and in the future studies, other pores/channels can be loaded into NP-Graft to study the triggered permeabilization of the outer membrane to other ions or molecules.

6. Cytoskeleton Mimic in Multicompartments

Here, the formation of a cytoskeletal actin network within a cell-sized polymeric vesicles is demonstrated. Actin polymerization was induced within polymeric GUVs due to ion influx after biopore recruitment from the environment or internal subcompartments into the GUV membrane to change the interior characteristics within the polymer vesicles.



PARTS OF THIS CHAPTER ARE A MANUSCRIPT IN PREPARATION:

SAGANA THAMBOO*, ANDREA BELLUATI*, ADRIAN NAJER, VIVIANA MAFFEIS, CLAUDIO VON PLANTA, IOANA CRACIUN, CORNELIA G. PALIVAN^x, WOLFGANG MEIER^x, MULTICOMPARTMENT POLYMER VESICLES WITH ARTIFICIAL ORGANELLES FOR SIGNAL-TRIGGERED CASCADE REACTIONS INCLUDING CYTOSKELETON FORMATION, *ADVANCED FUNCTIONAL MATERIALS*, 2020, 2002949.

**These authors contributed equally*

6.1. Introduction

Combinations of different functionalities with high spatiotemporal control remain challenging through bottom-up assembly of synthetic and biological components. A key task in moving towards the creation of artificial cells is the incorporation of a cytoskeleton mimic. In nature, cell mobility, shape, cell division and intracellular transport are all dependent on the dynamic assembly/disassembly of cytoskeletal components (e.g. actin) in combination with the action of motor proteins (e.g. myosin).^[191] Reproduction of such a complex system that allows reproducing mobility, division and transport using manmade autonomous artificial cells seems achievable, but many hurdles.^[61] With respect to cytoskeleton components inside artificial assemblies, actin polymerization has mainly been studied using giant liposomes to observe membrane transformations that underly cell motility.^[62] Unfortunately, liposomes are very unstable and generally not compatible with physiological salt, especially when proteins are encapsulated.^[192]

Herein, a complex multi-component protocell is presented that forms a cytoskeleton within a polymeric GUV using a minimal set of biological cytoskeleton components (purified actin proteins). The addition of an actin monomers yielded triggerable formation of an internal cytoskeletal network (actin polymerization) via channel forming ionophore recruitment from the environment or internal subcompartments. We show that the subcompartments can be activated selectively to kick start ionophore recruitment, and subsequently that actin network formation can be triggered within a polymeric GUV. We studied the change in viscosity before and after actin polymerization in a two-type multicompartment system. Our demonstration of precise temporal control over spatially confined components within a bottom-up fabricated protocell that performs complex cascade reactions upon applying a stimulus.

6.2. Results and Discussion

6.2.1. Actin Filament Polymerization in Synthetic GUVs

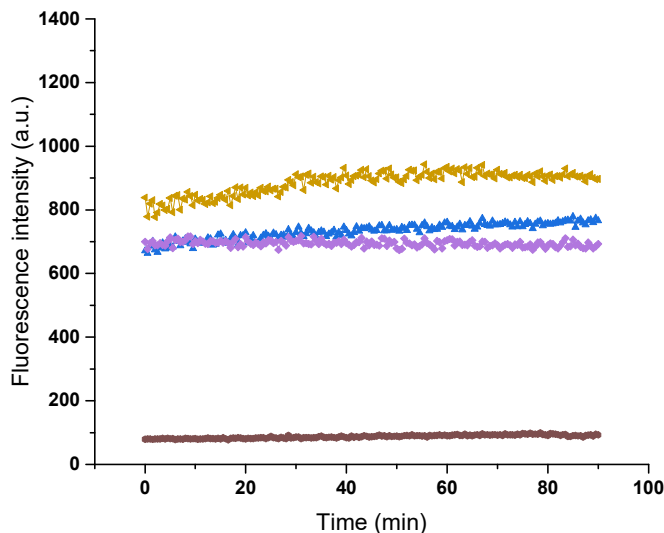


Figure 44. Pyrene fluorescence assays of G-actin polymerization in the dependence of salts. Actin-pyrene in sucrose (300 mM, brown), in CaCl₂ (100 mM, purple), in KCl (100 mM, blue) and in MgCl₂ (100 mM, gold). Almost immediately after mixing the solutions (t=0 min), the actin polymerized, showing stable filaments for the following 90 minutes. Ex/Em 365/407 nm.

To explore the potential of the presented strategy, we investigated the formation of an actin cytoskeleton in our biomimetic systems; mimicking a basic component of cells responsible for both, structural stability and dynamic shape modifications. We developed a protocol to load purified monomeric actin (G-actin) in combination with the passive crosslinker filamin into our polymer-based GUVs. Upon addition of ions and corresponding ionophores such as ionomycin (IoNo) or gramicidin (gA) to the external medium, the induced passage of Mg²⁺ and Ca²⁺ (IoNo) or K⁺ ions (gA) through the GUV membrane initiates actin polymerization inside the lumen of the polymer protocell (Figure 46A). Ion-mediated actin filament formation is depended on the concentration and type of salts in its surrounding; this behavior depends on nonspecific interactions of specific cation binding sites on actin filaments, which are known to regulate biological functions such as cellular motility or shape and can also be replicated in non-living liposomes. [19, 141, 142, 144, 153, 163]

We first confirmed fluorometrically, the concentration ranges for polymerization with monomeric pyrene-actin in solutions, showing formation of filaments in presence of various salt solutions (KCl, CaCl₂ and MgCl₂) (Figure 44). To enhance the creation of an ordered network, we mechanically stabilized our actin cytoskeleton (enriched mixed with ATTO488-G-actin for its visualization) with the actin-binding protein filamin,^[24] confirming the formation of actin-filamin networks formed in ion-rich solutions and not in HEPES solution(Figure 45).

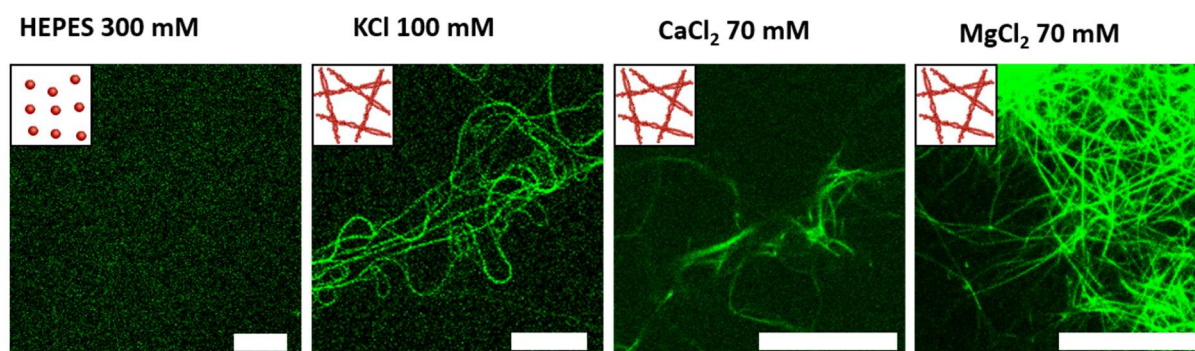


Figure 45. Confocal images of actin networks polymerized in bulk solution in presence of different solutions. In presence of the crosslinker filamin, G-actin stays in its monomeric form in HEPES buffer (300 mM) in contrary to the solutions containing KCl, CaCl₂ and MgCl₂ induce actin polymerization and form actin-filamin networks (green). The samples were incubated for 3 h. Scale bars, 20 μ m.

We then proceeded to load the actin proteins into the GUVs (“Actin GUVs”), yielding results qualitatively consistent with the data published earlier in liposomes loaded with actin bundles.^[140, 141, 149] The hydrophobic Bodipy630/650 was used to visualize the GUV membrane. As shown by CLSM (Figure 46B, Figure 47), in absence of ionophores and/or salts the actin monomers stayed in their monomeric form within the GUV (no observed filaments).

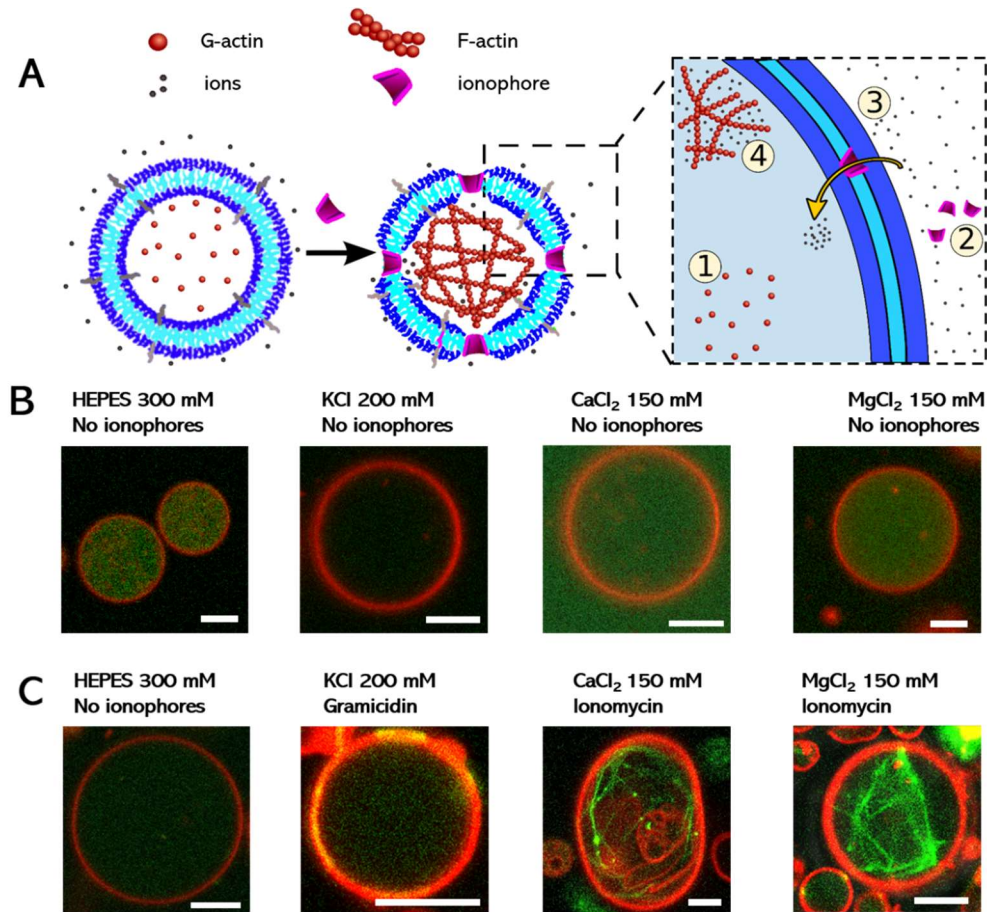


Figure 46. Actin filament polymerization in synthetic GUVs. Actin monomers (G-actin) and the actin crosslinker filamin was loaded into giant vesicles after 24 h incubation. Pores (gA or IoNo) were introduced to the vesicle solution resulting in permeabilization of the GUV membrane towards specific ions (K^+ or Ca^{2+} and Mg^{2+}). **(A)** Schematic representation of the actin polymerization in GUVs. **(B)** In absence of pores, the monomers stayed intact, and no filaments were formed since no ions could enter the GUV cavity. **(C)** When pores were added to the surrounding solution, they reconstituted into the membrane boundary of the GUV. Then ions entered the GUV cavity, actin starts to form filaments and the bundling agent filamin crosslinks the filaments into a network. Scale bars, 5 μm .

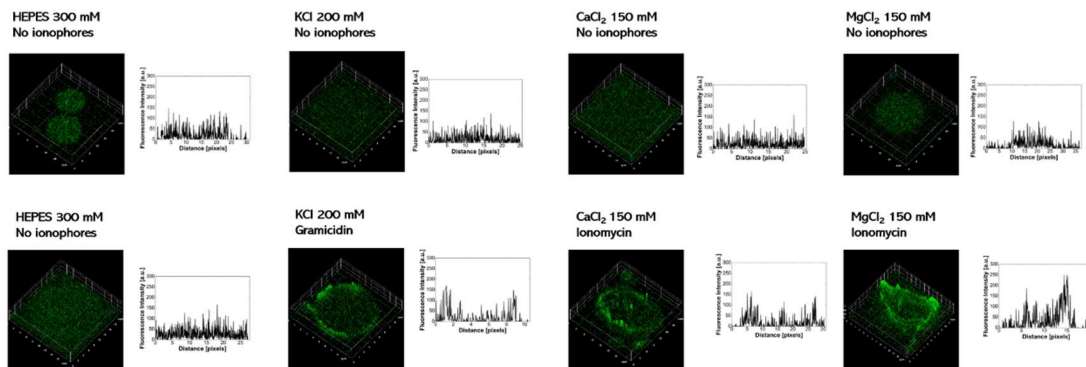


Figure 47. Surface profile along the surface (left) and plot profile along the diagonal (right) of the actin polymerization in GUVs (fluorescence intensity of the CLSM images of Figure 46).

When pores and salts were added to the outside of Actin GUVs, filaments were formed within 24 h, in 88.5% of the vesicles (N=200 GUVs) (Figure 46C, Figure 47, Figure

48), thanks to the diffusion of K^+ through membrane-inserted gA, or Mg^{2+}/Ca^{2+} due to IoNo, with similarly-shaped filaments regardless of the salts.. Actin filaments formed either ring-like structures directly underneath the GUV membrane (inner leaflet), following the round membrane by bending the actin filaments, or formed web-like network structures within the GUV cavity (Figure 46, Figure 47).

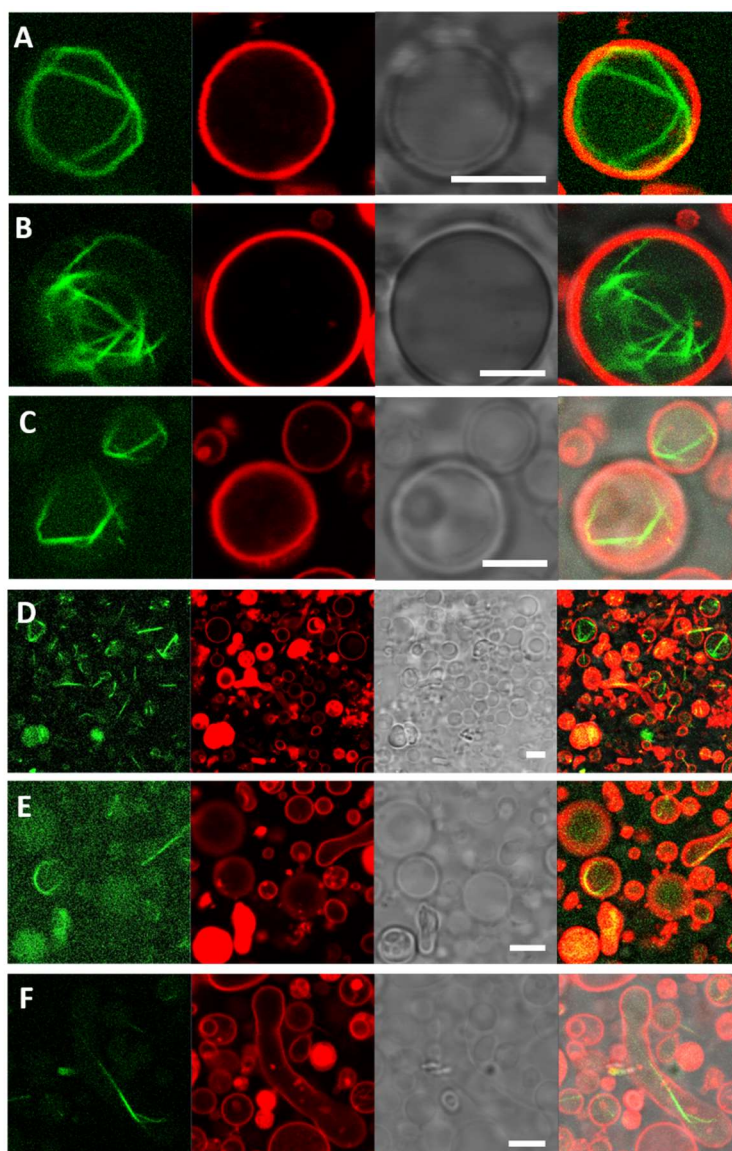


Figure 48. Confocal images of equatorial plane of actin networks confined in cell-sized GUVs. Confocal images of actin filaments polymerized inside cell-sized synthetic GUVs. (A-F) Actin filaments (green, left), polymer GUV membrane (red, left middle), bright field image (right middle) and merge (right) in presence of IoNo and 150 mM $MgCl_2$. The samples were incubated for 24 h. The samples are from the same batch as Figure 46. Scale bars, 5 μm .

To better visualize the morphology of the GUV cytoskeleton, we additionally used a high resolution microscopy technique, 3D structured illumination microscopy (3D-

SIM), showing that the actin network within the GUVs is composed of both thin actin filaments and actin bundles with thicker fibers (Figure 49).

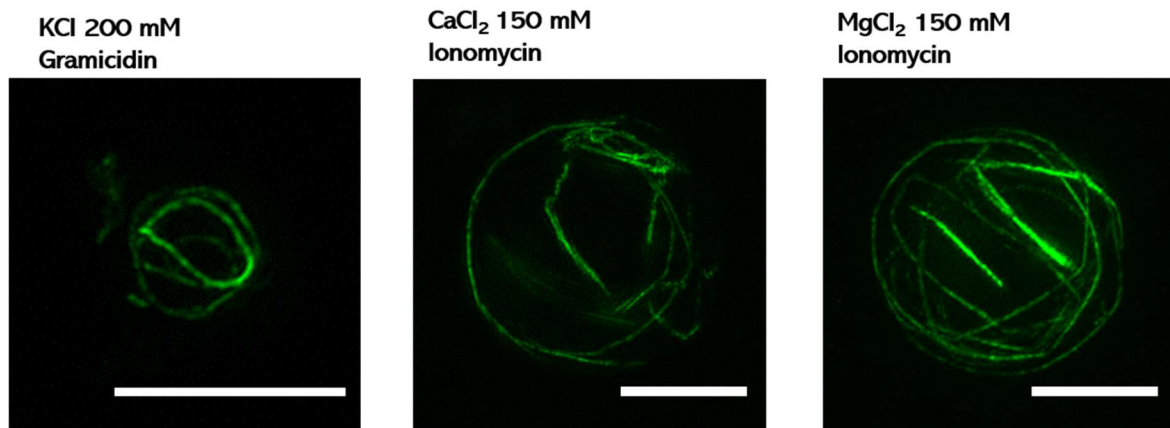


Figure 49. Projections of actin filaments (green) polymerized within GUVs in presence of pores and ions recorded with super-resolution 3D-SIM. High resolution images (3D-SIM) of Actin GUVs in salt solutions (200 mM KCl, 150 mM CaCl₂ and 150 mM MgCl₂) in presence of corresponding pore (gA, IoNo) after incubation of 48 h. Scale bars, 5 μm.

Note that any free, non-encapsulated actin was below the critical concentration of actin and therefore actin was too diluted to form any filaments outside the G-actin loaded GUVs. We tested the same conditions as present in the surrounding solution of Actin GUVs with free actin in solution and did not detect any actin filaments (Figure 50). Therefore, no further purification was necessary. In conclusion, we could successfully trigger salt-induced actin polymerization in polymeric GUVs via addition of ionophores.

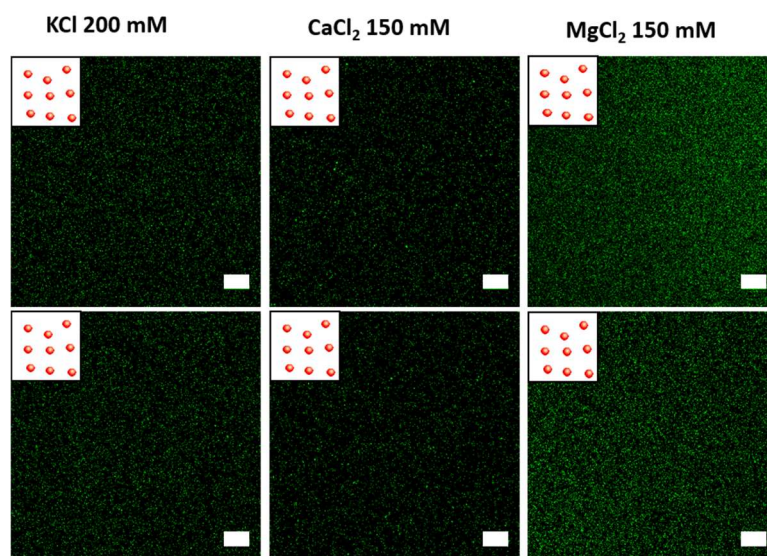


Figure 50. CLSM image of actin in solution in presence of salts (200 mM KCl, 150 mM CaCl₂ and 150 mM CaCl₂) with same concentrations of actin, actin488 and filamin similar to outside concentration in all GUV experiments, demonstrating that additional purification is not needed, since no filaments are formed after 24 h. Scale bars, 20 μm.

6.2.2. Actin Polymerizing Multicompartment

In a final step of increasing complexity of our polymer-based protocells, we aimed to combine triggerable artificial organelles (Chapter 4 - 5) with cytoskeleton components (Figure 46) to achieve a scenario of signal-induced cytoskeleton formation inside our protocell while the signal is first transduced via responsive subcompartments (“Actin MCs”). The actin filaments should only form in the presence of an externally added signal that acts on the stimuli-responsive subcompartments. Upon release of ionophores from these artificial organelles and inside-out insertion into the GUV membrane, ion influx from the environment should trigger actin polymerization (Figure 51A).

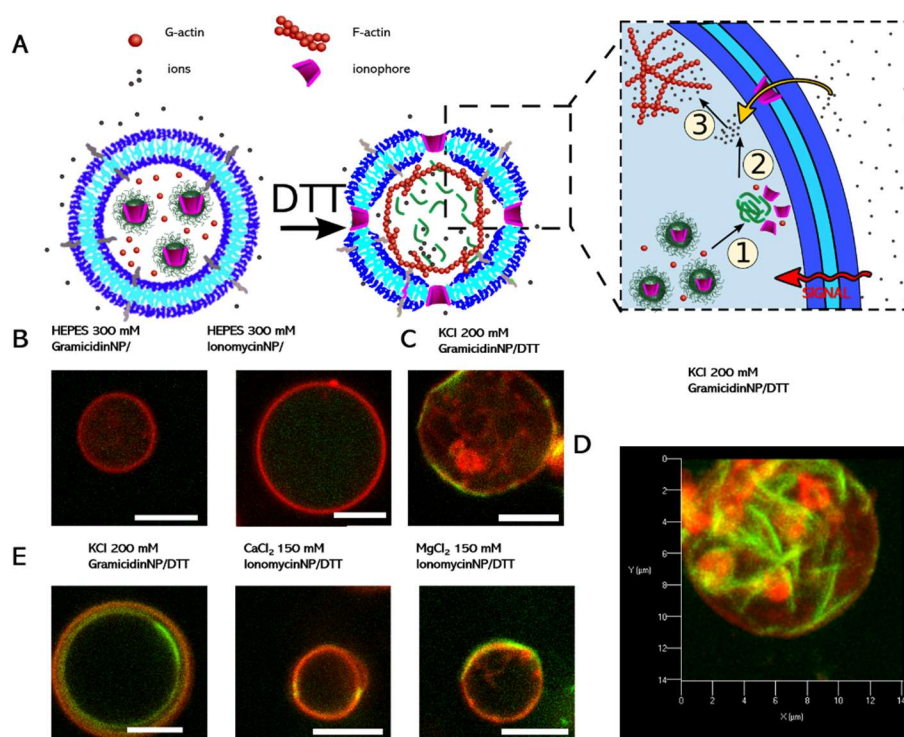


Figure 51. Stimuli-triggered actin polymerization in synthetic multicompartment (“Actin MCs”). (A) Schematic representation of pore mediated import of ions resulting in the formation of actin filaments. Upon DTT addition, the encapsulated pores are released from its NP-Graft and inserts into the GUV membrane boundary. Ions enter from the surrounding solution into the cavity of the GUV, where the actin monomers start to polymerize into filamentous structures. (B) CLSM imaging of actin monomer (G-actin, green) and crosslinker filamin co-loaded GUVs (red) remaining in its monomeric form in absence of salts and pores. (C) One slice of Figure 3D. Actin filaments (green) and GUV membrane (red), where actin polymerization is induced in presence of DTT. (D) Projections of actin filaments (green) in GUVs (red) via stimuli-responsiveness via internal subcompartments, were imaged with CLSM. The actin samples were incubated for 24 h. Each single slice is shown in Figure 53. (E) CLSM micrographs of actin filaments (green) in the lumen and inner leaflet of the GUV membrane (red), where actin polymerization is induced in presence of DTT. Scale bars, 5 μm.

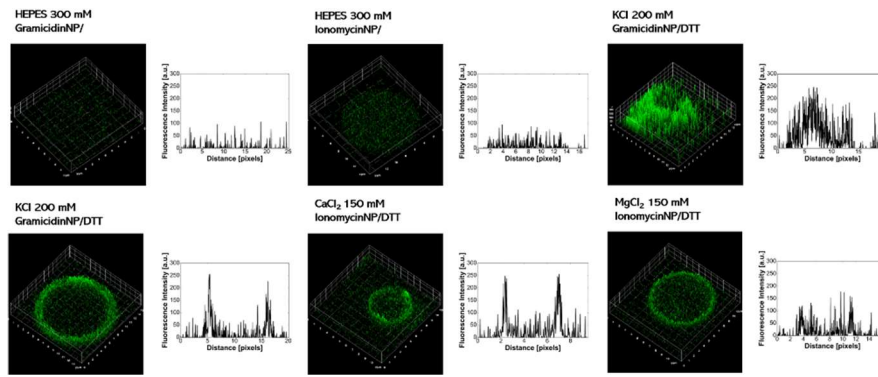


Figure 52. Surface profile along the surface (left) and plot profile along the diagonal (right) of the stimuli-triggered actin polymerization in multicompartments (fluorescence intensity of the CLSM images of Figure 51).

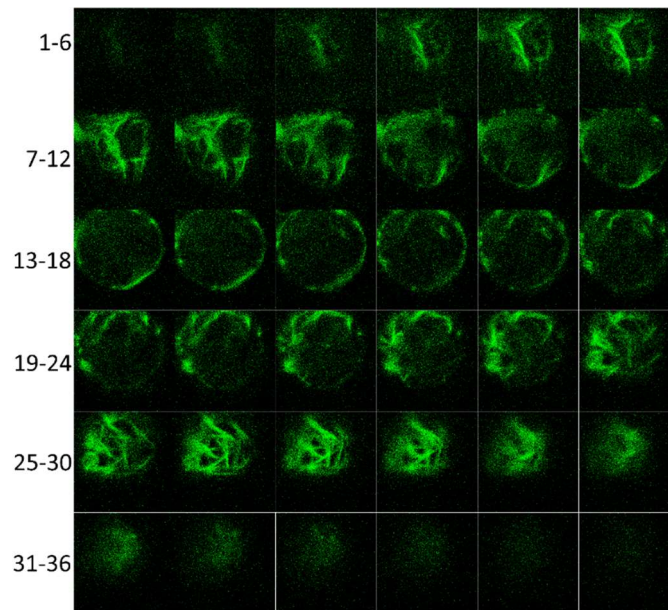


Figure 53. Projections of actin filaments (green) in GUVs via stimuli-responsiveness via internal subcompartments, were imaged with CLSM. The sample was incubated for 24 h. Slices 1-36 of Figure 3D are shown here.

Subcompartments (NP-Graft), carrying either the ion channel gA or the IoNo complex, were co-loaded with actin monomers and filamin in GUVs. Actin stayed monomeric within the GUV in absence of the signal (DTT) and/or ions (Figure 51B, Figure 52, Figure 53, Figure 54). In presence of DTT, the pore-loaded NP-Graft disassembled and released their cargo (gA or IoNo). As before, gA was incorporated into the GUV membrane, allowing the passage of K^+ from the exterior solution, leading to the polymerization of actin in the GUV. For the passage of Mg^{2+} or Ca^{2+} ions, that are also known to induce actin polymerization, we incorporated Iono to the GUV membrane from outside. (Figure 51C-E, Figure 52, Figure 53). Observations of mostly cortical

rings in the case of triggered actin polymerization via responsive subcompartments could be due to the much limited number of ionophores loaded into NP-Graft . In this case, a lower number of ionophores were inserted into the GUV membrane. Limited amount of ion influx could lead to a more localized actin polymerization directly beneath the membrane where the local concentration of ions will be highest upon channel insertion. In comparison, adding a high concentration of ionophores from the outside (Figure 46) allows fast and plentiful influx of ions that leads to higher chance of creating extended networks throughout the GUV lumen.

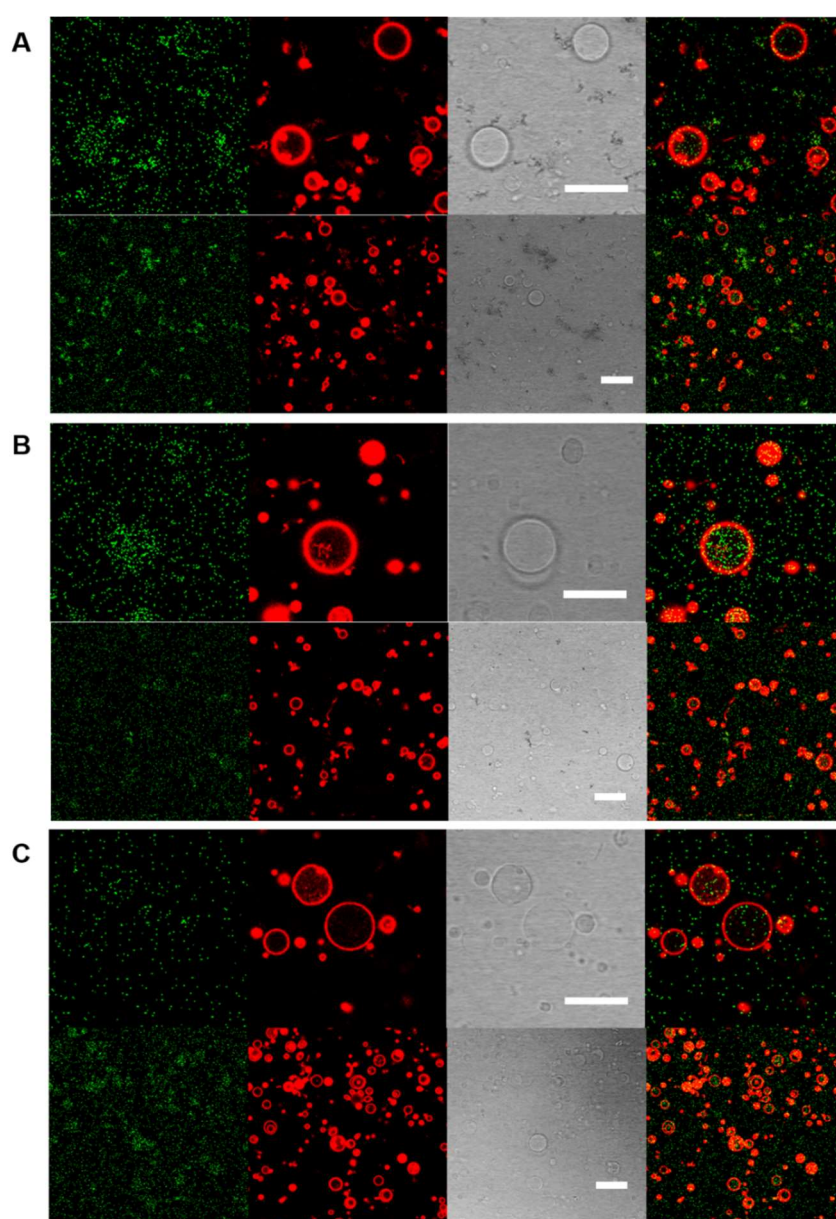


Figure 54. CLSM image of actin MCs in presence of salts ((A) 150 mM CaCl_2 , (B) 150 mM MgCl_2 and (C) 200 mM KCl) and absence of DTT after 24 h. Scale bars, 20 μm .

We again employed *in situ* FCS measurements to study the viscosity changes inside our polymer protocells due to triggered actin polymerization. We used GUVs filled with IoNo-loaded NP-Graft and non-responsive fluorescent subcompartments (SRBVes). We measured the diffusivity of the labelled non-responsive subcompartments (SRBVes) before and after selective disassembly of NP-Graft by adding DTT and subsequent formation of filaments after ion influx. Based on the change in SRBVes diffusion times from 4555 μs to 70277 μs of otherwise unchanged vesicles, we could calculate a change of internal viscosity from $8.9 \cdot 10^{-4} \text{ Pa} \cdot \text{s}$ to $1.4 \cdot 10^{-2} \text{ Pa} \cdot \text{s}$ after polymerization. The actin filaments within the GUV made the lumen more crowded, replicating the molecular crowding of cells (Figure 4F). The actin filaments within the GUV made the lumen more crowded replicating the molecular crowding of cells (Figure 55). We successfully demonstrated that polymeric membranes and the actin biopolymers regulate each other's conformation in a gentle force balance. The actin component in our multicompartment system combined with functional artificial organelles provides a complex and highly controlled active material, a further step towards mimicking the complex mechanisms involved in cellular movement, shape, cell division and intracellular transport.

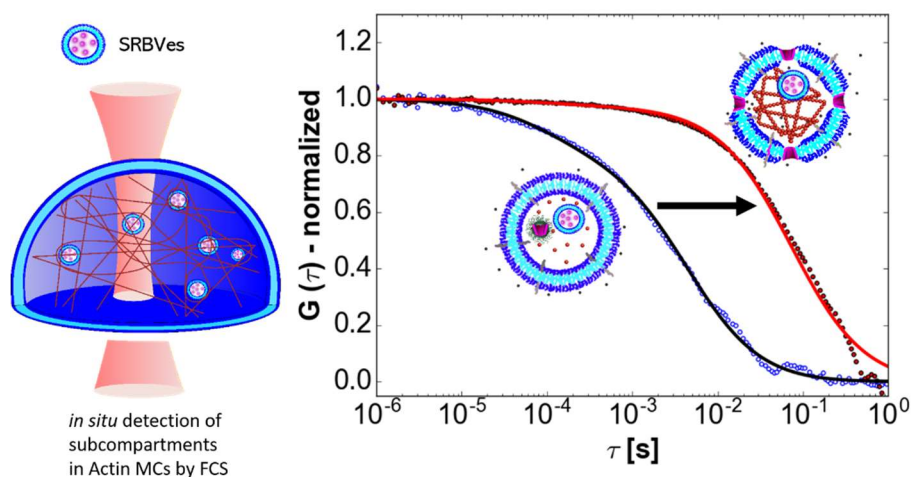


Figure 55. FCS autocorrelation curve of SRBVes of two-type multicompartments before and after triggered actin filament polymerization. Change in diffusion time can be indicated as viscosity change. (N=3 GUVs before and after addition of DTT).

6.2.3. Actin Related Morphology Changes

Filamentous cytoskeletal elements can cause morphology changes for the vesicular structures. [193] From previous publications of actin filaments in liposomes, we know that small membrane bending rigidity leads to finger-like membrane protrusions, while large bending rigidity of the membrane leads to cortical rings (suppressing membrane protrusions). When a filament is encapsulated in a deformable cavity, it leads to a balance between the energy cost of the filament bending and the energy cost for the cavity deformation. Tsai et al has worked on the control of the shape of lipid membrane by actin bundles. [141]

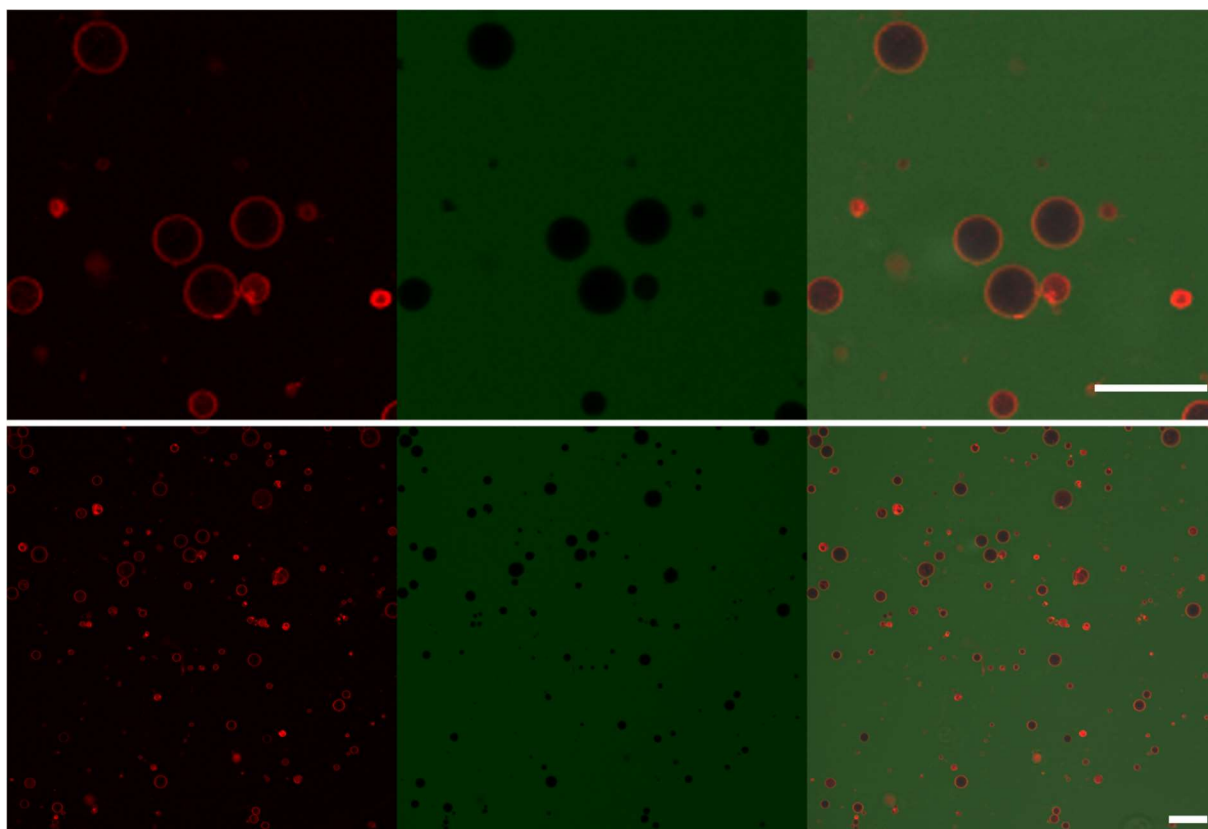


Figure 56. PMOXA₆-PDMS₆₅-PMOXA₆-PEG₃-N₃ GUVs (red) are spherical when no actin was loaded. Carboxyfluorescein was added to the outside solution of PMOXA₆-PDMS₆₅-PMOXA₆-PEG₃-N₃ GUVs to show that the membrane is not permeable to small hydrophilic compounds. Scale bars, 20 μ m.

In absence of actin, the GUVs assumed mainly to energetically favor spherical shapes (Figure 56), likewise when loaded with monomeric actin (1% non-spherical shape, N=200 GUVs) (Figure 46B, Figure 51, Figure 54). However, we also observed

membrane morphology changes, due to the bundled up confined actin filaments (28.5%, N=200 GUVs) (Figure 57, Figure 58).

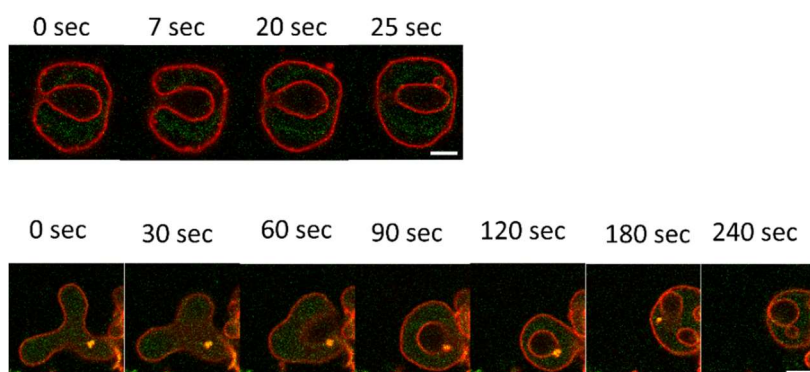


Figure 57. Morphology changes of Actin MCs after 24 h incubation. Confocal images of actin networks polymerized inside cell-sized synthetic GUVs via internal IoNo loaded NP-Graft in presence of DTT. Actin filaments (green, left), polymer GUV membrane (red, left middle), bright field image (right middle) and merge (right) in presence of DTT and (A) 150 mM MgCl₂ or (B) 150 mM CaCl₂. Scale bars, 5 μm.

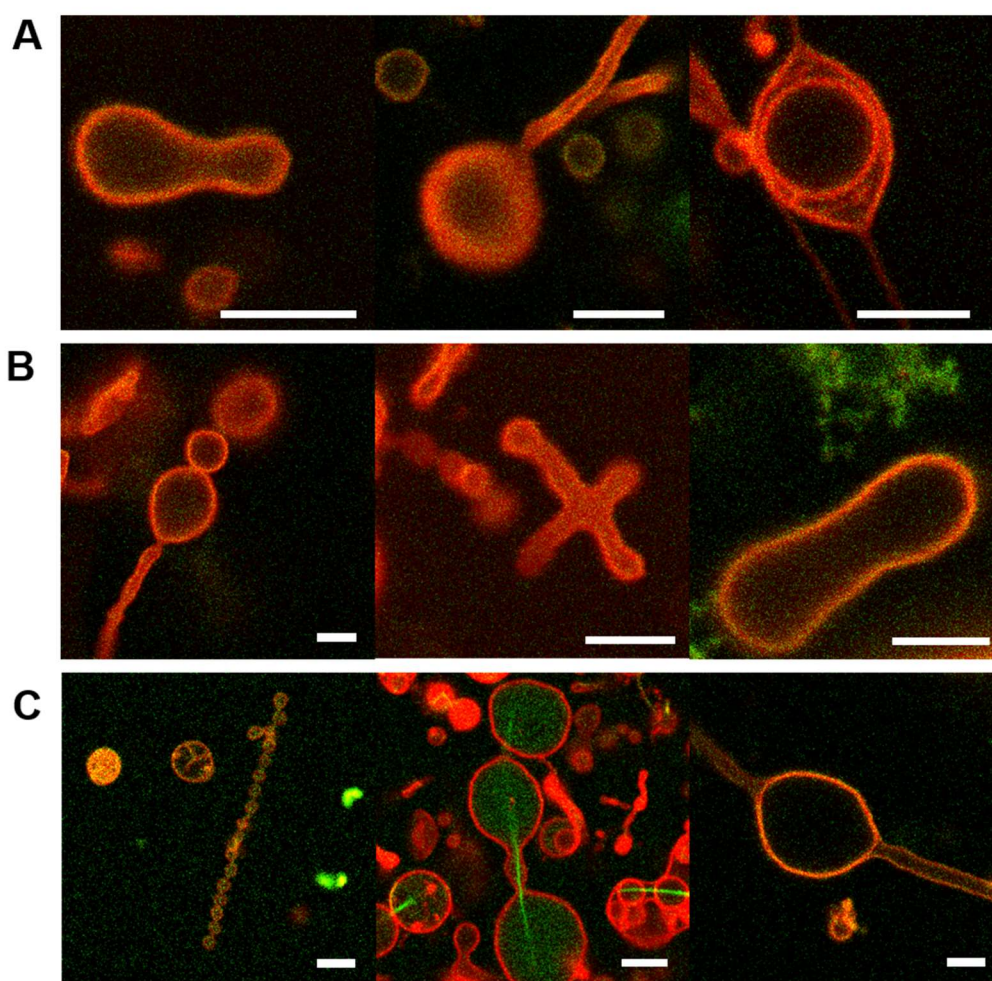


Figure 58. Morphological characterization of polymer based GUVs with polymerized filamin-actin networks. CLSM images of non-spherical polymer structures formed in after inducing actin-polymerization in presence of (A) 200 mM KCl and gA, (B) CaCl₂ and 150 mM IoNo, and (C) 150 mM MgCl₂ and IoNo. The samples were incubated for 24 h. Scale bars, 5 μm.

A variety of morphologies range from vesicular structures, elongated worm-like structures, finger-like membrane protrusions on vesicles, multicompartmental structures, fused vesicles and more were observed (Figure 57 ,Figure 58). Previous studies have revealed such changes in morphology with actin filaments in lipid structures, including protruded shapes, where the force for membrane deformations (elongation, contractions and protrusions) is generated in crowded condition in the compartment same as in living cells. ^[141, 194] Lipid membranes are known to be fluid-like and easily deformable compared to polymeric membranes that are less fluid/deformable when the membrane is thicker than the lipidic one. ^[173] The mechanical stress of actin filaments make giant liposomes more deformable and less stable; ^[194, 195] our synthetic actin-GUVs were stable for at least 48 h. Concentration of actin and type of crosslinker affect the stiffness of the actin filaments. Stiffer actin bundles remain straight resulting in elongation of the vesicular structures or even puncturing the membrane due to inability to bend the actin bundles. ^[141]

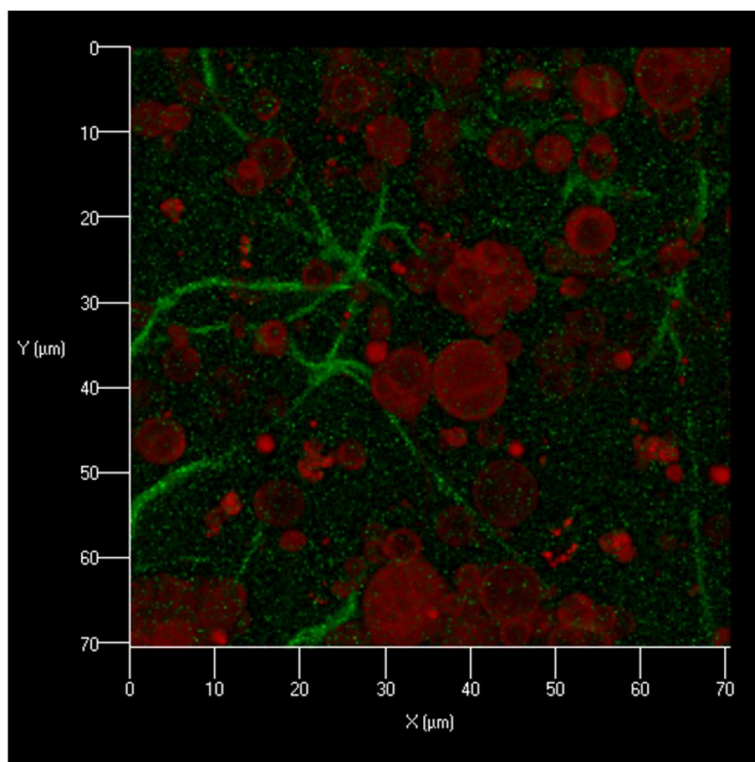


Figure 59. Projections of actin filaments (green) polymerized in GUVs (red) via stimuli-responsiveness via internal subcompartments (IoNo loaded NP-Graft) were imaged with CLSM in presence of 10 mM DTT and 150 mM MgCl₂. The filaments pierce out of the GUVs and form networks between various GUVs. The samples were incubated for 24 h.

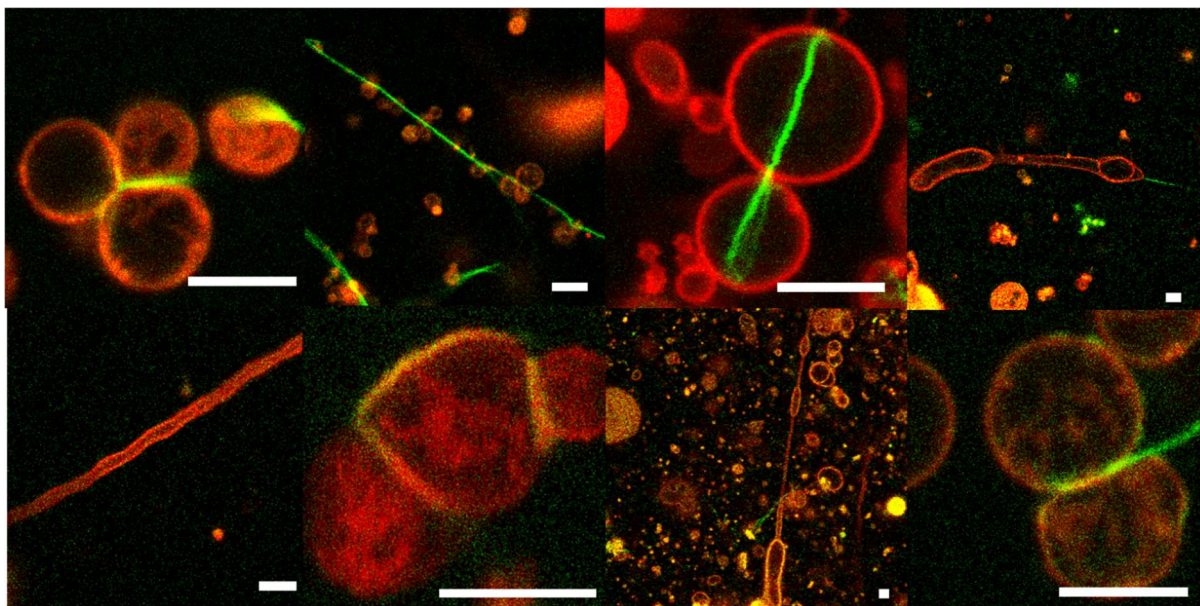


Figure 60. Confocal images of interactions of the contractile actin network (green) with the GUV membrane (red). The samples were incubated for 24 h. Scale bars, 5 μm .

On occasion, the stiff filaments pierced through the polymeric membrane and connect polymer compartments (Figure 59), sometimes even connecting actin protrusions along the inner leaflet between GUVs (Figure 60). Also in nature, the membrane tension of cells acts as a regulator of cytoskeleton architecture.^[196] Various parameters such as concentrations of actin, filamin, ions, pores, stiffness of the membrane and of the filaments and more are influencing the overall shape of the GUVs, which has to be studied in more detail to depict the mechanism by which these structures are formed and how they dynamically change over time. In most cases, we observed networks of actin within the GUVs and ring-like formations underneath the membrane; both can very clearly be seen in the high resolution SIM images (Figure 46C-D, Figure 49, Figure 51C). This is due to the vesicular morphology of our protocells that usually forces the polymerized actin to organize into cortical rings or web-like construct, minimizing the energy cost associated with bending of filaments, as demonstrated in lipid-based systems.^[141]

6.3. Conclusion

The actin polymerization in polymer vesicle based protocells was studied to better understand aspects of cell behavior. Actin filaments were polymerized when pores were introduced, and ions pass the membrane of the microscale polymer vesicles that were loaded with monomeric actin and cross-linking protein filamin. We inserted gA for the passage of K^+ and IoNo for Mg^{2+} and Ca^{2+} to induce actin polymerization in the GUV membrane. By using fluorescently labelled actin, the actin filaments could be observed via CLSM after focusing inside the GUVs. The cell-like system was further developed for a stimuli-triggered actin formation using hierarchical approach in compartmentalization. When the biopores (gA or IoNo) in reduction sensitive NP-Grafts were co-loaded with actin monomers in GUVs, the actin polymerization only took place, when the pores were released due to the stimuli (DTT). The pores recruited into the polymer membrane and allowed the ion influx. Using a two-type multicompartment system, we observed an increase in diffusion time of the non-sensitive subcompartments within the GUV due to the stimuli-triggered actin polymerization. The co-loaded SRBVs subcompartments were detected via *in situ* FCS and the results reveal a change in viscosity after adding the stimuli and starting the actin polymerization.

In conclusion, we demonstrated that our hybrid protein-polymer protocell system can be used for the formation of a cytoskeleton using confocal microscopy, fluorescence correlation spectroscopy and high resolution imaging (3D-SIM). Additionally, a complex signal transduction via a cascade for actin cytoskeleton formation was achieved, where our responsive multicompartment was used to modify its internal structure and content by selectively following a chemical stimulus, mimicking aspects of cell behavior. This complex and bio-inspired construct is a promising platform for the development of smart materials, sensing external factors and responding accordingly. We envision that the reported strategy has the potential to include even

add more complex functionalities by exchanging the trigger (signaling molecules), subcompartments (artificial organelles) and surface components to progress towards creation of an artificial cell. With the ultimate goal to develop a synthetic cell with the ability to autonomously move, grow and divide, we created a multifunctional system using synthetic multicompartment vesicles with an active soft matter to imitate the dynamic cytoskeleton and cell motility.

7. General Conclusion and Outlook

The complex architecture of living cells including simultaneous action of a myriad of dynamic processes are the inspiration for creating sophisticated protocells with the final goal of bottom-up assembly of artificial cells. This thesis summarizes a particular strategy to design and construct a synthetic protocell model based on amphiphilic block copolymer self-assembly. Particularly, a simple non-assisted film rehydration method was used, to closely resemble the natural circumstances that were most likely involved in the creation of natural cell precursors. Significant advances in the formation of different types of multicompartments were made and derived a strategy to study stimuli responsive material to exhibit simple functional and structural cell resemblance. Membrane functionality, sensitivity towards a specific external stimuli and internal response of the multicompartment system was investigated. A simple and well-studied approach proposes a basic system towards understanding the emergence of life and serves as a future scaffold for an artificial cell. Activity or permeability driven by an external stimuli without compromising the polymeric architecture lead to the proof of concept of simple cellular functions in cell mimics using a multicompartmentalized system. Inspired by signaling pathways in cells, a strategy to auto-trigger changes within micrometric multicompartments was developed that induced specific responses based on signaling cascades. First, multicompartments were generated by encapsulating various subcompartments (micelles, polymersomes and nanoparticles) inside synthetic GUVs, which remained stable for extended periods of time without *in situ* aggregation and their assembly was studied in detail by FCS/CLSM. Hence, the triggered response of the multicompartment towards the stimuli was recorded directly inside individual GUVs to obtain detailed information on multicompartment functionality and stability.

The selective permeability of the compartment membrane towards the reducing agent DTT was then used to induce a reductive milieu in the lumen of GUVs that disassembled the sensitive subcompartments, while no effect was observed for the non-responsive subcompartments. Desired molecules (enzymes, reporter compounds) together with corresponding partners (substrates, biopores) entrapped in responsive nanoparticles were simultaneously co-encapsulated within GUVs to obtain a spatial segregation. Upon penetration through the membrane of GUVs, DTT induced the disintegration of the sensitive nanoparticles and subsequent release of their content. The substrates were able to encounter the enzymes and trigger their reaction. In another case, the ionophores gA were released and recruited to the GUV's membrane and enabled a constant in/out flow of sodium ions. These particular systems successfully activated an enzymatic reaction and selectively recruited ionophores to the GUV membrane upon arrival of the stimulus. Inside-out ionophore insertion allows modulating outer membrane permeability on demand for secondary signaling. The latter allowed the influx and efflux of ions across the polymer membrane and was the basis for the next steps of formulating more complex reaction cascades within polymer-based multicompartments.

To mimic the cellular cytoskeleton, actin polymerization was triggered within the interior of a synthetic compartment. Notably, our multicompartment systems provides attributes to achieve a selective biopore recruitment that was used for a multi-step reaction involving the stimuli-triggered construction of an actin network within polymeric GUVs. FCS/CLSM technique provides a strong tool for the detection of nanosized compartments inside GUVs as demonstrated throughout this thesis. Additionally, FCS/CLSM also allows characterization of biophysical mechanisms such as crowding within GUVs. An increase in diffusion time was recorded for non-responsive subcompartments after triggering actin polymerization inside multicompartments. This can be attributed to a change in viscosity and gives another indication of successful cytoskeleton formation. In the future, quantitative analysis of

the actin loaded GUVs in terms of viscoelasticity and tension can be studied to generate more detailed knowledge of the interplay between actin fibers and the polymer membrane. The combination of the three main cytoskeletal components (actin filaments, microtubules and intermediate filaments) within the GUVs would be interesting to study with respect to morphology of the synthetic systems.

A major drawback of polymer-based systems is that the membrane components cannot be derived *in situ*, in contrary to lipid-based systems using fatty acid synthase. Therefore, the phenomenon of replication cannot be mimicked with existing technology. A possible machinery to reproduce these elements is the use of polymerization-induced self-assembly (PISA), a one-pot technique to generate polymer based structures.^[197] In order to maximize the amount of various processes occurring inside our multicompartments, the next step is to also allow substrates and products to be exchanged in a controlled matter through the outer membrane and involve further biologically relevant enzymatic reactions. This might be realized by triggered membrane protein channel recruitment for the passage of molecules with higher molecular weights. Technically it should be possible, however one main challenge will be to keep any system including complex pathways stable over time. Other physicochemical triggers such as pH, temperature or UV could be added to allow specific changes inside the multicompartment system or to create different communication strategies between multicompartments or with the external environment.

Our strategy has as advantages a very simple preparation method, high versatility and a straightforward manner to induce auto-controlled sequences of reactions/changes inside microcompartments. As anticipated, our multifunctional system went beyond pure nanotechnological terms and encroached into molecular logics territory, where the changes of internal architecture led to changes in the GUVs behavior. The use of semi-synthetic materials will have to be further investigated, as it has the potential of

bridging the well-known biochemical logics and the growing field of pure molecular logics. This design showed remarkable versatility, robustness and controllability, demonstrating that multicompartment polymer-based assemblies offer an ideal scaffold for the development of complex cell-inspired responsive systems for future applications in biosensing, catalysis and medicine.

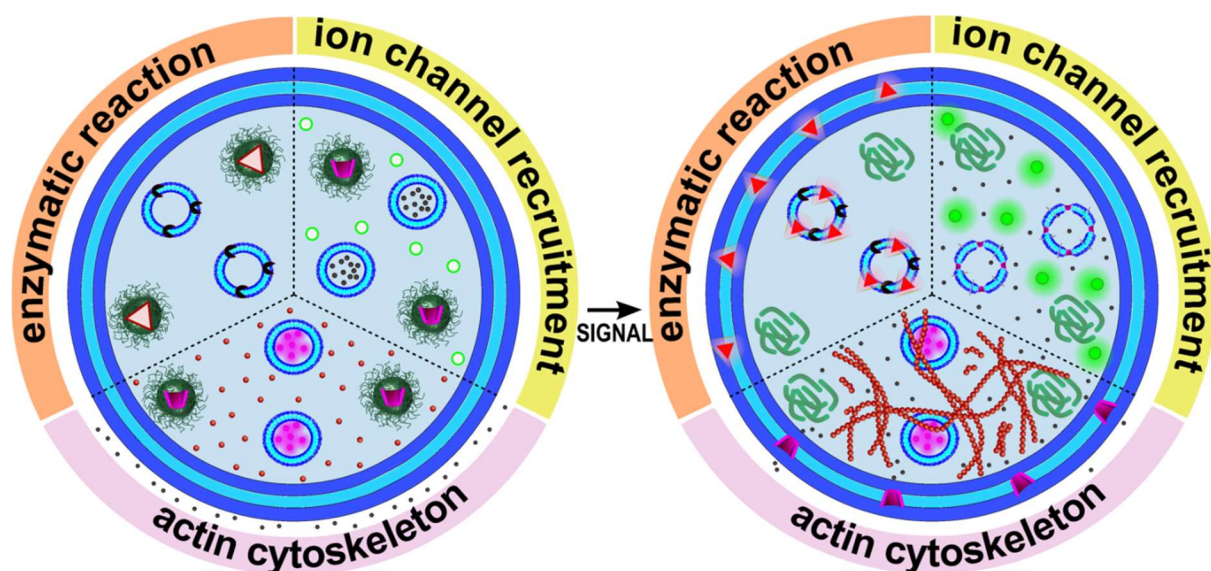


Figure 61. Artificial Cell Schematic of polymersome-based multicompartment system to study enzymatic reactions, ion channel recruitment and actin cytoskeleton.

8. Experimental Section

This chapter comprises the material and methods used for the individual experimental procedures, including chemicals, detailed setups and instruments for the characterization. Parts were reproduced and modified with permission from the corresponding references ^[1] (Copyright John Wiley and Sons, 2019) and parts of this chapter is prepared for a manuscript in preparation.

Sagana Thamboo, Andrea Belluati*, Adrian Najer, Viviana Maffei, Claudio von Planta, Ioana Craciun, Cornelia G. Palivan*, Wolfgang Meier*, Multicompartment Polymer Vesicles with Artificial Organelles for Signal-Triggered Cascade Reactions Including Cytoskeleton Formation, Advanced Functional Materials, 2020, 2002949.*

8.1. Materials

All chemicals were purchased from Sigma Aldrich and were used without further purification, unless stated otherwise.

8.2. Polymer Synthesis

8.2.1. Synthesis of PMOXA₅-*b*-PDMS₅₈-*b*-PMOXA₅

The amphiphilic triblock copolymer poly(2-methyl-2-oxazoline)₅-*block*-poly(dimethylsiloxane)₅₈-*block*-poly(2-methyl-2-oxazoline)₅ (PMOXA₅-*b*-PDMS₅₈-*b*-PMOXA₅) was synthesized according to previously published protocols. ^[198]

Briefly, the hydroxyl-terminated PDMS (OH-PDMS-OH) was synthesized by acid-catalyzed polycondensation. After purification OH-PDMS-OH was reacted with trifluoromethanesulfonic acid in anhydrous hexane to form bitriflate-activated PDMS macroinitiator. Following filtration of the reaction mixture and evaporation of hexane, anhydrous ethyl acetate was added, in the presence of which the PDMS macroinitiator reacted with distilled 2-methyl-2-oxazoline (MOXA) in a symmetric cationic ring-opening polymerization. After quenching the reaction with TEA/water (1:4 v/v),

impurities were removed by ultrafiltration in water/EtOH (1:1 v/v). Finally, the solvent was removed by vacuum distillation and the resulting bihydroxyl-terminated triblock copolymer PMOXA₅-*b*-PDMS₅₈-*b*-PMOXA₅ was dried under vacuum.

The synthesis was performed by Sven Kasper.

8.2.2. Synthesis of PDMS₆₅-Heparin

PDMS₆₅-*block*-heparin (PDMS₆₅-*b*-Hep) was synthesized via reductive amination using a heparin length of 15 kDa.^[167] First, an ion exchange of heparin sodium salt to heparin tetrabutylammonium salt was achieved by Dowex Marathon MSC column chromatography followed by dialysis against water for 48 h using a dialysis membrane with a 3.5 – 5 kDa MWCO at room temperature (RT, 22°C). The dried tetrabutylammonium heparin salt was dissolved in dichloromethane (DCM) followed by the addition of 100-fold excess of PDMS and a 10-fold excess of 2-picoline borane. The mixture was stirred at RT for one week with the addition of a 10-fold excess of 2-picoline borane on day 3 and day 5. Subsequently, DCM was evaporated and the residue was rinsed with diethyl ether. The final product was dried under vacuum and dissolved in EtOH for further use.

8.2.3. Synthesis of PMOXA₈₈-*g*(SS)-PCL₂₃₈

The synthesis of the reduction sensitive graft copolymer PMOXA₈₈-*g*(SS)-PCL₂₃₈ (poly(2-methyl-2-oxazoline)₈₈-*graft*(SS)-poly(ϵ -caprolactone)₂₃₈) was performed according to a previously published method.^[170]

In short, the monomer ϵ -caprolactone and α -benzyl carboxylate- ϵ -caprolactone were copolymerized using EtOH as an initiator. Pyridyl disulfide functionalized poly(ϵ -caprolactone) PCL-co-PBCL was synthesized by varying molar ratios of the reaction partners in toluene at 110°C. PCL-co-PBCL was reduced by Pd/C at RT for 42 h under hydrogen to form PCL-co-PCCL. Then 2-pyridylthio cysteamine hydrochloride was added in the presence of N,N'-dicyclohexylcarbodiimid to form PCL-co-PPCL. Thiol-disulfide exchange reaction was performed, where PCL-co-PPCL and PMOXA-

SH were dissolved in DMF and a catalytic amount of acetic acid was continuously added to the mixture and stirred at RT under argon for three days. Finally, PMOXA₈₈-*g*(SS)-PCL₂₃₈ was purified by precipitation from cold MeOH and a white solid was obtained. ^[170]

Dr. Dalin Wu synthesized the polymer.

8.2.4. Synthesis of PMOXA₃₀-*b*-PCL₆₂

PMOXA-OH was dissolved in freshly distilled ϵ -caprolactone and then tin(II) 2-ethylhexanoate was added according to published protocols. The polymerization reaction was carried out at 110°C under argon for 30 min. Once the reaction mixture had cooled down to RT, PMOXA₃₀-*b*-PCL₆₂ (poly(2-methyl-2-oxazoline)₃₀-*block*-poly(ϵ -caprolactone)₆₂) was dissolved in DCM and the colorless solid was precipitated twice into diethyl ether.

Table 5. Polymer characteristics including name, block ratio, molecular weight and structure.

Polymer	Block Ratio	Mw(GPC) ^[199]	Polymeric Assemblies
PMOXA- <i>b</i> -PDMS- <i>b</i> -PMOXA	5-58-5	6662	Giant vesicles, polymersomes
PDMS- <i>b</i> -Hep	65-25	not determined	Micelles
PMOXA- <i>g</i> SS-PCL	88-238	22300	Reduction sensitive NP-Graft
PMOXA- <i>b</i> -PCL	30-62	9630	Non-reduction sensitive NP-Control

All polymers used in this work were fully characterized in previous publications. ^[167, 170]

The synthesis was performed by Dr. Dalin Wu.

8.2.5. PMOXA₆-*b*-PDMS₆₅-*b*-PMOXA₆

The copolymer PMOXA₆-PDMS₆₅-PMOXA₆ was purchased in Polymer Source Inc. The polymer was used either without any further purification steps or we functionalized it with PEG₄-N₃, according to the previously published protocol. ^[200] Commercially available PMOXA₆-PDMS₆₅-PMOXA₆-OH (200 mg, 0.034 mmol), was dissolved into 5 mL dry DMF, then succinic anhydride (16 mg, 0.16 mmol), 4-dimethylaminopyridine (15 mg, 0.12 mmol) and TEA (17 mg, 0.16 mmol) were added. The mixture was stirred for 24 h at 60°C. Finally, 180 mg colorless solid product was obtained after the ultrafiltration with a yield of 90%. The resulting PMOXA₈-PDMS₅₆-PMOXA₈-COOH

(100 mg, 0.011 mmol) was first dissolved in dry DMF, then 11-azido-3,6,9-trioxaundecan-1-amine (44 mg, 0.20 mmol), N, N'-dicyclohexylcarbodiimide (42 mg, 0.20 mmol) and 4-dimethylaminopyridine (1.2 mg, 0.01 mmol) were added into the above solution. The mixture was stirred for 24 h at RT. Finally, 86 mg colorless solid product was obtained with a yield of 86%. ¹H NMR (500 MHz, Chloroform-d) δ 3.24-3.72 ppm (m, 55H), 2.00-2.32 ppm (m, 32H), 0.40-0.58 ppm (m, 4H), 0.06 (m, 351H). IR: 2961, 2114, 1736, 1635, 1420, 1263, 1007, 787, 682 cm⁻¹.

The N₃-functionalization was performed by Dr. Viviana Maffei.

8.3. Preparation of Nanostructures

8.3.1. Bulk Rehydration Method

Bulk Rehydration Method

Ves5 and Ves25 polymersomes were prepared using the bulk rehydration method. First, 1 mL of PMOXA₅-*b*-PDMS₅₈-*b*-PMOXA₅ at 6 mg/mL in EtOH was mixed with 0.08 mL PDMS₆₅-*b*-Hep at 4 mg/mL in EtOH for Ves5 (5 wt% PDMS₆₅-*b*-Hep) or with 0.5 mL for Ves25 (25 wt% PDMS₆₅-*b*-Hep). A thin film of PMOXA₅-*b*-PDMS₅₈-*b*-PMOXA₅/ PDMS-*b*-Hep was formed by rotary evaporation of the EtOH (100 rpm at 40 °C, 100 mbar for 5 min and 7 mbar for 15min). The film was dried overnight under high vacuum (2 x 10⁻¹ mbar). For polymersome formation, the film was gently dislodged using a spatula and subsequently rehydrated in phosphate buffered saline (PBS) (1X, pH = 7.2, BioConcept) containing Oregon Green 488 carboxylic acid succinimidyl ester (OG488, 50 μ M, Thermo Fisher Scientific Inc.). Lipase adsorbed polymersomes (LipVes) were formed by adding lipase (4 mL, 0.2 mg/mL, 100 kU, from porcine pancreas, Sigma-Aldrich) to already formed PBS loaded polymersomes based on PMOXA₅-*b*-PDMS₅₈-*b*-PMOXA₅. For sodium loaded Ves5 (Na⁺Ves), the film was rehydrated in PBS (pH 7.2). Remaining non-adsorbed lipase was removed by size exclusion). Samples were stirred overnight at RT and then extruded 15 times through

a 100 nm Whatman Nuclepore filter. Size exclusion chromatography (SEC) was equilibrated to remove remaining non-encapsulated (dyes, salts) or non-adsorbed (lipase) cargo against PBS and for Na⁺Ves against HEPES (300 mM, pH 7.2). The polymersome fractions were collected and stored at 4°C. ^[167, 201]

M100 micelles were obtained by the bulk rehydration method. Films were formed from PDMS₆₅-*b*-Hep (100 wt%, M100) and rehydrated overnight in OG488 (50 μM) in PBS with stirring. ^[167] M100 were extruded 15 times through a 100 nm pore size Nuclepore membrane and purified by SEC equilibrated in PBS.

8.3.2. Solvent Switch Technique

Graft-nanoparticles (NP-Graft, reduction sensitive) were formed using a solvent switch technique. ^[170] For NP-Graft, graft copolymer PMOXA₈₈-*g*(SS)-PCL₂₃₈ (1 mg) was dissolved in DMF (300 μL) and Bodipy630/650 (1 mL, 1 μM) in PBS was added under continuous stirring. The resulting turbid mixture was dialyzed against NaCl (150 mM) for at least 48 hours with 5 changes of buffer. After a final dialysis against PBS (pH 7.2), NP-Graft were stored at 4°C.

Similarly, lipase substrate 1,2-Di-O-lauryl-rac-glycero-3-(glutaric acid 6-methylresorufin ester, Sigma-Aldrich) (DGGR, 52 μL, 2.5 mM) in 1:1 EtOH:DMSO were added to polymer (1 mg) in DMF (248 μL) to form DGGR loaded NP-Graft. For the assembly of gramicidin A loaded nanoparticles (gA loaded NP-Graft), gA (15 μL, 1 mM, from *Bacillus aneurinolyticus*) in DMSO were added to polymer (1 mg) in DMF (285 μL). Here, the gA loaded NP-Graft were dialyzed against HEPES. Non-encapsulated cargo (Bodipy630/650, DGGR, gA or IoNo) was removed from the NP-Graft solution by dialysis as described above. Based on previous results, we know that the reduction sensitive NP-Graft are stable in PBS and also in more complex environments, such as cell culture medium. ^[170]

As a control, we prepared non-reduction sensitive nanoparticles (NP-Control) prepared from the block copolymer PMOXA₃₀-*b*-PCL₆₂. PMOXA₃₀-*b*-PCL₆₂ (1 mg) dissolved in THF (300 μ L) and then Bodipy630/650 (1 mL, 1 μ M) in PBS was added dropwise. ^[170]

8.4. Preparation of Giant Polymersomes

Giant vesicles were prepared by spontaneous swelling in the absence of stirring also called film rehydration. PMOXA₅-*b*-PDMS₅₈-*b*-PMOXA₅ in EtOH (40 μ L, 6 mg/mL) or a mixture of PMOXA₅-*b*-PDMS₅₈-*b*-PMOXA₅ (40 μ L, 6 mg/mL) and PDMS₆₅-*b*-Hep in EtOH (5 μ L, 4 mg/mL; 8 wt%) were applied to a small glass vial or to a well of an 8-well microscopy chamber (Nunc Lab-TekChamber Slide System, Thermo Fisher Scientific). Films were formed by removing the EtOH in a vacuum chamber (Plasma Cleaner, PDC-002, Harrick Plasma) for one hour. To remove all traces of organic solvent, the glass vials and 8-well chambers were further dried in the desiccator under vacuum for at least 24 h. To produce giant vesicles, films were rehydrated in the dark with rehydration solution (200 μ L) overnight and stored at RT until further characterization. Rehydration solutions included different concentrations of sucrose, H₂O, and PBS. For long-term experiments (>48 h), NaN₃ (0.02%) was added to the rehydration solution to prevent bacterial and fungal growth, when enzymes were not involved.

8.5. Preparation of Multicompartmentments

For multicompartment assembly, films comprising PMOXA₅-*b*-PDMS₅₈-*b*-PMOXA₅ (40 μ L, 6 mg/mL) or a mixture of PMOXA₅-*b*-PDMS₅₈-*b*-PMOXA₅ (40 μ L, 6 mg/mL) and PDMS₆₅-*b*-Hep in EtOH (5 μ L, 4 mg/mL; 8 wt%) were rehydrated with sucrose solution (190 μ L, 300 mM) and the corresponding nanostructures (10 μ L) in PBS unless stated otherwise. For two-type multicompartmentments we typically used 10 μ L of each type nanostructures (in PBS) in 200 μ L of 300 mM sucrose solution, unless stated otherwise. We combined Bodipy630/650 loaded NP-Graft with OG488 loaded heparin

nanostructures (Ves5, Ves25, M100) to study their formation and selective stimuli-responsiveness. Additionally, we combined Bodipy630/650 loaded Ves5 with OG488 loaded Ves5. In general, film rehydration and storage of giant vesicles compartmentalized with fluorescent nanostructures were carried out at RT in the dark without stirring. To minimize the disruption of giant vesicles that would result in the formation of mostly nano-sized polymersomes, samples were always handled with great care (minimal agitation).

For the assembly of lipase containing multicompartments, we used lipase (40 μ L, 100 kU, from porcine pancreas, Sigma-Aldrich) (0.2 mg/mL) in PBS, DGGR loaded NP-Graft (20 μ L) in sucrose (300 mM, 180 μ L) as rehydration solution. To determine the loading efficiency of DGGR loaded NP-Graft and lipase, we tested 40 single GUVs and obtained the histogram along diagonal of fluorescence. Similarly, for the two-type multicompartment for enzymatic reaction, we added 30 μ L of lipase (0.1 mg ml⁻¹) adsorbed polymersomes (LipVes) in PBS and 20 μ L of DGGR loaded NP-Graft in 150 μ L of sucrose (300 mM) to the thin polymer film. Unadsorbed lipase was recovered via SEC and quantified at 280 nm with Nanodrop 2000 (ThermoFisher Inc.).

To obtain gA multicompartments that import sodium ions, we added gA loaded NP-Graft solution (30 μ L) to 270 μ L Asante Natrium Green 2 (ANG2, TEFlabs) solution (25 μ M in 300 mM sucrose) to the polymer film. Similarly, for two-type multicompartment to study ionophore recruitment, we loaded the GUVs with 30 μ L gA loaded NP-Graft, 30 μ L of sodium loaded Ves5 (Na⁺Ves) to 140 μ L ANG2 in 300 mM sucrose (25 μ M) as a rehydration solution.

The non-encapsulated nanostructures and ANG2 were removed from exterior solution by changing the supernatant with HEPES (300 mM, twice daily for 5 days). To determine the loading efficiency of gA loaded NP-Graft and ANG2, we tested 40 single GUVs and obtained the histogram along diagonal of fluorescence. For the gA multicompartments that export sodium ions, we added gA loaded NP-Grafts (30 μ L)

and in 1:1 PBS:300mM sucrose (270 μ L) to the polymer film. The gA loaded NP-Graft in GUVs sediment due to higher density (loaded sucrose) compared to the surrounding solution (300 mM HEPES). The non-encapsulated NP-Grafts, ANG2 or sodium ions were removed from the solution by several exchanges of the supernatant with HEPES buffer (300 mM, twice daily for 5 days) to avoid any influence from the surrounding solution.

8.6. Preparation of Actin GUVs

G-Actin loaded giant vesicles (Actin GUVs) were prepared by spontaneous swelling in the absence of stirring also called film rehydration. A mixture of PMOXA₅-PDMS₆₅-PMOXA₅ (60 μ L, 10 mg/mL, Polymer Source Inc.) in EtOH and N₃-functionalised PMOXA₅-PDMS₆₅-PMOXA₅ (0.3 μ L, 90 mg/mL) was applied to a glass vial. A thin polymer film was formed on the bottom of the vial by removing all traces of EtOH in a vacuum chamber (Plasma Cleaner, PDC-002, Harrick Plasma) for one hour. The films were rehydrated in the dark with the actin rehydration solution containing the monomeric protein G-actin (24 μ L, 1 mg/mL, Hypermol, rabbit alpha-actin skeletal muscle), ATTO488 labelled G-actin (ATTO488-actin, 2 μ L, 1 mg/mL, Hypermol, rabbit alpha-actin skeletal muscle), and the crosslinking agent filamin (4 μ L, 1 mg/mL, Hypermol, turkey smooth muscle, ~1:100 actin:filamin ratio, 92% purity) and sucrose (170 μ L, 300 mM, containing 0.02 % NaN₃) overnight in the fridge and stored for some days until further characterization.

G-actin, ATTO488- G-actin and filamin in solution (1 mg/mL) was stored for up to 1 week in ice in the fridge and non-solubilized G-actin at -80°C for long term storage.

8.7. Preparation of Actin MCs

For G-actin loaded multicompartments (Actin MCs) we prepared the sample similarly as for the formation of Actin GUVs. Instead of adding the pores to the surrounding

GUV solution, we rehydrated with the actin components (actin, ATTO488-actin, filamin) and in addition with pore-loaded NP-Graft (IoNo loaded NP-Graft or gA loaded NP-Graft, 20 μ L) and sucrose (300 mM). For 2-comp Actin MCs, we loaded 20 μ L SRBVes and 20 μ L IoNo loaded NP-Graft) and sucrose (300 mM).

8.8. Preparation of F-actin

F-actin was prepared in solution by adding monomeric protein G-actin (24 μ L, 1 mg/mL, Hypermol, rabbit alpha-actin skeletal muscle) and ATTO488-Actin (2 μ L, 1 mg/mL, Hypermol, rabbit alpha-actin skeletal muscle) with salt solutions (100 mM KCl, 70 mM MgCl₂, 70 mM CaCl₂) or for control with salt-free solution(300 mM HEPES, pH 7.2).

8.9. Fluorescence Imaging of Giant

Polymersomes and Multicompartmentments

Giant vesicles were imaged using an LSM 880 confocal laser scanning microscope (Carl Zeiss, Jena, Germany) with a water immersion objective (C-Apochromat, M=40, NA 1.2). The pinhole for each channel was set to 91 μ m and the MBS 488/561/633 filter was used. The transmission PMT (T-PMT) option was used to record bright field images. Imaging settings were kept constant for each experiment. Image processing was carried out with LSM Image Browser (Zeiss) and plot profile from ImageJ.

To mimic receptor-ligand interaction for the heparin moieties on the GUVs, we labeled the positively charged protamine sulfate (Grade X, from salmon, Sigma-Aldrich) with Oregon Green 488 succinimidyl ester (OG488-NHS, Invitrogen, 5-isomer). Protamine was dissolved in 500 μ L buffer containing 100 mM carbonate and 150 mM NaCl (500 μ L, pH 8.3, 10.2 mg/mL). OG488-NHS (0.5 mg) was dissolved in 50 μ L DMSO (1 μ M) and the solution was subsequently added to the protamine solution. The mixture was

incubated under shaking at RT for 4 h. The product was purified from free dye by fast protein liquid chromatography (FPLC Äkta Amersham Biosciences) with a Sephadex G25 column. We added OG488-labeled protamine (15 μ L) to the 8-well chamber containing giant vesicles solution (10 μ L) in PBS (225 μ L). After 24 h, samples were imaged by CLSM by using the 633 nm and 488 nm laser with pinhole 91 μ m and beam splitter MBS 488/561/633.

Protamine was labelled with Oregon Green 488 by Dr. Adrian Najer.

RZ loaded GUVS were characterized by CLSM using a 561 nm diode laser, beam splitter MBS 488/561 and pinhole of 34 μ m. The reducing agents were freshly prepared daily to assure the thiol-disulfide exchange capability.

For imaging of lipase (or LipVes) and DGGR loaded NP-Graft entrapped multicompartments, we added 30 μ L of these multicompartments in 232.5 μ L PBS with DTT (30 μ L, 100 mM) or PBS (262.5 μ L) for the controls. Additionally, we added Orlistat (7.5 μ L, 2.5 mM) to the 8-well chambers to assure the inactivation of non-encapsulated lipase or LipVes outside of the giant vesicles. The activity in giant vesicles after 2, 24 and 48 hours of incubation in presence of DTT was assayed via CLSM, exciting at 561 nm using beam splitter MBS 488/561 and pinhole of 44 μ m.

To study the induced incorporation of gA for the import of sodium ions into the giant vesicles, we added gA loaded NP-Graft and ANG2 entrapped multicompartments (20 μ L) in PBS (250 μ L) and DTT (30 μ L, 100 mM) in PBS or HEPES buffer for the controls to the 8-well. For studying of the export of sodium ions through the gA pores, we added gA loaded NP-Graft (20 μ L) and sodium ions entrapped multicompartments, ANG2 (20 μ L, 100 μ M) in HEPES (300 mM), HEPES (50 μ L, 300 mM) and DTT (10 μ L, 100 mM) in HEPES (300 mM) or HEPES (300 mM) for the control to the observation chamber. For the two-type multicompartments, Na⁺Ves, gA loaded NP-Graft and ANG2 co-loaded into giant vesicles, where these multicompartments (20 μ L) were added to DTT (20 μ L, 100 mM) and HEPES (160 μ L, 300 mM, pH 7.2) or in

HEPES (180 μ L, 300 mM, pH 7.2) for the controls to the 8-well observation chamber. A 488 nm diode laser, beam splitter MBS 488 and a pinhole of 40 μ m was used.

For Actin GUV CLSM imaging we used a 488 nm diode laser for actin filaments and a 633 nm for Bodipy630/650 adsorbed GUV membrane. To induce actin polymerization within the polymeric GUVs, we added Actin GUVs (30 μ L) with salt/pore solutions (i) KCl (250 μ L, 200 mM) and gA (2 μ L, 1 mM), (ii) MgCl₂ (250 μ L, 150 mM) and IoNo (2 μ L, 1.3 mM) and (iii) CaCl₂ (250 μ L, 150 mM) and IoNo (2 μ L, 1.3 mM). As a control we used salt-free HEPES (250 μ L, 300 mM, pH 7.2) with or without pores (2 μ L). For inducing actin polymerization in multicompartments, we added Actin MCs (20 μ L) in corresponding salt solution (250 μ L) and DTT (30 μ L, 100 mM) and as the control we used HEPES (300 mM, pH 7.2). Here, no pores were added additionally to the surrounding giant solution. By summing up several confocal fluorescence images along the z-axis in the equatorial plane (x-y plane), we could extract z-stack projections of Actin GUVs/MCs with filaments out-of-plane. For the compartmentalized actin samples, we added Bodipy630/650 (10 μ L, 72 μ M) to each well of the observation chamber to visualize the GUV membrane.

8.10. Fluorescence Correlation Spectroscopy

Fluorescence correlation spectroscopy (FCS) experiments were carried out with an inverted laser scanning confocal microscope (LSM 880 and LSM 510-META/Confocor2, Carl Zeiss) using a water immersion objective (Zeiss C/Apochromat, M=40, NA=1.2). A helium/neon laser (wavelength 633 nm) and an Argon laser (wavelength 488 nm) with appropriate filters (MBS 488/56/633 for 633 nm laser; MBS 488 for 488 nm laser) were used. The fluorescence intensity was recorded on an avalanche photodiode. The pinhole size (19 μ m for 633 nm laser and 45 μ m for 488 nm laser, 1AU) was adjusted before recording FCS curves of the respective free dye.

For FCS measurements of fluorophores or nanostructures in solution, 5 μL of a sample was placed on a 0.15 mm thick glass coverslip mounted on the microscope stage. Alternatively, giant vesicles were measured in 8-well chambers (Nunc Lab-Tek Chamber Slide System, Thermo Fisher Scientific) microscopy chambers. For reduction-triggered rupture experiments, Bodipy630/650 -loaded NP-Grafts or NP-Control were added to DTT (200 μL , 10 mM) in PBS or to GSH (200 μL , 10 mM) in Phosphate buffer (0.1 M) containing NaCl (50 mM, pH 7). For the calibration of the confocal volume, the diffusion constants of the nanostructures and the free dye were used. Free fluorophores were measured for 5 s at RT with 30 measurements recorded, whereas dye loaded nanostructures were measured for 10 s with 10 repeats. Typically, 80% of the FCS curves were suitable and included in the analysis. The experimental autocorrelation curves were fitted according to the following equation for samples with one component diffusion model:

$$G(\tau) = 1 + \frac{1}{N} \left[\frac{1}{1 + \frac{\tau}{\tau_D}} \frac{1}{\sqrt{1 + R^2 \frac{\tau}{\tau_D}}} \right] \quad (14)$$

Where N represents the average number of particles in the observation volume, τ_D is the diffusional correlation time, and R is the structural parameter which was set to 5. In the next equation, the diffusion coefficient D was calculated using the relation between τ_D and the x-y dimension of the confocal volume (ω_{xy}).

$$\tau = \frac{\omega_{xy}^2}{4D} \quad (15)$$

The Einstein-Stokes equation using the diffusion coefficient D , the Boltzmann's constant k_B , absolute temperature T , viscosity of the surrounding medium η was used to calculate the hydrodynamic radius (R_H) of the nanostructures.

$$D = \frac{k_B T}{6\pi\eta R_H} \quad (16)$$

Multicompartmental structures were located in microscopy chambers in the bright field imaging mode of the CLSM and a focus in the center of a giant vesicle was marked. Due to

higher density (encapsulated sucrose) compared to the outer solution (buffer), the giant vesicles sank to the bottom of the observation chamber. This allowed us to first identify the center of the giant vesicles by bright field imaging and positioning of the confocal volume accordingly, followed by FCS measurement to obtain the corresponding diffusion times. Subsequently, ten times 10 s were recorded at RT for each FCS measurement cycle per multicompartment. After the recordings were normalized and fitted. For the analysis, a customized python script (available on request) was applied to meet the following criteria: If the counts per molecule (CPM) were below 2 kHz, the N was set to 0. Additionally, membrane measurements with diffusion times > 10 ms were excluded. Only measurements in the lumen of the giant vesicles, to detect the subcompartments were targeted. Giant vesicles that were moving out of focus during the measurements were also excluded from the analysis. Processing was the same for individual FCS/CLSM measurements. Diffusion time count rate (CR), CPM, numbers of particles, and hydrodynamic diameter from individual FCS measurements were averaged. The data extracted from the FCS data (N , CR) were presented as average \pm standard error of mean (SEM) from 40 measurements that were based on at least three independent samples for each type of multicompartment, except the time point at 8 h that was from 5 measurements. Data were statistically analyzed by one-way ANOVA (analysis of variance) using a customized python script (available on request). Additionally, HSD (honestly significant difference procedure) test for comparing differences between multiple groups was run if significant differences was found ($p < 0.05$).

Our giant vesicles form hemispheres immobilized on the bottom of the hydrophilic plasma treated 8-well chambers due to hydrophilic forces. The sucrose-filled giant vesicles sink to the surface in a non-sucrose containing solution (PBS; 0.1 M Phosphate buffer (+ 50 mM NaCl, pH 7) or 300 mM HEPES). The mean number of particles in the giant hemisphere (GHN) volume was estimated using following equation based on

the measured number of particles in the confocal volume (CN), the volume of the confocal volume (CV) and the volume of the giant hemisphere (GHV):

$$GHN = \frac{GHV}{CV} CN \quad (17)$$

GHV was calculated by measuring each diameter of the giant hemisphere from CLSM images with ImageJ. The confocal volume (CV) was assumed to be 1 fL ^[202] and the number of particles in the confocal volume (CN) extracted from FCS measurements were used to estimate the mean number of the NP-Graft in the giant hemisphere in the presence of 10 mM DTT (0-48 h).

To study the stimuli responsiveness, the FCS curves of the NP-Graft in giant vesicles with reducing agent (DTT or GSH, 10 mM) or under physiological conditions over time were analyzed. When sigmoidal curves of subcompartments were similar to sigmoidal curves of free nanoassemblies, we assumed successful formation of intact multicompartments. Additionally, if inside the observation volume the average number of particles N was 0, it was assumed that the previous intact multicompartment was not a multicompartment anymore and the inner compartments burst within the giant vesicle. Similarly, we studied the formation and selective disassembly of two-type multicompartments. Here, we measured FCS of both subcompartments within the same GUV with corresponding channels. Successful formation of intact two-type multicompartment were assumed, when each of the sigmoidal curves of subcompartments in the GUV were similar to the sigmoidal curves of corresponding nanoassemblies in solution. To study reduction responsiveness, we prepared the responsive two-type multicompartment solution in DTT in PBS (10 mM) as a stimulus to selectively disassemble the stimuli sensitive subcompartment and as a control under physiological conditions.

For Actin-MCs, we co-loaded giant polymersomes with SRB loaded polymersome and IoNo loaded NP-Graft. After 24 h incubation of DTT or HEPES for control we

measured FCS using a 561 laser (wavelength 561 nm, 1 AU) utilizing a beam splitter of MBS 488/561 to study the viscosity changes.

8.11. Transmission Electron Microscopy

Nanostructures (5 μ L) were adsorbed on copper grids for 1 min, washed with water, and blotted to remove excess liquid. Specimens were negatively stained with uranyl acetate (2%) for 15 sec, washed and blotted. Transmission Electron Microscopy (TEM) micrographs were recorded on a Philips CM100 with an accelerating voltage of 80 kV.

TEM imaging was performed by Gabriele Persy and me.

8.12. Cryonic Transmission Electron

Microscopy

A 4 μ l aliquot of sample on extruded GUVs through a 400 nm Whatman Nuclepore filter was adsorbed onto holey carbon-coated grid (Lacey, Ted Pella, USA), blotted with Whatman 1 filter paper and vitrified into liquid ethane at -178 °C using a Leica GP plunger (Leica, Austria). Frozen grids were transferred onto a Talos electron microscope (FEI, USA) using a Gatan 626 cryo-holder. Electron micrographs were recorded at an accelerating voltage of 200 kV and a nominal magnification of 57000 x, using a low-dose system (20 e-/Å²) and keeping the sample at low temperature. Micrographs were recorded on a CETA camera.

Cryonic TEM imaging was performed by Carola Alampi.

8.13. Dynamic Light Scattering

The size of the nanostructures was characterized by dynamic light scattering (DLS) using a Zetasizer Nano ZSP (Malvern Instruments Ltd.). A laser wavelength of 633 nm and a scattering angle of 173° were used.

8.14. Enzymatic Test

Enzymatic fluorescence assays were performed using a Spectramax M5 microplate reader (Molecular Devices), in a black flat-bottomed 96- well plate (Thermo Fisher Scientific), final volume in either PBS (200 μ L) or sucrose (200 μ L, 300 mM). The increase of fluorescence (ex: 529 nm, em: 600 nm) was monitored for 20 minutes at RT and measured in triplicate. With respect to the experiment, lipase was added to a final concentration of 10 μ g/mL, DGGR (25 μ M), DTT (10 mM), Orlistat (655 μ M) and the DGGR loaded NP-Graft (10 μ L) suspension were added.

8.15. Pyrene-F-actin Polymerization Assays

For pyrene-F-actin (10%, Hypermol, rabbit alpha-actin skeletal muscle, 99% purity) in 100 mM of the salts solutions (KCl, MgCl₂, CaCl₂) and as a control in salt-free HEPES (300 mM, pH 7.2) were added to 300 mM sucrose (final volume 200 μ L), in a black flat-bottomed 96-well plate (Thermo Fisher Scientific). The measurements were carried out with a SpectraMax M5e microplate reader (Molecular Devices), followed for 90 minutes. Ex/Em 365/407 nm.

8.16. Preparation of Actin GUVs for 3D-SIM

Actin GUVs (15 μ L), IoNo (2 μ L, 1.3 mM) and MgCl₂ or CaCl₂ (275 μ L, 150 mM) were added each in a well of a sterile observation chambers (μ -Slide 8 Well Glass Bottom, #1.5H, Ibidi). In addition, Actin GUVs (15 μ L), gA (2 μ L, 1 mM), and KCl (275 μ L, 200 mM) were added to a well. All salt solutions contained NaN₃ (0.02%) and the sample was incubated for 48 h in the fridge for the actin polymerization.

8.17. 3D-SIM Super-Resolution Microscopy

Three-dimensional structured illumination microscopy (3D-SIM) was performed on a DeltaVision OMX-Blaze V4 system (GE Healthcare) equipped with 405, 445, 488, 514, 568 and 642 nm solid-state lasers. Images were acquired using a Plan Apo N 60x, 1.42 NA oil immersion objective lens (Olympus) and 4 liquid-cooled sCMOS cameras (pco.edge 5.5, full frame 2560 x 2160; PCO). Exciting light was directed through a movable optical grating to generate a fine-striped interference pattern on the sample plane. The pattern was shifted laterally through five phases and three angular rotations of 60° for each z section. The 488 nm laser line was used, and the optical z-sections were separated by 0.125 μm . Laser power was attenuated to 50% with an exposure of 20 milliseconds.

Raw 3D-SIM images were processed and reconstructed using the DeltaVision OMX SoftWoRx software package (v6.1.3, GE Healthcare). The resulting size of the reconstructed images was of 512 x 512 pixels from an initial set of 256 x 256 raw images. The channels were aligned in the image plane and around the optical axis using predetermined shifts as measured using a target lens and the SoftWoRx alignment tool.

Imaging was performed by Dr. Alexia Loynton-Ferrand.

9. References

- [1] Thamboo, S.; Najer, A.; Belluati, A.; von Planta, C.; Wu, D. L.; Craciun, I.; Meier, W.; Palivan, C. C., Mimicking Cellular Signaling Pathways within Synthetic Multicompartment Vesicles with Triggered Enzyme Activity and Induced Ion Channel Recruitment. *Adv Funct Mater* **2019**.
- [2] Elani, Y.; Law, R. V.; Ces, O., Vesicle-based artificial cells: recent developments and prospects for drug delivery. *Ther Deliv* **2015**, *6* (5), 541-3.
- [3] Walde, P., Building artificial cells and protocell models: Experimental approaches with lipid vesicles. *Bioessays* **2010**, *32* (4), 296-303.
- [4] McMahon, H. T.; Gallop, J. L., Membrane curvature and mechanisms of dynamic cell membrane remodelling. *Nature* **2005**, *438* (7068), 590-596.
- [5] van Meer, G.; Voelker, D. R.; Feigenson, G. W., Membrane lipids: where they are and how they behave. *Nat Rev Mol Cell Bio* **2008**, *9* (2), 112-124.
- [6] Supramaniam, P.; Ces, O.; Salehi-Reyhani, A., Microfluidics for Artificial Life: Techniques for Bottom-Up Synthetic Biology. *Micromachines-Basel* **2019**, *10* (5).
- [7] Keating, C. D., Aqueous Phase Separation as a Possible Route to Compartmentalization of Biological Molecules. *Accounts Chem Res* **2012**, *45* (12), 2114-2124.
- [8] Gupta, A., Comprehensive biochemistry for dentistry : textbook for dental students. **2019**.
- [9] Hovland, R.; Hesketh, J. E.; Pryme, I. F., The compartmentalization of protein synthesis: Importance of cytoskeleton and role in mRNA targeting. *Int J Biochem Cell B* **1996**, *28* (10), 1089-1105.
- [10] Asokan, A.; Cho, M. J., Exploitation of intracellular pH gradients in the cellular delivery of macromolecules. *J Pharm Sci* **2002**, *91* (4), 903-913.
- [11] Chandrawati, R.; van Koeverden, M. P.; Lomas, H.; Caruso, F., Multicompartment Particle Assemblies for Bioinspired Encapsulated Reactions. *J Phys Chem Lett* **2011**, *2* (20), 2639-2649.
- [12] Zecchin, A.; Stapor, P. C.; Goveia, J.; Carmeliet, P., Metabolic pathway compartmentalization: an underappreciated opportunity? *Curr Opin Biotech* **2015**, *34*, 73-81.
- [13] Cornejo, E.; Abreu, N.; Komeili, A., Compartmentalization and organelle formation in bacteria. *Curr Opin Cell Biol* **2014**, *26*, 132-138.
- [14] Masters, C., On the role of the cytoskeleton in metabolic compartmentation. **1995**, *2*.

- [15] Mulla, Y.; Aufderhorst-Roberts, A.; Koenderink, G. H., Shaping up synthetic cells. *Phys Biol* **2018**, *15* (4).
- [16] Mair, J.; Puschendorf, B.; Michel, G., Clinical-Significance of Cardiac Contractile Proteins for the Diagnosis of Myocardial Injury. *Adv Clin Chem* **1994**, *31*, 63-98.
- [17] Maruyama, K.; Tsukagoshi, K., Effects of Kcl, Mgcl₂, and Cacl₂ Concentrations on the Monomer-Polymer Equilibrium of Actin in the Presence and Absence of Cytochalasin-D. *J Biochem-Tokyo* **1984**, *96* (3), 605-611.
- [18] Chhabra, E. S.; Higgs, H. N., The many faces of actin: Matching assembly factors with cellular structures. *Nat Cell Biol* **2007**, *9* (10), 1110-1121.
- [19] Kang, H.; Bradley, Michael J.; Elam, W. A.; De La Cruz, Enrique M., Regulation of Actin by Ion-Linked Equilibria. *Biophys J* **2013**, *105* (12), 2621-2628.
- [20] Staiger, C. J., Signaling to the actin cytoskeleton in plants. *Annu Rev Plant Phys* **2000**, *51*, 257-288.
- [21] Septiadi, D.; Abdussalam, W.; Rodriguez-Lorenzo, L.; Spuch-Calvar, M.; Bourquin, J.; Petri-Fink, A.; Rothen-Rutishauser, B., Revealing the Role of Epithelial Mechanics and Macrophage Clearance during Pulmonary Epithelial Injury Recovery in the Presence of Carbon Nanotubes. *Adv Mater* **2018**, *30* (52).
- [22] Kang, H.; Bradley, M. J.; McCullough, B. R.; Pierre, A.; Grintsevich, E. E.; Reisler, E.; De La Cruz, E. M., Identification of cation-binding sites on actin that drive polymerization and modulate bending stiffness. *Proc Natl Acad Sci U S A* **2012**, *109* (42), 16923-7.
- [23] Abu Shah, E.; Keren, K., Symmetry breaking in reconstituted actin cortices. *Elife* **2014**, *3*.
- [24] Sutherland-Smith, A. J., Filamin structure, function and mechanics: are altered filamin-mediated force responses associated with human disease? *Biophys Rev* **2011**, *3* (1), 15-23.
- [25] Nakamura, F.; Stossel, T. P.; Hartwig, J. H., The filamins Organizers of cell structure and function. *Cell Adhes Migr* **2011**, *5* (2), 160-169.
- [26] Mazzochi, C.; Benos, D. J.; Smith, P. R., Interaction of epithelial ion channels with the actin-based cytoskeleton. *Am J Physiol-Renal* **2006**, *291* (6), F1113-F1122.
- [27] Maguire, G.; Connaughton, V.; Prat, A. G.; Jackson, G. R.; Cantiello, H. F., Actin cytoskeleton regulates ion channel activity in retinal neurons. *Neuroreport* **1998**, *9* (4), 665-670.
- [28] Kamat, N. P.; Katz, J. S.; Hammer, D. A., Engineering Polymersome Protocells. *J Phys Chem Lett* **2011**, *2* (13), 1612-1623.
- [29] Martino, C.; deMello, A. J., Droplet-based microfluidics for artificial cell generation: a brief review. *Interface Focus* **2016**, *6* (4).

- [30] Xu, C.; Hu, S.; Chen, X. Y., Artificial cells: from basic science to applications. *Mater Today* **2016**, *19* (9), 516-532.
- [31] Spoelstra, W. K.; Deshpande, S.; Dekker, C., Tailoring the appearance: what will synthetic cells look like? *Curr Opin Biotech* **2018**, *51*, 47-56.
- [32] Palivan, C. G.; Goers, R.; Najer, A.; Zhang, X. Y.; Car, A.; Meier, W., Bioinspired polymer vesicles and membranes for biological and medical applications. *Chem Soc Rev* **2016**, *45* (2), 377-411.
- [33] Garni, M.; Thamboo, S.; Schoenenberger, C. A.; Palivan, C. G., Biopores/membrane proteins in synthetic polymer membranes. *Biochim Biophys Acta Biomembr* **2017**, *1859* (4), 619-638.
- [34] Belluati, A.; Craciun, I.; Meyer, C. E.; Rigo, S.; Palivan, C. G., Enzymatic reactions in polymeric compartments: nanotechnology meets nature. *Curr Opin Biotechnol* **2019**, *60*, 53-62.
- [35] Coelho, J. F.; Ferreira, P. C.; Alves, P.; Cordeiro, R.; Fonseca, A. C.; Góis, J. R.; Gil, M. H., Drug delivery systems: Advanced technologies potentially applicable in personalized treatments. *EPMA Journal* **2010**, *1* (1), 164-209.
- [36] Findenegg, G. H., J. N. Israelachvili: Intermolecular and Surface Forces (With Applications to Colloidal and Biological Systems). Academic Press, London, Orlando, San Diego, New York, Toronto, Montreal, Sydney, Tokyo 1985. 296 Seiten, Preis: \$ 65.00. *Berichte der Bunsengesellschaft für physikalische Chemie* **1986**, *90* (12), 1241-1242.
- [37] Zhang, X. Y.; Zhang, P. Y., Polymersomes in Nanomedicine - A Review. *Curr Nanosci* **2017**, *13* (2), 124-129.
- [38] Abedalwafa, M.; Wang, F. J.; Wang, L.; Li, C. J., Biodegradable Poly-Epsilon-Caprolactone (Pcl) for Tissue Engineering Applications: A Review. *Rev Adv Mater Sci* **2013**, *34* (2), 123-140.
- [39] Christian, D. A.; Garbuzenko, O. B.; Minko, T.; Discher, D. E., Polymer Vesicles with a Red Cell-like Surface Charge: Microvascular Imaging and in vivo Tracking with Near-Infrared Fluorescence. *Macromol Rapid Comm* **2010**, *31* (2), 135-141.
- [40] Mecke, A.; Dittrich, C.; Meier, W., Biomimetic membranes designed from amphiphilic block copolymers. *Soft Matter* **2006**, *2* (9), 751-759.
- [41] Antonietti, M.; Forster, S., Vesicles and liposomes: A self-assembly principle beyond lipids. *Adv Mater* **2003**, *15* (16), 1323-1333.
- [42] Blanazs, A.; Armes, S. P.; Ryan, A. J., Self-Assembled Block Copolymer Aggregates: From Micelles to Vesicles and their Biological Applications. *Macromol Rapid Comm* **2009**, *30* (4-5), 267-277.
- [43] Discher, D. E.; Ahmed, F., Polymersomes. *Annu Rev Biomed Eng* **2006**, *8*, 323-

- [44] Balazs, D. A.; Godbey, W., Liposomes for Use in Gene Delivery. *Journal of Drug Delivery* **2011**, *2011*.
- [45] Kita-Tokarczyk, K.; Grumelard, J.; Haefele, T.; Meier, W., Block copolymer vesicles - using concepts from polymer chemistry to mimic biomembranes. *Polymer* **2005**, *46* (11), 3540-3563.
- [46] Forster, S.; Plantenberg, T., From self-organizing polymers to nanohybrid and biomaterials. *Angew Chem Int Ed Engl* **2002**, *41* (5), 689-714.
- [47] Vanden Bout, D. A., Self-Assembled Nanostructures *J Am Chem Soc* **2003**, *125* (31), 9539-9539.
- [48] Tanford, C., Hydrophobic Effect and Organization of Living Matter. *Science* **1978**, *200* (4345), 1012-1018.
- [49] Ruckenstein, E.; Nagarajan, R., Critical Micelle Concentration - Transition Point for Micellar Size Distribution. *J Phys Chem-Us* **1975**, *79* (24), 2622-2626.
- [50] Wong, C. K.; Stenzel, M. H.; Thordarson, P., Non-spherical polymersomes: formation and characterization. *Chem Soc Rev* **2019**, *48* (15), 4019-4035.
- [51] Bangham, A. D.; Horne, R. W., Negative Staining of Phospholipids + Their Structural Modification by-Surface Active Agents as Observed in Electron Microscope. *J Mol Biol* **1964**, *8* (5), 660-&.
- [52] Malmstadt, N.; Jeon, L. J.; Schmidt, J. J., Long-lived planar lipid bilayer membranes anchored to an in situ polymerized hydrogel. *Adv Mater* **2008**, *20* (1), 84+.
- [53] Fahey, P. F.; Koppel, D. E.; Barak, L. S.; Wolf, D. E.; Elson, E. L.; Webb, W. W., Lateral Diffusion in Planar Lipid Bilayers. *Science* **1977**, *195* (4275), 305-306.
- [54] Rideau, E.; Wurm, F. R.; Landfester, K., Giant polymersomes from non-assisted film hydration of phosphate-based block copolymers. *Polym Chem-Uk* **2018**, *9* (44), 5385-5394.
- [55] Greene, A. C.; Henderson, I. M.; Gomez, A.; Paxton, W. F.; VanDelinder, V.; Bachand, G. D., The Role of Membrane Fluidization in the Gel-Assisted Formation of Giant Polymersomes. *Plos One* **2016**, *11* (7).
- [56] Henriksen-Lacey, M.; Korsholm, K. S.; Andersen, P.; Perrie, Y.; Christensen, D., Liposomal vaccine delivery systems. *Expert Opin Drug Del* **2011**, *8* (4), 505-519.
- [57] Onaca, O.; Enea, R.; Hughes, D. W.; Meier, W., Stimuli-Responsive Polymersomes as Nanocarriers for Drug and Gene Delivery. *Macromol Biosci* **2009**, *9* (2), 129-139.
- [58] Discher, D. E.; Ortiz, V.; Srinivas, G.; Klein, M. L.; Kim, Y.; David, C. A.;

- Cai, S. S.; Photos, P.; Ahmed, F., Emerging applications of polymersomes in delivery: From molecular dynamics to shrinkage of tumors. *Prog Polym Sci* **2007**, *32* (8-9), 838-857.
- [59] Hammer, D. A.; Kamat, N. P., Towards an artificial cell. *Febs Lett* **2012**, *586* (18), 2882-2890.
- [60] Messenger, L.; Gaitzsch, J.; Chierico, L.; Battaglia, G., Novel aspects of encapsulation and delivery using polymersomes. *Curr Opin Pharmacol* **2014**, *18*, 104-111.
- [61] Gopfrich, K.; Platzman, I.; Spatz, J. P., Mastering Complexity: Towards Bottom-up Construction of Multifunctional Eukaryotic Synthetic Cells. *Trends Biotechnol* **2018**, *36* (9), 938-951.
- [62] Rideau, E.; Dimova, R.; Schwille, P.; Wurm, F. R.; Landfester, K., Liposomes and polymersomes: a comparative review towards cell mimicking. *Chem Soc Rev* **2018**, *47* (23).
- [63] Nishiyama, N., Nanomedicine - Nanocarriers shape up for long life. *Nat Nanotechnol* **2007**, *2* (4), 203-204.
- [64] Hunter, D. G.; Frisken, B. J., Effect of extrusion pressure and lipid properties on the size and polydispersity of lipid vesicles. *Biophys J* **1998**, *74* (6), 2996-3002.
- [65] Kamiya, K.; Takeuchi, S., Giant liposome formation toward the synthesis of well-defined artificial cells. *J Mater Chem B* **2017**, *5* (30), 5911-5923.
- [66] Reeves, J. P.; Dowben, R. M., Formation and Properties of Thin-Walled Phospholipid Vesicles. *J Cell Physiol* **1969**, *73* (1), 49-&.
- [67] Fetsch, C.; Gaitzsch, J.; Messenger, L.; Battaglia, G.; Luxenhofer, R., Self-Assembly of Amphiphilic Block Copolypeptoids - Micelles, Worms and Polymersomes (vol 6, 33491, 2016). *Sci Rep-Uk* **2016**, *6*.
- [68] Angelova, M. I.; Dimitrov, D. S., Liposome Electroformation. *Faraday Discuss* **1986**, *81*, 303-+.
- [69] Montes, L. R.; Alonso, A.; Goni, F. M.; Bagatolli, L. A., Giant unilamellar vesicles electroformed from native membranes and organic lipid mixtures under physiological conditions. *Biophys J* **2007**, *93* (10), 3548-3554.
- [70] Witkowska, A.; Jablonski, L.; Jahn, R., A convenient protocol for generating giant unilamellar vesicles containing SNARE proteins using electroformation. *Sci Rep-Uk* **2018**, *8*.
- [71] Horger, K. S.; Estes, D. J.; Capone, R.; Mayer, M., Films of Agarose Enable Rapid Formation of Giant Liposomes in Solutions of Physiologic Ionic Strength. *J Am Chem Soc* **2009**, *131* (5), 1810-1819.
- [72] Lira, R. B.; Dimova, R.; Riske, K. A., Giant Unilamellar Vesicles Formed by

- Hybrid Films of Agarose and Lipids Display Altered Mechanical Properties. *Biophys J* **2014**, *107* (7), 1609-1619.
- [73] Weinberger, A.; Tsai, F. C.; Koenderink, G. H.; Schmidt, T. F.; Itri, R.; Meier, W.; Schmatko, T.; Schroder, A.; Marques, C., Gel-Assisted Formation of Giant Unilamellar Vesicles. *Biophys J* **2013**, *105* (1), 154-164.
- [74] Mora, N. L.; Hansen, J. S.; Gao, Y.; Ronald, A. A.; Kieltyka, R.; Malmstadt, N.; Kros, A., Preparation of size tunable giant vesicles from cross-linked dextran(ethylene glycol) hydrogels. *Chem Commun* **2014**, *50* (16), 1953-1955.
- [75] Pautot, S.; Frisken, B. J.; Weitz, D. A., Production of unilamellar vesicles using an inverted emulsion. *Langmuir* **2003**, *19* (7), 2870-2879.
- [76] Campillo, C.; Sens, P.; Koster, D.; Pontani, L. L.; Levy, D.; Bassereau, P.; Nassoy, P.; Sykes, C., Unexpected Membrane Dynamics Unveiled by Membrane Nanotube Extrusion. *Biophys J* **2013**, *104* (6), 1248-1256.
- [77] Stuart, M. A. C.; Huck, W. T. S.; Genzer, J.; Muller, M.; Ober, C.; Stamm, M.; Sukhorukov, G. B.; Szleifer, I.; Tsukruk, V. V.; Urban, M.; Winnik, F.; Zauscher, S.; Luzinov, I.; Minko, S., Emerging applications of stimuli-responsive polymer materials. *Nat Mater* **2010**, *9* (2), 101-113.
- [78] Wei, M. L.; Gao, Y. F.; Li, X.; Serpe, M. J., Stimuli-responsive polymers and their applications. *Polym Chem-Uk* **2017**, *8* (1), 127-143.
- [79] Jahid, M. A.; Hu, J.; Zhuo, H., Stimuli-responsive polymers in coating and laminating for functional textile. 2019; pp 155-173.
- [80] Bixner, O.; Kurzhals, S.; Virk, M.; Reimhult, E., Triggered Release from Thermoresponsive Polymersomes with Superparamagnetic Membranes. *Materials* **2016**, *9* (1).
- [81] Kim, K. T.; Cornelissen, J. J. L. M.; Nolte, R. J. M.; van Hest, J. C. M., A Polymersome Nanoreactor with Controllable Permeability Induced by Stimuli-Responsive Block Copolymers. *Adv Mater* **2009**, *21* (27), 2787-+.
- [82] Mabrouk, E.; Cuvelier, D.; Brochard-Wyart, F.; Nassoy, P.; Li, M. H., Bursting of sensitive polymersomes induced by curling. *P Natl Acad Sci USA* **2009**, *106* (18), 7294-7298.
- [83] DiazDuarte-Rodriguez, M.; Cortez-Lemus, N. A.; Licea-Claverie, A.; Licea-Rodriguez, J.; Mendez, E. R., Dual Responsive Polymersomes for Gold Nanorod and Doxorubicin Encapsulation: Nanomaterials with Potential Use as Smart Drug Delivery Systems. *Polymers-Basel* **2019**, *11* (6).
- [84] Cerritelli, S.; Velluto, D.; Hubbell, J. A., PEG-SS-PPS: Reduction-sensitive disulfide block copolymer vesicles for intracellular drug delivery. *Biomacromolecules* **2007**, *8* (6), 1966-1972.

- [85] Lichtman, J. W.; Conchello, J. A., Fluorescence microscopy. *Nat Methods* **2005**, *2* (12), 910-919.
- [86] Bacia, K.; Kim, S. A.; Schwille, P., Fluorescence cross-correlation spectroscopy in living cells. *Nat Methods* **2006**, *3* (2), 83-89.
- [87] Butterworth, P. J., Lehninger: principles of biochemistry (4th edn) D. L. Nelson and M. C. Cox, W. H. Freeman & Co., New York, 1119 pp (plus 17 pp glossary), ISBN 0-7167-4339-6 (2004). *Cell Biochem Funct* **2005**, *23* (4), 293-294.
- [88] Elson, E. L., Fluorescence Correlation Spectroscopy: Past, Present, Future. *Biophys J* **2011**, *101* (12), 2855-2870.
- [89] Engelborghs, Y.; Visser, A. J. W. G., Fluorescence Spectroscopy and Microscopy Methods and Protocols Preface. *Fluorescence Spectroscopy and Microscopy: Methods and Protocols* **2014**, *1076*, V-Xii.
- [90] Trantidou, T.; Friddin, M.; Elani, Y.; Brooks, N. J.; Law, R. V.; Seddon, J. M.; Ces, O., Engineering Compartmentalized Biomimetic Micro- and Nanocontainers. *Acs Nano* **2017**, *11* (7), 6549-6565.
- [91] Yewdall, N. A.; Mason, A. F.; van Hest, J. C. M., The hallmarks of living systems: towards creating artificial cells. *Interface Focus* **2018**, *8* (5).
- [92] Jia, H.; Schwille, P., Bottom-up synthetic biology: reconstitution in space and time. *Curr Opin Biotechnol* **2019**, *60*, 179-187.
- [93] Postupalenko, V.; Einfalt, T.; Lomora, M.; Dinu, I. A.; Palivan, C. G., Chapter 11 - Bionanoreactors: From Confined Reaction Spaces to Artificial Organelles. In *Organic Nanoreactors*, Sadjadi, S., Ed. Academic Press: Boston, 2016; pp 341-371.
- [94] Lomora, M.; Garni, M.; Itel, F.; Tanner, P.; Spulber, M.; Palivan, C. G., Polymersomes with engineered ion selective permeability as stimuli-responsive nanocompartments with preserved architecture. *Biomaterials* **2015**, *53*, 406-414.
- [95] Kumar, M.; Grzelakowski, M.; Zilles, J.; Clark, M.; Meier, W., Highly permeable polymeric membranes based on the incorporation of the functional water channel protein Aquaporin Z. *P Natl Acad Sci USA* **2007**, *104* (52), 20719-20724.
- [96] Nardin, C.; Widmer, J.; Winterhalter, M.; Meier, W., Amphiphilic block copolymer nanocontainers as bioreactors. *Eur Phys J E* **2001**, *4* (4), 403-410.
- [97] Huang, L. L.; Chen, X. Z.; Muhlenbernd, H.; Zhang, H.; Chen, S. M.; Bai, B. F.; Tan, Q. F.; Jin, G. F.; Cheah, K. W.; Qiu, C. W.; Li, J. S.; Zentgraf, T.; Zhang, S., Three-dimensional optical holography using a plasmonic metasurface. *Nat Commun* **2013**, *4*.
- [98] Garni, M.; Einfalt, T.; Goers, R.; Palivan, C. G.; Meier, W., Live Follow-Up of Enzymatic Reactions Inside the Cavities of Synthetic Giant Unilamellar Vesicles Equipped with Membrane Proteins Mimicking Cell Architecture. *Acs Synth Biol*

- 2018, 7(9), 2116-2125.
- [99] Jang, W. S.; Park, S. C.; Reed, E. H.; Dooley, K. P.; Wheeler, S. F.; Lee, D.; Hammer, D. A., Enzymatically triggered rupture of polymersomes. *Soft Matter* **2016**, 12 (4), 1014-20.
- [100] Armada-Moreira, A.; Thingholm, B.; Andreassen, K.; Sebastiao, A. M.; Vaz, S. H.; Stadler, B., On the Assembly of Microreactors with Parallel Enzymatic Pathways. *Adv Biosyst* **2018**, 2 (5).
- [101] Liu, X. L.; Formanek, P.; Voit, B.; Appelhans, D., Functional Cellular Mimics for the Spatiotemporal Control of Multiple Enzymatic Cascade Reactions. *Angew Chem Int Edit* **2017**, 56 (51), 16233-16238.
- [102] Godoy-Gallardo, M.; Labay, C.; Trikalitis, V. D.; Kempen, P. J.; Larsen, J. B.; Andresen, T. L.; Hosta-Rigau, L., Multicompartment Artificial Organelles Conducting Enzymatic Cascade Reactions inside Cells. *Acs Appl Mater Inter* **2017**, 9 (19), 15907-15921.
- [103] Zhang, Y.; Baekgaard-Laursen, M.; Stadler, B., Small Subcompartmentalized Microreactors as Support for Hepatocytes. *Adv Healthc Mater* **2017**, 6 (15).
- [104] Hammer, D. A.; Robbins, G. P.; Haun, J. B.; Lin, J. J.; Qi, W.; Smith, L. A.; Ghoroghchian, P. P.; Therien, M. J.; Bates, F. S., Leuko-polymersomes. *Faraday Discuss* **2008**, 139, 129-141.
- [105] Kubilis, A.; Abdulkarim, A.; Eissa, A. M.; Cameron, N. R., Giant Polymersome Protocells Dock with Virus Particle Mimics via Multivalent Glycan-Lectin Interactions. *Sci Rep-Uk* **2016**, 6.
- [106] Najer, A.; Thamboo, S.; Palivan, C. G.; Beck, H. P.; Meier, W., Giant Host Red Blood Cell Membrane Mimicking Polymersomes Bind Parasite Proteins and Malaria Parasites. *Chimia* **2016**, 70 (4), 288-291.
- [107] Martino, C.; Kim, S. H.; Horsfall, L.; Abbaspourrad, A.; Rosser, S. J.; Cooper, J.; Weitz, D. A., Protein Expression, Aggregation, and Triggered Release from Polymersomes as Artificial Cell-like Structures. *Angew Chem Int Edit* **2012**, 51 (26), 6416-6420.
- [108] Otrin, L.; Marusic, N.; Bednarz, C.; Vidakovic-Koch, T.; Lieberwirt, I.; Landfester, K.; Sundmacher, K., Toward Artificial Mitochondrion: Mimicking Oxidative Phosphorylation in Polymer and Hybrid Membranes. *Nano Lett* **2017**, 17 (11), 6816-6821.
- [109] Bastakoti, B. P.; Perez-Mercader, J., Autonomous Ex Novo Chemical Assembly with Blebbing and Division of Functional Polymer Vesicles from a "Homogeneous Mixture". *Adv Mater* **2017**, 29 (43).
- [110] Tamate, R.; Hashimoto, K.; Horii, T.; Hirasawa, M.; Li, X.; Shibayama, M.;

- Watanabe, M., Self-Healing Micellar Ion Gels Based on Multiple Hydrogen Bonding. *Adv Mater* **2018**, *30* (36).
- [111] Lu, A. X.; Oh, H.; Terrell, J. L.; Bentley, W. E.; Raghavan, S. R., A new design for an artificial cell: polymer microcapsules with addressable inner compartments that can harbor biomolecules, colloids or microbial species. *Chem Sci* **2017**, *8* (10), 6893-6903.
- [112] Peyret, A.; Ibarboure, E.; Pippa, N.; Lecommandoux, S., Liposomes in Polymersomes: Multicompartment System with Temperature-Triggered Release. *Langmuir* **2017**, *33* (28), 7079-7085.
- [113] Marguet, M.; Bonduelle, C.; Lecommandoux, S., Multicompartmentalized polymeric systems: towards biomimetic cellular structure and function. *Chem Soc Rev* **2013**, *42* (2), 512-29.
- [114] Chandrawati, R.; Hosta-Rigau, L.; Vanderstraaten, D.; Lokuliyana, S. A.; Stadler, B.; Albericio, F.; Caruso, F., Engineering Advanced Capsosomes: Maximizing the Number of Subcompartments, Cargo Retention, and Temperature-Triggered Reaction. *Acs Nano* **2010**, *4* (3), 1351-1361.
- [115] Lomas, H.; Johnston, A. P. R.; Such, G. K.; Zhu, Z. Y.; Liang, K.; van Koeveden, M. P.; Alongkornchotikul, S.; Caruso, F., Polymersome-Loaded Capsules for Controlled Release of DNA. *Small* **2011**, *7* (14), 2109-2119.
- [116] Costa, R. R.; Castro, E.; Arias, F. J.; Rodriguez-Cabello, J. C.; Mano, J. F., Multifunctional Compartmentalized Capsules with a Hierarchical Organization from the Nano to the Macro Scales. *Biomacromolecules* **2013**, *14* (7), 2403-2410.
- [117] Driever, C. D.; Mulet, X.; Waddington, L. J.; Postma, A.; Thissen, H.; Caruso, F.; Drummond, C. J., Layer-by-layer polymer coating on discrete particles of cubic lyotropic liquid crystalline dispersions (cubosomes). *Langmuir* **2013**, *29* (42), 12891-900.
- [118] York-Duran, M. J.; Godoy-Gallardo, M.; Labay, C.; Urquhart, A. J.; Andresen, T. L.; Hosta-Rigau, L., Recent advances in compartmentalized synthetic architectures as drug carriers, cell mimics and artificial organelles. *Colloids Surf B Biointerfaces* **2017**, *152*, 199-213.
- [119] Utech, S.; Scherer, C.; Maskos, M., Multifunctional, multicompartment polyorganosiloxane magnetic nanoparticles for biomedical applications. *J Magn Magn Mater* **2009**, *321* (10), 1386-1388.
- [120] Wei, L. J.; Yan, S.; Wang, H. H.; Yang, H. Q., Fabrication of multi-compartmentalized mesoporous silica microspheres through a Pickering droplet strategy for enhanced CO₂ capture and catalysis. *Npg Asia Mater* **2018**, *10*, 899-911.
- [121] McPhail, D.; Tetley, L.; Dufes, C.; Uchegbu, I. F., Liposomes encapsulating

- polymeric chitosan based vesicles - a vesicle in vesicle system for drug delivery. *Int J Pharmaceut* **2000**, *200* (1), 73-86.
- [122] Walker, S. A.; Kennedy, M. T.; Zasadzinski, J. A., Encapsulation of bilayer vesicles by self-assembly. *Nature* **1997**, *387* (6628), 61-4.
- [123] Evans, C. C.; Zasadzinski, J., Encapsulating vesicles and colloids from cochleate cylinders. *Langmuir* **2003**, *19* (8), 3109-3113.
- [124] Ogue, S.; Takahashi, Y.; Onishi, H.; Machida, Y., Preparation of double liposomes and their efficiency as an oral vaccine carrier. *Biol Pharm Bull* **2006**, *29* (6), 1223-1228.
- [125] Yamabe, K.; Kato, Y.; Onishi, H.; Machida, Y., In vitro characteristics of liposomes and double liposomes prepared using a novel glass beads method. *J Control Release* **2003**, *90* (1), 71-79.
- [126] Bolinger, P. Y.; Stamou, D.; Vogel, H., Integrated nanoreactor systems: Triggering the release and mixing of compounds inside single vesicles. *J Am Chem Soc* **2004**, *126* (28), 8594-8595.
- [127] Elani, Y.; Gee, A.; Law, R. V.; Ces, O., Engineering multi-compartment vesicle networks. *Chem Sci* **2013**, *4* (8), 3332-3338.
- [128] Petrov, P. D.; Drechsler, M.; Muller, A. H. E., Self-Assembly of Asymmetric Poly(ethylene oxide)-block-Poly (n-butyl acrylate) Diblock Copolymers in Aqueous Media to Unexpected Morphologies. *J Phys Chem B* **2009**, *113* (13), 4218-4225.
- [129] Fu, Z. K.; Ochsner, M. A.; de Hoog, H. P. M.; Tomczak, N.; Nallani, M., Multicompartmentalized polymersomes for selective encapsulation of biomacromolecules. *Chem Commun* **2011**, *47* (10), 2862-2864.
- [130] Chiu, H. C.; Lin, Y. W.; Huang, Y. F.; Chuang, C. K.; Chern, C. S., Polymer vesicles containing small vesicles within interior aqueous compartments and pH-Responsive transmembrane channels. *Angew Chem Int Edit* **2008**, *47* (10), 1875-1878.
- [131] Shum, H. C.; Zhao, Y. J.; Kim, S. H.; Weitz, D. A., Multicompartment Polymersomes from Double Emulsions. *Angew Chem Int Edit* **2011**, *50* (7), 1648-1651.
- [132] Kim, S. H.; Shum, H. C.; Kim, J. W.; Cho, J. C.; Weitz, D. A., Multiple Polymersomes for Programmed Release of Multiple Components. *J Am Chem Soc* **2011**, *133* (38), 15165-15171.
- [133] Marguet, M.; Sandre, O.; Lecommandoux, S., Polymersomes in "gelly" polymersomes: toward structural cell mimicry. *Langmuir* **2012**, *28* (4), 2035-43.
- [134] Brea, R. J.; Hardy, M. D.; Devaraj, N. K., Towards Self-Assembled Hybrid Artificial Cells: Novel Bottom-Up Approaches to Functional Synthetic Membranes.

- Chem-Eur J* **2015**, *21* (36), 12564-12570.
- [135] Hosta-Rigau, L.; Chung, S. F.; Postma, A.; Chandrawati, R.; Stadler, B.; Caruso, F., Capsosomes with "Free-Floating" Liposomal Subcompartments. *Adv Mater* **2011**, *23* (35), 4082-+.
- [136] Hindley, J. W.; Elani, Y.; McGilvery, C. M.; Ali, S.; Bevan, C. L.; Law, R. V.; Ces, O., Light-triggered enzymatic reactions in nested vesicle reactors. *Nat Commun* **2018**, *9*.
- [137] Cortese, J. D.; Schwab, B.; Frieden, C.; Elson, E. L., Actin Polymerization Induces a Shape Change in Actin-Containing Vesicles. *P Natl Acad Sci USA* **1989**, *86* (15), 5773-5777.
- [138] Abkarian, M.; Loiseau, E.; Massiera, G., Continuous droplet interface crossing encapsulation (cDICE) for high throughput monodisperse vesicle design. *Soft Matter* **2011**, *7* (10), 4610-4614.
- [139] Hayashi, M.; Nishiyama, M.; Kazayama, Y.; Toyota, T.; Harada, Y.; Takiguchi, K., Reversible Morphological Control of Tubulin-Encapsulating Giant Liposomes by Hydrostatic Pressure. *Langmuir* **2016**, *32* (15), 3794-3802.
- [140] Schafer, E.; Vache, M.; Kliesch, T. T.; Janshoff, A., Mechanical response of adherent giant liposomes to indentation with a conical AFM-tip. *Soft Matter* **2015**, *11* (22), 4487-4495.
- [141] Tsai, F. C.; Koenderink, G. H., Shape control of lipid bilayer membranes by confined actin bundles. *Soft Matter* **2015**, *11* (45), 8834-8847.
- [142] Carvalho, K.; Tsai, F. C.; Lees, E.; Voituriez, R.; Koenderink, G. H.; Sykes, C., Cell-sized liposomes reveal how actomyosin cortical tension drives shape change (vol 110, pg 16456, 2013). *P Natl Acad Sci USA* **2013**, *110* (49), 19969-19969.
- [143] Keber, F. C.; Loiseau, E.; Sanchez, T.; DeCamp, S. J.; Giomi, L.; Bowick, M. J.; Marchetti, M. C.; Dogic, Z.; Bausch, A. R., Topology and dynamics of active nematic vesicles. *Science* **2014**, *345* (6201), 1135-1139.
- [144] Loiseau, E.; Schneider, J. A. M.; Keber, F. C.; Pelzl, C.; Massiera, G.; Salbreux, G.; Bausch, A. R., Shape remodeling and blebbing of active cytoskeletal vesicles. *Sci Adv* **2016**, *2* (4).
- [145] van Swaay, D.; deMello, A., Microfluidic methods for forming liposomes (vol 13, pg 752, 2013). *Lab Chip* **2013**, *13* (24), 4890-4890.
- [146] Guevorkian, K.; Manzi, J.; Pontani, L. L.; Brochard-Wyart, F.; Sykes, C., Mechanics of Biomimetic Liposomes Encapsulating an Actin Shell. *Biophys J* **2015**, *109* (12), 2471-2479.
- [147] Luo, T. Z.; Mohan, K.; Iglesias, P. A.; Robinson, D. N., Molecular mechanisms of cellular mechanosensing. *Nat Mater* **2013**, *12* (11), 1063-1070.

- [148] Sato, Y.; Hiratsuka, Y.; Kawamata, I.; Murata, S.; Nomura, S. M., Micrometer-sized molecular robot changes its shape in response to signal molecules. *Sci Robot* **2017**, *2* (4).
- [149] Luo, T. Z.; Srivastava, V.; Ren, Y. X.; Robinson, D. N., Mimicking the mechanical properties of the cell cortex by the self-assembly of an actin cortex in vesicles. *Appl Phys Lett* **2014**, *104* (15).
- [150] Koenderink, G. H.; Dogic, Z.; Nakamura, F.; Bendix, P. M.; MacKintosh, F. C.; Hartwig, J. H.; Stossel, T. P.; Weitz, D. A., An active biopolymer network controlled by molecular motors. *P Natl Acad Sci USA* **2009**, *106* (36), 15192-15197.
- [151] Lieleg, O.; Claessens, M. M. A. E.; Luan, Y.; Bausch, A. R., Transient binding and dissipation in cross-linked actin networks. *Phys Rev Lett* **2008**, *101* (10).
- [152] Yao, N. Y.; Broedersz, C. P.; Depken, M.; Becker, D. J.; Pollak, M. R.; MacKintosh, F. C.; Weitz, D. A., Stress-Enhanced Gelation: A Dynamic Nonlinearity of Elasticity. *Phys Rev Lett* **2013**, *110* (1).
- [153] Weiss, M.; Frohnmayer, J. P.; Benk, L. T.; Haller, B.; Janiesch, J. W.; Heitkamp, T.; Borsch, M.; Lira, R. B.; Dimova, R.; Lipowsky, R.; Bodenschatz, E.; Baret, J. C.; Vidakovic-Koch, T.; Sundmacher, K.; Platzman, I.; Spatz, J. P., Sequential bottom-up assembly of mechanically stabilized synthetic cells by microfluidics. *Nat Mater* **2018**, *17* (1), 89-+.
- [154] Tsai, F. C.; Stuhrmann, B.; Koenderink, G. H., Encapsulation of Active Cytoskeletal Protein Networks in Cell-Sized Liposomes. *Langmuir* **2011**, *27* (16), 10061-10071.
- [155] Pontani, L. L.; van der Gucht, J.; Salbreux, G.; Heuvingh, J.; Joanny, J. F.; Sykes, C., Reconstitution of an Actin Cortex Inside a Liposome. *Biophys J* **2009**, *96* (1), 192-198.
- [156] Limozin, L.; Roth, A.; Sackmann, E., Microviscoelastic moduli of biomimetic cell envelopes. *Phys Rev Lett* **2005**, *95* (17).
- [157] van Oudenaarden, A.; Theriot, J. A., Cooperative symmetry-breaking by actin polymerization in a model for cell motility. *Nat Cell Biol* **1999**, *1* (8), 493-9.
- [158] Stachowiak, J. C.; Richmond, D. L.; Li, T. H.; Brochard-Wyart, F.; Fletcher, D. A., Inkjet formation of unilamellar lipid vesicles for cell-like encapsulation. *Lab Chip* **2009**, *9* (14), 2003-9.
- [159] Limozin, L.; Barmann, M.; Sackmann, E., On the organization of self-assembled actin networks in giant vesicles. *Eur Phys J E Soft Matter* **2003**, *10* (4), 319-30.
- [160] Limozin, L.; Sackmann, E., Polymorphism of cross-linked actin networks in giant vesicles. *Phys Rev Lett* **2002**, *89* (16), 168103.
- [161] Honda, M.; Takiguchi, K.; Ishikawa, S.; Hotani, H., Morphogenesis of liposomes

- encapsulating actin depends on the type of actin-crosslinking. *J Mol Biol* **1999**, *287* (2), 293-300.
- [162] Lee, K. Y.; Park, S. J.; Lee, K. A.; Kim, S. H.; Kim, H.; Meroz, Y.; Mahadevan, L.; Jung, K. H.; Ahn, T. K.; Parker, K. K.; Shin, K., Photosynthetic artificial organelles sustain and control ATP-dependent reactions in a protocellular system. *Nat Biotechnol* **2018**, *36* (6), 530-535.
- [163] Dhir, S.; Salahub, S.; Mathews, A. S.; Kumaran, S. K.; Montemagno, C. D.; Abraham, S., Light-induced ATP driven self-assembly of actin and heavy-meromyosin in proteo-tubularsomes as a step toward artificial cells. *Chem Commun* **2018**, *54* (42), 5346-5349.
- [164] Najer, A.; Wu, D. L.; Vasquez, D.; Palivan, C. G.; Meier, W., Polymer nanocompartments in broad-spectrum medical applications. *Nanomedicine-Uk* **2013**, *8* (3), 425-447.
- [165] Einfalt, T.; Witzigmann, D.; Edlinger, C.; Sieber, S.; Goers, R.; Najer, A.; Spulber, M.; Onaca-Fischer, O.; Huwyler, J.; Palivan, C. G., Biomimetic artificial organelles with in vitro and in vivo activity triggered by reduction in microenvironment. *Nat Commun* **2018**, *9*.
- [166] Gumz, H.; Boye, S.; Iyisan, B.; Kronert, V.; Formanek, P.; Voit, B.; Lederer, A.; Appelhans, D., Toward Functional Synthetic Cells: In-Depth Study of Nanoparticle and Enzyme Diffusion through a Cross-Linked Polymersome Membrane. *Adv Sci* **2019**, *6* (7).
- [167] Najer, A.; Wu, D. L.; Bieri, A.; Brand, F.; Palivan, C. G.; Beck, H. P.; Meier, W., Nanomimics of Host Cell Membranes Block Invasion and Expose Invasive Malaria Parasites. *Acs Nano* **2014**, *8* (12), 12560-12571.
- [168] Farrugia, B. L.; Mi, Y. L.; Kim, H. N.; Whitelock, J. M.; Baker, S. M.; Wiesmann, W. P.; Li, Z.; Maitz, P.; Lord, M. S., Chitosan-Based Heparan Sulfate Mimetics Promote Epidermal Formation in a Human Organotypic Skin Model. *Adv Funct Mater* **2018**, *28* (36).
- [169] Vankerkhof, J. C.; Bergveld, P.; Schasfoort, R. B. M., Development of an Isfet Based Heparin Sensor Using the Ion-Step Measuring Method. *Biosens Bioelectron* **1993**, *8* (9-10), 463-472.
- [170] Najer, A.; Wu, D. L.; Nussbaumer, M. G.; Schwertz, G.; Schwab, A.; Witschel, M. C.; Schafer, A.; Diederich, F.; Rottmann, M.; Palivan, C. G.; Beck, H. P.; Meier, W., An amphiphilic graft copolymer-based nanoparticle platform for reduction-responsive anticancer and antimalarial drug delivery. *Nanoscale* **2016**, *8* (31), 14858-14869.
- [171] Altan-Bonnet, N.; Altan-Bonnet, G., Fluorescence correlation spectroscopy in living cells: a practical approach. *Curr Protoc Cell Biol* **2009**, *Chapter 4*, Unit 4 24.

- [172] Itel, F.; Najer, A.; Palivan, C. G.; Meier, W., Dynamics of Membrane Proteins within Synthetic Polymer Membranes with Large Hydrophobic Mismatch. *Nano Lett* **2015**, *15* (6), 3871-3878.
- [173] Itel, F.; Chami, M.; Najer, A.; Lorcher, S.; Wu, D. L.; Dinu, I. A.; Meier, W., Molecular Organization and Dynamics in Polymersome Membranes: A Lateral Diffusion Study. *Macromolecules* **2014**, *47* (21), 7588-7596.
- [174] Meister, A., Glutathione Metabolism and Its Selective Modification. *J Biol Chem* **1988**, *263* (33), 17205-17208.
- [175] Ates, B.; Ercal, B. C.; Manda, K.; Abraham, L.; Ercal, N., Determination of glutathione disulfide levels in biological samples using thiol-disulfide exchanging agent, dithiothreitol. *Biomed Chromatogr* **2009**, *23* (2), 119-123.
- [176] Chung, W. S.; Farley, J. M.; Drummond, H. A., ASIC-like Currents in Freshly Isolated Cerebral Artery Smooth Muscle Cells are Inhibited by Endogenous Oxidase Activity. *Cell Physiol Biochem* **2011**, *27* (2), 129-138.
- [177] Graf, P.; Sies, H., Hepatic-Uptake of Cadmium and Its Biliary Release as Affected by Dithioerythritol and Glutathione. *Biochem Pharmacol* **1984**, *33* (4), 639-643.
- [178] Holme, J. A.; Dahlin, D. C.; Nelson, S. D.; Dybing, E., Cyto-Toxic Effects of N-Acetyl-Para-Benzoquinone Imine, a Common Arylating Intermediate of Paracetamol and N-Hydroxyparacetamol. *Biochem Pharmacol* **1984**, *33* (3), 401-406.
- [179] Ziegler, D. M., Role of Reversible Oxidation-Reduction of Enzyme Thiols-Disulfides in Metabolic-Regulation. *Annu Rev Biochem* **1985**, *54*, 305-329.
- [180] Howse, J. R.; Jones, R. A. L.; Battaglia, G.; Ducker, R. E.; Leggett, G. J.; Ryan, A. J., Templated formation of giant polymer vesicles with controlled size distributions. *Nat Mater* **2009**, *8* (6), 507-511.
- [181] Wang, H.; Zhao, Z.; Liu, Y. X.; Shao, C. M.; Bian, F. K.; Zhao, Y. J., Biomimetic enzyme cascade reaction system in microfluidic electrospray microcapsules. *Sci Adv* **2018**, *4* (6).
- [182] Shang, L. R.; Cheng, Y.; Zhao, Y. J., Emerging Droplet Microfluidics. *Chemical Reviews* **2017**, *117* (12), 7964-8040.
- [183] Paleos, C. M.; Pantos, A., Molecular Recognition and Organizational and Polyvalent Effects in Vesicles Induce the Formation of Artificial Multicompartment Cells as Model Systems of Eukaryotes. *Accounts Chem Res* **2014**, *47* (5), 1475-1482.
- [184] Panteghini, M.; Bonora, R.; Pagani, F., Measurement of pancreatic lipase activity in serum by a kinetic colorimetric assay using a new chromogenic substrate. *Ann Clin Biochem* **2001**, *38*, 365-370.
- [185] Groten, C. J.; Magoski, N. S., PKC Enhances the Capacity for Secretion by Rapidly Recruiting Covert Voltage-Gated Ca²⁺ Channels to the Membrane. *J*

- Neurosci* **2015**, *35* (6), 2747-2765.
- [186] Capera, J.; Serrano-Novillo, C.; Navarro-Perez, M.; Cassinelli, S.; Felipe, A., The Potassium Channel Odyssey: Mechanisms of Traffic and Membrane Arrangement. *Int J Mol Sci* **2019**, *20* (3).
- [187] Balse, E.; El-Haou, S.; Dillanian, G.; Dauphin, A.; Eldstrom, J.; Fedida, D.; Coulombe, A.; Hatem, S. N., Cholesterol modulates the recruitment of Kv1.5 channels from Rab11-associated recycling endosome in native atrial myocytes. *P Natl Acad Sci USA* **2009**, *106* (34), 14681-14686.
- [188] Balse, E.; Boycott, H. E., Ion Channel Trafficking: Control of Ion Channel Density as a Target for Arrhythmias? *Front Physiol* **2017**, *8*.
- [189] Einfalt, T.; Goers, R.; Dinu, I. A.; Najer, A.; Spulber, M.; Onaca-Fischer, O.; Palivan, C. G., Stimuli-Triggered Activity of Nanoreactors by Biomimetic Engineering Polymer Membranes. *Nano Lett* **2015**, *15* (11), 7596-7603.
- [190] Xu, H.; Martinoia, E.; Szabo, I., Organellar channels and transporters. *Cell calcium* **2015**, *58* (1), 1-10.
- [191] Blanchoin, L.; Boujemaa-Paterski, R.; Sykes, C.; Plastino, J., Actin Dynamics, Architecture, and Mechanics in Cell Motility. *Physiol Rev* **2014**, *94* (1), 235-263.
- [192] Walde, P.; Cosentino, K.; Engel, H.; Stano, P., Giant vesicles: preparations and applications. *Chembiochem* **2010**, *11* (7), 848-65.
- [193] Kim, K. T.; Zhu, J.; Meeuwissen, S. A.; Cornelissen, J. J.; Pochan, D. J.; Nolte, R. J.; van Hest, J. C., Polymersome stomatocytes: controlled shape transformation in polymer vesicles. *J Am Chem Soc* **2010**, *132* (36), 12522-4.
- [194] Tanaka, S.; Takiguchi, K.; Hayashi, M., Repetitive stretching of giant liposomes utilizing the nematic alignment of confined actin. *Commun Phys* **2018**, *1*.
- [195] Ardawi, M. S. M.; Rouzi, A. A.; Qari, M. H.; Ali, A. Y.; Refai, G. Y.; Mousa, S. A., Total Serum 25(OH)D Levels Misclassify Vitamin D Status in Saudi Men and Women: The Role of Vitamin D-Binding Protein. *Osteoporosis Int* **2014**, *25*, S356-S357.
- [196] Sens, P.; Plastino, J., Membrane tension and cytoskeleton organization in cell motility. *J Phys-Condens Mat* **2015**, *27* (27).
- [197] Canning, S. L.; Smith, G. N.; Armes, S. P., A Critical Appraisal of RAFT-Mediated Polymerization-Induced Self-Assembly. *Macromolecules* **2016**, *49* (6), 1985-2001.
- [198] Nardin, C.; Hirt, T.; Leukel, J.; Meier, W., Polymerized ABA triblock copolymer vesicles. *Langmuir* **2000**, *16* (3), 1035-1041.
- [199] Shokeen, N.; Issa, C.; Mukhopadhyay, A., Comparison of nanoparticle diffusion using fluorescence correlation spectroscopy and differential dynamic microscopy

- within concentrated polymer solutions. *Appl Phys Lett* **2017**, *111* (26).
- [200] Liu, J.; Postupalenko, V.; Lörcher, S.; Wu, D.; Chami, M.; Meier, W.; Palivan, C. G., DNA-Mediated Self-Organization of Polymeric Nanocompartments Leads to Interconnected Artificial Organelles. *Nano Lett* **2016**, *16* (11), 7128-7136.
- [201] Najer, A.; Thamboo, S.; Duskey, J. T.; Palivan, C. G.; Beck, H. P.; Meier, W., Analysis of Molecular Parameters Determining the Antimalarial Activity of Polymer-Based Nanomimics. *Macromol Rapid Comm* **2015**, *36* (21), 1923-1928.
- [202] Eigen, M.; Rigler, R., Sorting Single Molecules - Application to Diagnostics and Evolutionary Biotechnology. *P Natl Acad Sci USA* **1994**, *91* (13), 5740-5747.

10. Acknowledgements

I would like to take this opportunity to express my sincere thanks to all the people who directly or indirectly have been absolutely instrumental to my success throughout my PhD here at University of Basel.

First and foremost I would like to thank *Prof. Dr. Wolfgang Meier* and *Prof. Dr. Cornelia Palivan* for giving me the opportunity to fulfil my PhD research in this interesting field. Additionally, I thank gratefully *Prof. Dr. Nico Bruns* for being my co-examiner. *Prof. Dr. Catherine Housecroft* is kindly acknowledged for being the chair.

My next acknowledgements are due to my outstanding supervisor *Dr. Adrian Najer* for his generous support, his guidance and sharing a broad experience and knowledge. I enjoyed the scientific discussions and all your input for our manuscripts. I am indebted and grateful to *Andrea Belluati* for introducing me to enzymatic cascade reactions and working together on several projects. I would like to thank *Dr. Ioana Craciun* for scientific discussions and proofreading our manuscripts.

I also thank sincerely *Dr. Dalin Wu*, *Dr. Viviana Maffeis* and *Sven Kasper* for providing me access with certain polymers. I thank *Gabriele Percy* for TEM imaging, *Carola Alampi* from the C-CINA for cryo-TEM imaging, and *Dr. Alexia Loynton-Ferrand* (IMCF, University of Basel) for 3D-SIM imaging. I am grateful to *Prof. Dr. Abhai Pandit* for all the guidance and organization during my scientific exchange in Galway, Ireland. Furthermore I would like to thank the research technical officer *Dr. Oliver Carroll* and *Dr. Renza Spelat* for their generous support during the cell experiments. I also thank sincerely *Dilip Thomas* for helping with the flow cytometry. For a lovely working atmosphere, I would like to thank my former and current colleagues from the *Meier/Palivan group*. *Serena Rigo*, I enjoyed studying with you and complete our

doctorate studies together. I would like to thank *Myrto Kyropoulou, Claire Elsa Meyer, Dr. Evgeniia Konishcheva, Dr. Pascal Richard, Dr. Samuel Lörcher, Riccardo Wehr, Dimitri Hürlimann, Davy Daubian, Dr. Jens Gaitzsch, Dr. Martina Garni,* and *Dr. Cora-Ann Schönenberger* for their support. I thank my students *Patrick Weber, Florian Wenger* and *Benjamin Manser*. For administrative support, I thank *Maya Greuter, Daniela Tischhauser, Beatrice Erismann, Olaf Lips, Philipp Knöpfel, Grischa Martin, Dr. Michael Devereux, Mariella Schneiter* and *Markus Hauri*.

I am grateful for all my *family and friends* whose support was very valuable.

Claudio, I thank you for all the love and tremendous support during the last eight years. Thanks for establishing the customized python scripts for my data analysis.

Finally, I am deeply grateful to my beloved parents (*Amma* and *Appa*) and my sisters (*Keerthana* and *Santhana*) for their love and continuous support. Without their help, I wouldn't have been here.